

**TUNING OF THE MULTIFERROIC PROPERTIES OF  
SELECTED MATERIALS BY MAGNETIC FIELD,  
CHEMICAL DOPING, AND PRESSURE**

---

A Dissertation Presented to  
the Faculty of the Department of Physics  
University of Houston

---

In Partial Fulfillment  
of the Requirements for the Degree  
Doctor of Philosophy

---

By  
Narayan Poudel  
May 2017

**TUNING OF THE MULTIFERROIC PROPERTIES OF  
SELECTED MATERIALS BY MAGNETIC FIELD,  
CHEMICAL DOPING, AND PRESSURE**

---

Narayan Poudel

APPROVED:

---

Dr. Ching-Wu Chu, Chairman  
Department of Physics, University of Houston

---

Dr. Zhifeng Ren  
Department of Physics, University of Houston

---

Dr. Allan J. Jacobson  
Department of Chemistry, University of Houston

---

Dr. Wei-Kan Chu  
Department of Physics, University of Houston

---

Dr. Chin-Sen Ting  
Department of Physics, University of Houston

---

Dean, College of Natural Sciences and Mathematics

# Acknowledgements

Four years ago, Dr. Chu accepted me to work in the HPLT group and I was quite excited, which still holds true today. I would like to thank my academic advisor Prof. Paul Chu wholeheartedly for giving me the opportunity to work in his prestigious group and for his active guidance throughout my graduate studies. I feel grateful for my advisor's support which allowed for me to attend numerous conferences, symposiums, summer schools and also in participating in research experiments at national laboratories. This also allowed numerous opportunities for me to connect with research scholars in my research field. I am indebted to my research supervisor Prof. Bernd Lorenz for his continuous support in my research work and his inspirational advice for my future career. I am grateful for his encouragement in every aspect of my research work for helping me connect with collaborators.

This work wouldn't be complete without my dissertation committee members: Prof. Zhifeng Ren, Prof. Allan Jacobson, Prof. Wei-Kan Chu and Prof. Chin-Sen whose constructive suggestions to elaborate the research work during annual progress evaluation is highly commendable. I highly appreciate the feedback and guidance of our group members Melissa Gooch, Zheng Wu, Bing Lv, Quantum Deng, Keshav, Kui, Ben, Hanming and Shuyuan for their help throughout my research work. Melissa made me familiar with various Lab instrumentation, especially the high-pressure techniques and modestly helped me edit my writing stuff. Zheng and Quantum helped me with technical issues and measurements. I also want to acknowledge the help of our previous group members Y. Q. Wang, Y. Y. Sun in sample-growth and X-ray measurements. I express my gratitude to our collaborators Prof. S. W.

Cheong and Prof. M. Jain who procured us high-quality samples, and to Dr. Feng Ye who guided us in neutron diffraction experiments and gave valuable lessons in data analysis. Finally, I would like to thank Troy, Helen, Ileana and Naomi for their help in administrative affairs.

Last but not the least, I want to thank my parents for their incessant support and noble inspiration throughout my research and academic endeavors that have extended throughout my life. I can hardly describe with good enough pedigree the uncompromised and relentless efforts of my wife to keep my motivation high through the times of perseverance and hardships.

**TUNING OF THE MULTIFERROIC PROPERTIES OF  
SELECTED MATERIALS BY MAGNETIC FIELD,  
CHEMICAL DOPING, AND PRESSURE**

---

An Abstract of a Dissertation  
Presented to  
the Faculty of the Department of Physics  
University of Houston

---

In Partial Fulfillment  
of the Requirements for the Degree  
Doctor of Philosophy

---

By  
Narayan Poudel  
May 2017

# Abstract

This work will explore how magnetic field, chemical doping, and hydrostatic pressure affect type-II multiferroic materials. Above a critical field, a ferroelectric polarization is induced by an externally applied magnetic field and its reversal is observed in coexisting multiferroic phases of  $\text{Mn}_{1-x}\text{Co}_x\text{WO}_4$ . The sign reversal of the polarization is explained on the basis of strong inter-domain coupling between the two coexisting multiferroic phases and the preserved chirality of the spin helix across their domain boundary. Also observed at low cobalt doping, was the continuous rotation of the polarization in the magnetic field, thereby charging the ferroelectric domain walls.

Next, the evolution of different magnetic and multiferroic phases was explored up to 30% nickel doping in  $\text{MnWO}_4$  via magnetic, ferroelectric, heat capacity and neutron diffraction measurements. Nickel doping quickly suppressed the paraelectric phase observed at lower nickel dopings and suppressed the multiferroicity at higher doping in  $\text{MnWO}_4$ . The anisotropy and anti-correlation effect between Mn and Ni spins forced the suppression of polarization which was observed for higher nickel concentration.

Lastly the effect of pressure up to 18 kbars was explored for  $\text{GdMn}_2\text{O}_5$  and  $\text{RCrO}_3$  ( $\text{R} = \text{Ho}, \text{Dy}, \text{Gd}$ ). A new ferroelectric phase was induced above a critical pressure and also at a higher temperature, than the already reported multiferroic phase for  $\text{GdMn}_2\text{O}_5$ . The new ferroelectric phase is explained on the basis of pressure induced decoupling of Gd-moments and Mn-spins in the commensurate phase. The decoupled Mn spins order at higher temperature which gives rise to the new ferroelectric phase. On the other hand, the pressure effect on Néel temperature of the multiferroic  $\text{RCrO}_3$

(R = Ho, Dy, Gd) shows that Néel temperature of  $\text{RCrO}_3$  increases with pressure.

# Contents

<b>1</b>	<b>Introduction</b>	<b>1</b>
<b>2</b>	<b>Background</b>	<b>5</b>
2.1	Dielectric constant . . . . .	5
2.2	Ferroic order . . . . .	6
2.3	Ferroelectricity . . . . .	7
2.4	Proper and improper ferroelectrics . . . . .	9
2.5	Polarization and surface charge density . . . . .	9
2.6	Landau theory of ferroelectric phase transition . . . . .	10
2.7	Magnetic properties of solids . . . . .	13
2.8	Magnetic frustration . . . . .	16
2.9	Multiferroics . . . . .	17
2.10	Ferroelectricity in spiral magnets . . . . .	19
2.11	Ferroelectricity in collinear magnets . . . . .	23
2.12	Pressure effect in multiferroics . . . . .	23
<b>3</b>	<b>Methods</b>	<b>24</b>
3.1	Sample growth . . . . .	24
3.1.1	Single crystal growth of $\text{Mn}_{1-x}\text{Co}_x\text{WO}_4$ and $\text{Mn}_{1-x}\text{Ni}_x\text{WO}_4$ . . . . .	24

3.1.2	Single crystal growth of $\text{RMn}_2\text{O}_5$ ( $\text{R} = \text{Gd}, \text{Tm}$ ) . . . . .	25
3.1.3	Polycrystal growth of $\text{RCrO}_3$ ( $\text{R} = \text{Ho}, \text{Dy}, \text{Gd}$ ) . . . . .	25
3.2	Determination of single crystal orientation . . . . .	26
3.3	Physical property measurement system . . . . .	26
3.4	Magnetic property measurement system . . . . .	26
3.5	Dielectric constant measurement . . . . .	27
3.6	Pyroelectric current and polarization measurement . . . . .	28
3.7	High-pressure measurements of dielectric and pyroelectric current . . . . .	29
3.8	Mutual induction measurement under high-pressure . . . . .	33
3.9	Specific heat measurement . . . . .	34
3.10	Dilatometer and thermal expansion measurement . . . . .	36
3.11	Neutron diffraction . . . . .	40
<b>4</b>	<b>Results</b> . . . . .	<b>41</b>
4.1	Magnetic field effect in $\text{Mn}_{1-x}\text{Co}_x\text{WO}_4$ ( $x = 0.135, 0.15, 0.17$ ) . . . . .	41
4.1.1	Magnetic field induced spin-flop transition in $\text{Mn}_{0.865}\text{Co}_{0.135}\text{WO}_4$ . . . . .	48
4.1.2	Magnetic field effect in $\text{Mn}_{0.83}\text{Co}_{0.17}\text{WO}_4$ . . . . .	52
4.1.3	Polarization reversal by magnetic field in $\text{Mn}_{0.85}\text{Co}_{0.15}\text{WO}_4$ . . . . .	54
4.1.4	Origin of polarization reversal in $\text{Mn}_{0.85}\text{Co}_{0.15}\text{WO}_4$ . . . . .	60
4.1.5	Magnetic field induced polarization rotation in $\text{Mn}_{0.95}\text{Co}_{0.05}\text{WO}_4$ . . . . .	67
4.2	Effects of Ni doping on the multiferroic properties of $\text{MnWO}_4$ . . . . .	70
4.2.1	Magnetic properties of $\text{Mn}_{1-x}\text{Ni}_x\text{WO}_4$ . . . . .	72
4.2.2	Heat-capacity measurement of $\text{Mn}_{1-x}\text{Ni}_x\text{WO}_4$ . . . . .	75
4.2.3	Neutron diffraction study of $\text{Mn}_{1-x}\text{Ni}_x\text{WO}_4$ . . . . .	75
4.2.4	Ferroelectric properties of $\text{Mn}_{1-x}\text{Ni}_x\text{WO}_4$ . . . . .	80

4.3	Pressure effect on the ferroelectric properties of $\text{GdMn}_2\text{O}_5$ and $\text{TmMn}_2\text{O}_5$	85
4.3.1	Pressure effect on dielectric constant of $\text{GdMn}_2\text{O}_5$	88
4.3.2	Pressure effect on ferroelectric polarization of $\text{GdMn}_2\text{O}_5$	91
4.3.3	Thermal expansion and heat capacity measurement of $\text{GdMn}_2\text{O}_5$	94
4.3.4	Origin of pressure-induced ferroelectric phase in $\text{GdMn}_2\text{O}_5$	98
4.3.5	Pressure effect on ferroelectricity of $\text{TmMn}_2\text{O}_5$	101
4.4	Pressure effect on Néel temperature of $\text{RCrO}_3$ ( $\text{R} = \text{Ho}, \text{Dy}, \text{Gd}$ )	103
<b>5</b>	<b>Summary</b>	<b>110</b>
<b>A</b>	<b>Publications and Conference Participations</b>	<b>114</b>
A.1	Publications	114
A.2	Conference and symposium presentations	115
	<b>Bibliography</b>	<b>118</b>

# List of Figures

1.1	Number of publications per year on the topic of multiferroic or magnetoelectric materials. The data were collected from the Web of Science. . . . .	3
2.1	A typical P - E hysteresis loop in ferroelectric materials. . . . .	8
2.2	Landau free energy as a function of $P^2$ in the first-order phase transition. . . . .	12
2.3	Temperature dependence of the magnetic susceptibility and its inverse in paramagnetic, ferromagnetic and antiferromagnetic materials. . . . .	15
2.4	(a) Multiferroics combining the ferroelectric and ferromagnetic order in the same phase. (b) Inversion symmetry breaking by a spiral magnetic order under space inversion. The image (a) is taken from ref. [1] . . . . .	18
2.5	(a) Collinear E-type ( $\uparrow\uparrow\downarrow\downarrow$ ) spin structure. The collinear spin structure is formed if $J'/J > 1/2$ . The + and - sign means the neighboring ions have different valence states (different charges) and induce ferroelectricity. (b) Spiral spin structure. The spiral spin structure is formed if $J'/J > 1/4$ . (c) Polarization induced by two non-collinear spins. . . . .	20
2.6	Various types of spin orders in frustrated multiferroics. The figure is referenced from [2] with permission. . . . .	22
3.1	Second-order gradiometer superconducting detection coil in MPMS. The figure is taken from ref. [3], fundamentals of magnetism and magnetic measurement system from Quantum Design. . . . .	27
3.2	Pyroelectric current observed in $GdMn_2O_5$ during cooling cycle. The reference line drawn is used to subtract the background current. . . . .	30

3.3	The schematic diagram of the pressure cell with sample and lead manometer inside the Teflon sample holder. The Teflon sample holder is filled with the pressure medium FC-77. . . . .	32
3.4	Expanded view of Quantum Design heat capacity puck [4]. The diameter of the puck is 20 mm and the height is 15 mm. . . . .	35
3.5	The front view of different parts of the high-precision dilatometer. . .	38
4.1	Crystal structure of monoclinic $\text{MnWO}_4$ . The zigzag chains of the Mn ions are surrounded by an oxygen octahedra along the $c$ -axis and the Mn spins are frustrated along the $a$ - and $c$ -directions. . . . .	42
4.2	(a) Phase diagram of Co doped $\text{MnWO}_4$ without magnetic field [5]. (b), (c) and (d) show the spin helix in different multiferroic phases of $\text{Mn}_{1-x}\text{Co}_x\text{WO}_4$ . The large arrows indicate the direction of polarization in respective multiferroic phases. . . . .	45
4.3	The dependence of angle $\Theta$ with Co and Zn concentration in $\text{Mn}_{1-x}\text{Co}_x\text{WO}_4$ and $\text{Mn}_{1-x}\text{Zn}_x\text{WO}_4$ . The angle $\Theta$ in AF2 phase decreases with increased Co concentration. Above 7.5% Co doping, $\Theta$ vanishes and the helical plane flips into $a - c$ plane (not shown in the figure). The image is taken from [6] with permission. . . . .	46
4.4	Magnetic measurement $M(T)$ of $\text{Mn}_{0.865}\text{Co}_{0.135}\text{WO}_4$ in the magnetic field along different directions. The sharp increase of $M(T)$ in the $c$ -axis magnetic field above 25 kOe indicates the spin-flop transition in AF5 helical phase. . . . .	49
4.5	Magnetic field dependence of $P_b$ in $\text{Mn}_{1-x}\text{Co}_x\text{WO}_4$ . (a) For $x = 0.135$ , $P_b$ appears suddenly above 20 kOe in the AF5 phase and remains constant at low temperature. The $T_C$ increases with the magnetic field and reaches to 9 K at 70 kOe. (b) For $x = 0.17$ , $P_b$ is unaffected by the $c$ -axis magnetic field up to 50 kOe. A small drop in $P_b$ is observed at low temperature above 50 kOe. . . . .	51
4.6	Magnetic measurement $M(T)$ for $\text{Mn}_{0.83}\text{Co}_{0.17}\text{WO}_4$ along different directions. $M(T)$ along the $b$ -axis is different than other directions due to transverse magnetic field with spin orientation in the AF4 phase. .	53
4.7	Polarization reversal in $\text{Mn}_{0.85}\text{Co}_{0.15}\text{WO}_4$ in the $c$ -axis magnetic field. The $P_b$ becomes negative below $T_{C2}$ above 25 kOe. $T_{C2}$ increases with the magnetic field while $T_{C1}$ slightly decreases above 50 kOe. . . . .	56

4.8	Magnetic measurements $M(T)$ of $Mn_{0.85}Co_{0.15}WO_4$ in the $c$ -axis magnetic field. $M(T)$ decreases below $T_N$ and suddenly increases due to the spin-flop transition in AF5 phase at 7 K above 20 kOe. $M(T)$ remains constant at low temperature after the spin-flop transition. . .	57
4.9	Relevant exchange interaction pathways in $MnWO_4$ based on exchange energy ( $J$ ). The exchange energies of the spin pairs were obtained by fitting spin wave excitation of $MnWO_4$ with the Heisenberg model [7]. The strength of interaction between spin pairs is proportional to the polarization if allowed by symmetry. . . . .	61
4.10	The schematic diagram of normal vector $\mathbf{n}$ to the helical plane, angle $\Theta$ between the normal $\mathbf{n}$ and the $z$ -axis, angle $\varphi$ made by projection of $\mathbf{n}$ in the $x$ - $y$ plane with the $x$ -axis. The $x$ , $y$ and $z$ -axes correspond to the $a$ , $b$ and $c$ -axes of the crystal geometry. . . . .	62
4.11	The smooth transition across the domain wall of two multiferroic phases [8]. (a) Sketch of total contribution to $P_b$ by $J_1$ and $J_3$ exchange pathways in the two domains. (b) Domain structure of the AF5 phase after spin-flop transition. (c) Domain wall transition between the AF2/4 phase and AF5 phase in the $c$ -axis magnetic field. (d) Domain structure of the AF2/4 phase. . . . .	64
4.12	Ferroelectric polarization ( $P_b$ ) of $Mn_{0.85}Co_{0.15}WO_4$ in the $a$ -axis magnetic field. Unlike in the $c$ -axis magnetic field, the total $P_b$ is positive in the $a$ -axis magnetic field. . . . .	66
4.13	(a) Continuous rotation of the polarization direction in $Mn_{0.95}Co_{0.05}WO_4$ from the $b$ -axis to $a$ -axis in the $b$ -axis magnetic field at 5 K. (b) The SGH image of side-by-side domain wall at 0 T ( $P \parallel b$ ) converting to head-to-head domain wall at 6 T ( $P \parallel a$ ) at 5 K. The SHG images are taken from ref.[9]. . . . .	68
4.14	DC susceptibility ( $M/H$ ) of $Mn_{1-x}Ni_xWO_4$ along the $b$ -axis. The shifting of peaks towards low temperature indicates that the onset temperature of the AF2 phase moves to the lower value with increased Ni concentration. The vertical arrows indicate the onset of AF4 phases for different Ni concentration. The $M/H$ data are vertically offset for better visualization. . . . .	74

4.15	Heat capacity $C_P(T)$ of $Mn_{1-x}Ni_xWO_4$ . All the magnetic phase transitions are clearly reflected in the heat capacity data. The vertical arrows indicate the onset of AF4 phases for different Ni concentration. The inset shows the heat capacity of pure $MnWO_4$ which shows additional phase transition into AF1 phase at 7.6 K. . . . .	76
4.16	Temperature dependence of the wave vector scan of AF2 and AF4 phases for $Mn_{1-x}Ni_xWO_4$ . The AF4 and AF2 phases are coexisting for $x = 0.2$ below 9 K. The colors of the images represent the intensities of magnetic reflections in corresponding phases. . . . .	78
4.17	(a) Integrated intensities of magnetic reflections of AF2 phase [10]. (b) Integrated intensities of the magnetic reflections of AF4 phase. The intensity and $T_C$ of the AF2 phase decrease with increased Ni content while the intensity and $T_N$ of the AF4 phase increase with increased Ni content. For $x = 0.15$ and $0.2$ , the two phases are coexisting at low temperature. . . . .	79
4.18	Ferroelectric polarization in $Mn_{1-x}Ni_xWO_4$ for different $x$ values along the $b$ -axis. The $P_b$ of $Mn_{1-x}Ni_xWO_4$ is smaller than the extrapolated $P_b$ of $MnWO_4$ . Above 10% Ni doping, the $P_b$ quickly drops and reverses sign at low temperature and completely vanishes above 20% Ni doping. . . . .	82
4.19	Evolution of the magnetic and multiferroic phases with Ni concentration. The phase diagram is derived from magnetic and heat capacity data which is in agreement with neutron diffraction and polarization measurement. The $T_C$ decreases and $T_N$ increases above 10% Ni doping. The AF2 and AF4 phases coexist between 15% to 30% Ni doping. The dotted line shows the extrapolation to low temperature. . . . .	83
4.20	(a) Magnetic unit cell (supercell) of $GdMn_2O_5$ in the commensurate phase. The arrows show the direction of magnetic moment of respective ions. The $Gd^{3+}$ ions are surrounded by $Mn^{3+}$ - $Mn^{3+}$ - $Mn^{4+}$ - $Mn^{3+}$ - $Mn^{4+}$ repeating units in the $a - b$ plane. The labelled pair of $Mn^{3+}$ - $Mn^{4+}$ ions are frustrated and produce lattice distortion to minimize frustration. (b) Ferroelectric $T_C$ of $RMn_2O_5$ vs ionic radii of rare-earth ions. The $T_C$ 's are extracted from [11, 12, 13, 14, 15, 16]. . . . .	87
4.21	Temperature dependence of the dielectric constant of $GdMn_2O_5$ at different pressure values. The new dielectric peak observed above $P_C$ moves to higher temperature with pressure. The inset shows the dielectric constant and dielectric loss $\tan(\delta)$ at ambient pressure. . . . .	89

4.22	Pressure effect on FE polarization of $\text{GdMn}_2\text{O}_5$ . (a) A new FE phase is observed above $P_C$ in the incommensurate paraelectric region. (b) Large scale view of the new FE phase at higher temperature. The $P_b$ and $T_{C2}$ both increase with pressure. . . . .	92
4.23	P-T phase diagram of $\text{GdMn}_2\text{O}_5$ up to 18 kbars [17]. The $T_N$ and $T_{C2}$ increase, while $T_{C1}$ decreases with pressure. . . . .	93
4.24	Thermal expansion measurement of $\text{GdMn}_2\text{O}_5$ using high precision capacitance dilatometer. (a) The relative length change along the three crystallographic axes. Lattice anomalies are observed at the ferroelectric and magnetic transitions. (b) The relative volume change is calculated from the change in length of the sample. The volume of incommensurate phase is smaller than the volume of the high-temperature paramagnetic phase and the low-temperature commensurate phase. The volume increases at the FE transition in the commensurate phase.	96
4.25	Heat capacity of $\text{GdMn}_2\text{O}_5$ at constant pressure. The two anomalies are observed at $T_N = 40$ K and $T_{C1} = 30$ K. The inset shows the abrupt change in heat capacity ( $C_p/T$ ) at the ferroelectric transition.	97
4.26	The Gd-Mn <sup>3+</sup> antiferromagnetic zigzag chains along the $c$ -axis. Only Mn <sup>3+</sup> ions are labelled in the image and the smallest spheres indicate oxygen ions. The arrows show the direction of spins in the commensurate phase. . . . .	99
4.27	Pressure effect on the ferroelectric properties of $\text{TmMn}_2\text{O}_5$ up to 16.6 kbars. The $P_b$ drops to lower value in the incommensurate phase. The commensurate region slightly increases under pressure. . . . .	102
4.28	Pressure effect on the magnetic transition of $\text{DyCrO}_3$ . The mutual inductance data are vertically offset by constant values for better visualization. . . . .	105
4.29	Pressure effect on the magnetic transition of $\text{HoCrO}_3$ (unpublished). The mutual inductance data are vertically offset by constant values for better visualization. . . . .	106
4.30	Pressure effect on the magnetic transition of $\text{Ho}_{0.7}\text{Dy}_{0.3}\text{CrO}_3$ . The mutual inductance data are vertically offset by constant values for better visualization. . . . .	107

4.31	Pressure dependence of the Néel temperature of $\text{RCrO}_3$ (unpublished). The $T_N$ values are extracted from the peak positions of warming data. The inset image of one of the sample used for mutual induction mea- surement winded with two Cu coils. . . . .	109
------	---	-----

# List of Tables

4.1	Magnetocrystalline anisotropy of the transition metal ions in $\text{TWO}_4$ ( $\text{T} = \text{Mn, Cu, Fe, Co, Ni}$ ) in $a-c$ plane. $\theta_a$ is the anisotropy angle with respect to the $a$ -axis in the $a-c$ plane. These values are referenced from [18, 19]. . . . .	71
4.2	Refined magnetic structure parameters of $\text{Mn}_{1-x}\text{Ni}_x\text{WO}_4$ for $x = 0.05, 0.10, 0.15, 0.30$ at 5 K and 10 K. $\Theta$ is the angle made by $\mathbf{m}_{\perp b}$ with $a$ -axis. . . . .	80

# Chapter 1

## Introduction

In recent years, technological advancements in electronic devices and communications have greatly benefited society and this results from devices becoming continually smaller and smaller and their operating speeds becoming faster and faster everyday. Artificial intelligence and machine-learning are also hot fields currently, where developments are directly correlated to the advancements in material research and the utilization of specific material properties to design new materials. One specific interesting class of materials are functional materials, named such for their properties or functions that are inherent to the material. Discovery of new functional materials for technological applications requires a deep understanding of the fundamental properties at stationary states as well as their dynamics under perturbations and extreme conditions. Ferroic materials are one of many classes of functional materials which are extensively used in applications and are most commonly known as ferromagnets, ferroelectrics etc. As ferroic materials have a memory, this makes

them an ideal match to be utilized in industry and research as memory, data storage devices as well as sensors; just to name a few applications.

If two or more primary ferroic orders coexist in the same material, it is defined as a multiferroic material. The associated ferroic property can be ferromagnetic (FM), ferroelectric (FE), ferroelastic or ferrotoroidic, as well as antiferromagnetic (AFM) order are also included in the multiferroic class of materials. Here we consider those multiferroics that have any type of magnetic order which shows ferroelectric polarization. If cross coupling between these ferroic orders exists, then the material is magnetoelectric (ME). In such materials, magnetization (polarization) can be controlled by an electric field (magnetic field). The upper bound of linear ME coupling in ME medium is limited by  $\alpha_{ij}^2 \leq \chi_{ii}^e \chi_{jj}^m$ , where  $\alpha_{ij}$  is the ME susceptibility and  $\chi_{ii}^e, \chi_{jj}^m$  are the ferroelectric and magnetic susceptibilities [20]. The multiferroic materials exhibit both magnetic and electric susceptibilities that have large values in the vicinity of phase transition and could display large ME susceptibility.

The first experimental evidence of the ME effect was reported in  $\text{Cr}_2\text{O}_3$  in 1960 [21, 22] after the theoretical prediction by Dzyaloshinskii in 1959 [23]. A sizable coupling between the magnetic and the ferroelectric order was observed in hexagonal  $\text{YMnO}_3$  in 1997 [24]. After the discovery of magnetoelectric effect in multiferroic  $\text{TbMnO}_3$  [25, 26] in 2003, a resurgence was seen in the research of multiferroics. The continuous growth of interest in this research field is demonstrated in Fig.4.2, which gives a visualization of the number of publications per year with topic multiferroic/magnetoelectric retrieved from the Web of Science and shows a rapid increase of publications over recent years.

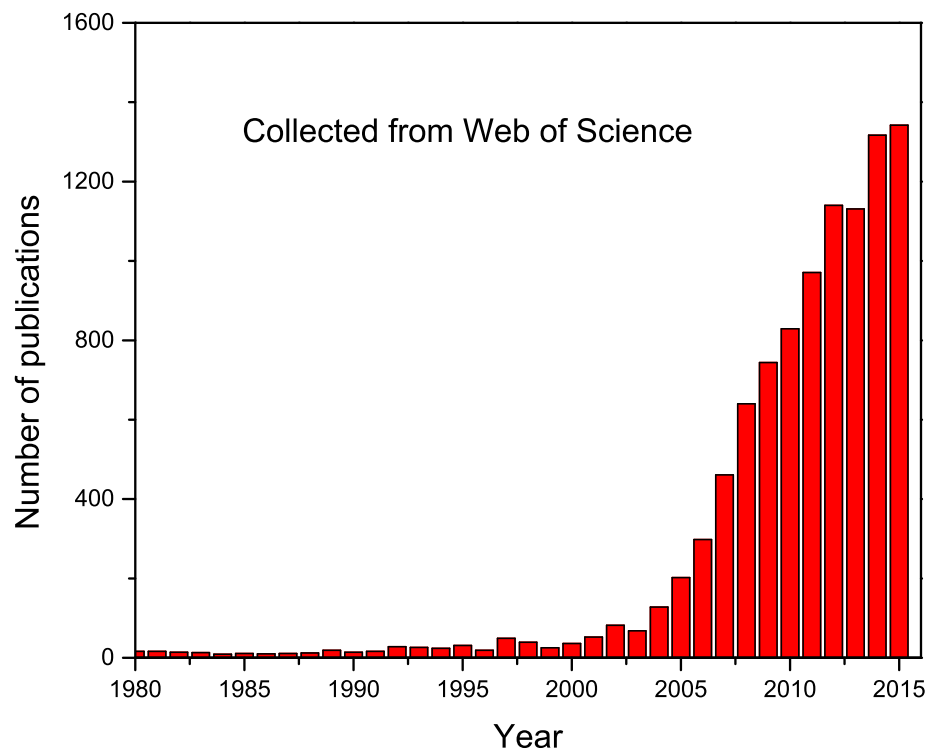


Figure 1.1: Number of publications per year on the topic of multiferroic or magnetoelectric materials. The data were collected from the Web of Science.

Our goal is to understand the fundamental physics associated with different classes of multiferroics under perturbation. In particular, we studied the effect of the magnetic field, pressure and chemical doping in type II multiferroics. For better device performance, a robust ME effect is necessary. In many multiferroic systems, the ME effect is enhanced by external perturbations [25, 27] and in some cases shows interesting and exotic phenomena. Although intensive research in multiferroics has occurred over the past 15 years, many questions are still left unanswered which will allow multiferroic materials to better utilized in device applications and possibly lead to new devices.

In this work, we investigated the effect of magnetic field in the phase diagram of  $\text{Mn}_{1-x}\text{Co}_x\text{WO}_4$  ( $x = 0.05, 0.135, 0.15, 0.17$ ), where it is discovered that the strong coupling of different coexisting magnetic domains reverses the polarization in  $\text{Mn}_{0.85}\text{Co}_{0.15}\text{WO}_4$ . The anisotropy effect of the magnetic ions suppresses the polarization in  $\text{Mn}_{1-x}\text{Ni}_x\text{WO}_4$  above  $x = 0.10$ . It is also interesting to note that pressure induced a new ferroelectric phase at a higher temperature in  $\text{GdMn}_2\text{O}_5$  by decoupling of the Gd moments and the Mn spins above a critical pressure. These results give insight into how a small perturbation affect frustrated multiferroics, as they are highly sensitive to external perturbations.

The proceeding chapter, Chapter 2, will provide a broad overview of the basic phenomena critical to this work: magnetic order, multiferroics and pressure effects. Chapter 3 will cover all methods pertinent to sample preparation as well as measurement techniques, with Chapter 4 covering results and a discussion. Finally, Chapter 5 will summarize and provide future perspective and opportunities.

# Chapter 2

## Background

In this chapter, I will provide a short introduction to the fundamental properties and terminologies used in solid state physics to facilitate a discussion in following chapters for all experimental results to be presented in this work.

### 2.1 Dielectric constant

In electrostatics, the polarization of the medium by an electric field is expressed as

$$\mathbf{P} = \epsilon_o \chi_e \mathbf{E} \tag{2.1}$$

provided that the field is not too strong. The proportionality constant  $\chi_e$  is the electric susceptibility of the medium and  $\epsilon_o$  is introduced to make  $\chi_e$  dimensionless. Materials which follow Eq. 2.1 are called linear dielectrics. The electric field  $\mathbf{E}$

in Eq. 2.1 is the total field due to the free charges and an induced polarization. In such a case, if a dielectric is placed in an external field  $\mathbf{E}_o$ , then we can not compute  $\mathbf{P}$  directly from Eq. 2.1. The external field will polarize the material and the polarization will produce its own field, which then contributes to the total field, and in turn, modifies the polarization. The simplest approach is, to begin with the displacement  $\mathbf{D}$ , which can be deduced directly from the free charge distribution. In a linear media, we can write

$$\mathbf{D} = \epsilon_o \mathbf{E} + \mathbf{P} = \epsilon_o \mathbf{E} + \epsilon_o \chi_e \mathbf{E} = \epsilon_o (1 + \chi_e) \mathbf{E} = \epsilon \mathbf{E} \quad (2.2)$$

So  $\mathbf{D}$  is also proportional to  $\mathbf{E}$ . In Eq. 2.1,  $\epsilon_o$  is permittivity of free space and the new constant  $\epsilon = \epsilon_o(1 + \chi_e)$  is the permittivity of material. The dimensionless quantity  $\epsilon_r = 1 + \chi_e = \frac{\epsilon}{\epsilon_o}$  is called the relative permittivity or the dielectric constant of the material.

## 2.2 Ferroic order

If a material has any long-range ordered microscopic property which gives rise to a measurable macroscopic property that can be aligned and switched by external fields, then these materials are defined as ferroic materials. The macroscopic physical quantity that arises in the ferroic state as a result of a spontaneous phase transition and characterizes the reduced symmetry state of the material is called order parameter. In the ferroic state, there are at least two degenerate states which only differ in their orientations of the corresponding order parameters. These degenerate states

are separated by domain walls. If the orientational switching of an order parameter requires only one kind of external field like an electric field or a magnetic field or even a stress field, then these ferroics are called primary ferroic materials. If the combination of two kinds of fields mentioned above is required for switching, then these are known as secondary ferroic materials. The ferroic state is the reduced symmetry state which has a lower symmetry than the prototype phase. All ferroic materials show characteristic hysteric behavior in the ordered state if a field is applied.

## 2.3 Ferroelectricity

The materials which show a spontaneous polarization and can be switched by external electric field are ferroelectric materials. Ferroelectrics are non-centrosymmetric, where the center of positive charges does not coincide with the center of the negative charges. The plot of the polarization versus the electric field exhibits a hysteresis, which is a typical feature of ferroic materials. The polarization appears due to the symmetry breaking phase transition below the certain transition temperature ( $T_c$ ). Above  $T_c$ , the polarization vanishes and the material is called a paraelectric; which is similar to the paramagnetic state in magnetism. In some non-centrosymmetric materials, the spontaneous polarization can not be switched by reversing the electric field although the spontaneous polarization is observed by changing temperature are called pyroelectric materials.

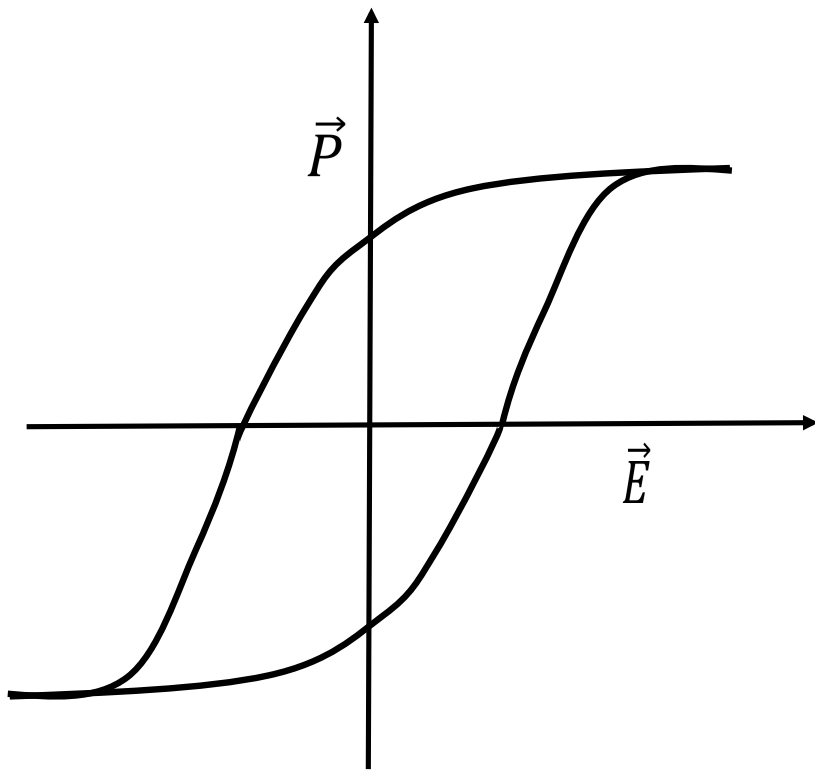


Figure 2.1: A typical P - E hysteresis loop in ferroelectric materials.

## 2.4 Proper and improper ferroelectrics

The ferroelectric state of the material below ( $T_C$ ) is characterized by an order parameter known as polarization ( $\mathbf{P}$ ). If the polarization is primary order parameter in the ferroelectric crystal, then it is proper ferroelectric, e.g.,  $\text{BaTiO}_3$ . In some materials, the polarization arises in the crystal as a secondary effect by the consequence of other order parameters; called improper ferroelectrics. Most of the magnetic ferroelectrics are improper ferroelectrics, where magnetization (ordered spin arrangement) becomes the primary order parameter and polarization becomes secondary order parameter, for instance,  $\text{MnWO}_4$ . In those cases, the spin order breaks the inversion symmetry, which may transfer to the lattice site and thereby induces the polarization.

## 2.5 Polarization and surface charge density

The potential due to an electric dipole of dipole moment  $\mathbf{p}$  at a distance  $r$  with the unit vector  $\mathbf{r}$  in CGS units is

$$\phi(r) = \frac{\mathbf{p} \cdot \mathbf{r}}{r^2} = -\mathbf{p} \cdot \nabla\left(\frac{1}{r}\right) \quad (2.3)$$

if there are  $n$  dipoles per unit volume, then the potential due to unit volume is

$$\phi(r) = -\mathbf{P} \cdot \nabla\left(\frac{1}{r}\right) \quad (2.4)$$

where  $\mathbf{P} = n\mathbf{p}$  is the dipole moment per unit volume defined as the polarization.

The potential now can be written as

$$\phi(r) = -\frac{1}{r}\nabla \cdot \mathbf{P} + \nabla \cdot \left(\frac{\mathbf{P}}{r}\right). \quad (2.5)$$

The total potential due to the volume distribution of electric dipoles can be found by integrating the Eq. 2.5 over the entire volume

$$\phi(r) = \int \left(-\frac{1}{r}\nabla \cdot \mathbf{P} + \nabla \cdot \left(\frac{\mathbf{P}}{r}\right)\right) dV \quad (2.6)$$

applying Gauss's divergence theorem we get,

$$\phi(r) = \int \left(-\frac{1}{r}\nabla \cdot \mathbf{P}\right) dV + \oint \left(\frac{1}{r}\right) \mathbf{P} \cdot d\mathbf{a} \quad (2.7)$$

The first term in Eq. 2.7 corresponds to the potential due to a volume charge density where  $\rho_b = -\nabla \cdot \mathbf{P}$  and the second term corresponds to the potential due to a surface charge density where  $\sigma_b = \mathbf{P} \cdot \mathbf{n}$ . In the case of an insulator,  $\nabla \cdot \mathbf{P} = 0$  and the polarization is equivalent to the surface charge density,  $Q/A$ , where  $A$  is the surface area of the material. If the insulating surface is provided with some conducting medium and electrodes, then it is possible to measure the pyroelectric current.

## 2.6 Landau theory of ferroelectric phase transition

In 1946, V. L. Ginzburg explained the phase transition in ferroelectrics using Landau's theory of phase transition where the free energy  $F$ , in the vicinity of phase

transition can be written in power series utilizing the order parameter  $\mathbf{P}$ , as in [28].

$$F(\mathbf{P}, T, \mathbf{E}) = -\mathbf{E}\mathbf{P} + g_o + \frac{1}{2}g_2\mathbf{P}^2 + \frac{1}{4}g_4\mathbf{P}^4 + \frac{1}{6}g_6\mathbf{P}^6 + \dots \quad (2.8)$$

where  $\mathbf{E}$  is the electric field and the coefficients  $g_n$  is temperature dependent. The free energy only contains even power in  $\mathbf{P}$  with respect to the inversion symmetry above the phase transition. At equilibrium, the polarization in an applied electric field  $\mathbf{E}$  is given by the minimum of  $F$ ,

$$\frac{\partial F}{\partial \mathbf{P}} = -\mathbf{E} + g_2\mathbf{P} + g_4\mathbf{P}^3 + g_6\mathbf{P}^5 + \dots = 0. \quad (2.9)$$

In order to set the ferroelectricity in material,  $g_2$  has to be of the form  $g_2 = \gamma(T - T_o)$  where  $\gamma$  is positive constant. The second-order phase transition happens if  $g_4 > 0$  and  $g_6$  is neglected. So the Eq. 2.9 becomes

$$\gamma(T - T_o)\mathbf{P}_s + g_4\mathbf{P}_s^3 = 0. \quad (2.10)$$

The solutions of Eq. 2.10 are  $\mathbf{P}_s = 0$  and  $\mathbf{P}_s^2 = (\frac{\gamma}{g_4})(T_o - T)$ . For  $T \geq T_o$ ,  $\mathbf{P}_s = 0$ , as  $\gamma$  and  $g_4$  are both positive which defines Curie temperature as  $T_o$ . For  $T < T_o$  with no applied electric field

$$|\mathbf{P}_s| = \left(\frac{\gamma}{g_4}\right)^{\frac{1}{2}}(T_o - T)^{\frac{1}{2}}, \quad (2.11)$$

by plotting Eq. 2.11, it is observed that  $\mathbf{P}_s$  goes to zero continuously at the transition temperature, which implies a second-order phase transition.

First-order phase transitions can also be explained from Eq. 2.8 if  $g_4$  is negative and  $g_6$  is positive. At equilibrium condition for  $\mathbf{E} = 0$

$$\gamma(T - T_o)\mathbf{P}_s - |g_4|\mathbf{P}_s^3 + g_6\mathbf{P}_s^5 = 0, \quad (2.12)$$

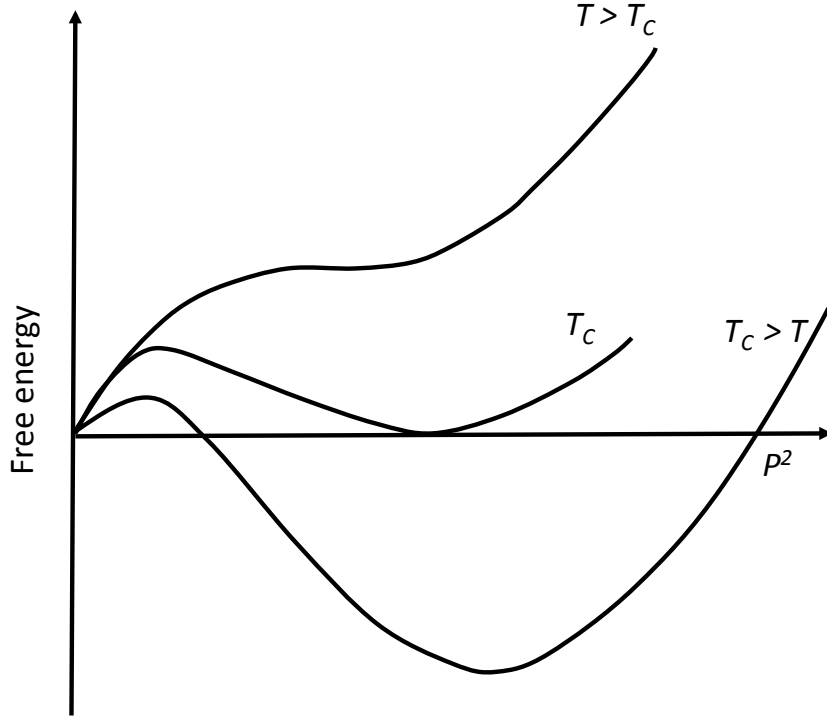


Figure 2.2: Landau free energy as a function of  $P^2$  in the first-order phase transition.

where the solutions are either  $\mathbf{P}_s = 0$  or  $\mathbf{P}_s$  is given by

$$\gamma(T - T_o) - |g_4|\mathbf{P}_s^2 + g_6\mathbf{P}_s^4 = 0. \quad (2.13)$$

Fig. 2.2 shows that at  $T = T_C$ , the free energy becomes equal in disordered (paraelectric) and ordered (ferroelectric) phases and the order parameter jumps from 0 to  $\mathbf{P}_s$ . For  $T > T_C$ , the disordered phase is stable whereas the ordered phase is stable for  $T_C > T$ .

## 2.7 Magnetic properties of solids

Magnetism in solids arises from the angular momentum (spin and orbital) of electrons of the atoms. At high temperatures, the spins have random orientations in a paramagnetic order due to relatively large thermal energy  $\kappa_B T$  compared to that of the magnetic energy. At low temperature, these spins correlate and then order in a certain type of long-range order below some critical temperature ( $T_C$ ), where the spins may arrange in parallel (ferromagnetic), antiparallel (antiferromagnetic) or some other orientation. Below  $T_C$ , a macroscopic physical quantity defines the magnetically ordered system known as magnetization ( $M$ ). According to Curie law, the paramagnetic susceptibility for noninteracting spins is defined as

$$\chi = \frac{C}{T} \quad (2.14)$$

where  $C$  is the Curie constant.

When the spins are aligned in a ferromagnetic order, the exchange field  $\mathbf{B}_E$  is proportional to the magnetization  $\mathbf{M}$ , i.e.,

$$\mathbf{B}_E = \lambda \mathbf{M}, \quad (2.15)$$

where  $\lambda$  is a constant independent of temperature. If  $\mathbf{B}_a$  is the applied magnetic field for the paramagnetic phase and  $\mathbf{B}_E$  is the exchange field, then the paramagnetic susceptibility can be written as

$$\chi_p = \frac{M}{\mathbf{B}_E + \mathbf{B}_a}. \quad (2.16)$$

Using Eq. 2.14 and Eq. 2.21 in Eq. 2.22,

$$\chi = \frac{\mathbf{M}}{\mathbf{B}_a} = \frac{C}{T - C\lambda} = \frac{C}{T - T_c}. \quad (2.17)$$

Eq. 2.14 is the Curie-Weiss law in magnetism where  $T_c = C\lambda$  is the characteristic Curie temperature. The  $\chi$  blows up at  $T = T_c$  and spontaneous magnetization exists below  $T_c$ .

In antiferromagnetic materials, the characteristic temperature is the Néel temperature  $T_N$  below which antiferromagnetic domains are formed. If two antiferromagnetic sublattices A and B have equal magnetization, then  $C_A = C_B = C$  and the Néel temperature in the mean field approximation is given by

$$T_N = \mu C, \quad (2.18)$$

where  $\mu$  is a constant independent of temperature. The susceptibility in paramagnetic region can be written as

$$\chi = \frac{2C}{T + T_N}, \quad (2.19)$$

whereas the experimental results above  $T_N$  follows

$$\chi = \frac{2C}{T + \theta}, \quad (2.20)$$

and is independent of field orientation above  $T_N$ .  $\theta$  is the Curie-Weiss temperature. In many antiferromagnetic materials, the ratio  $\frac{\theta}{T_N}$  is different than unity. So the higher-order interaction and lattice geometry of sublattices should be considered to

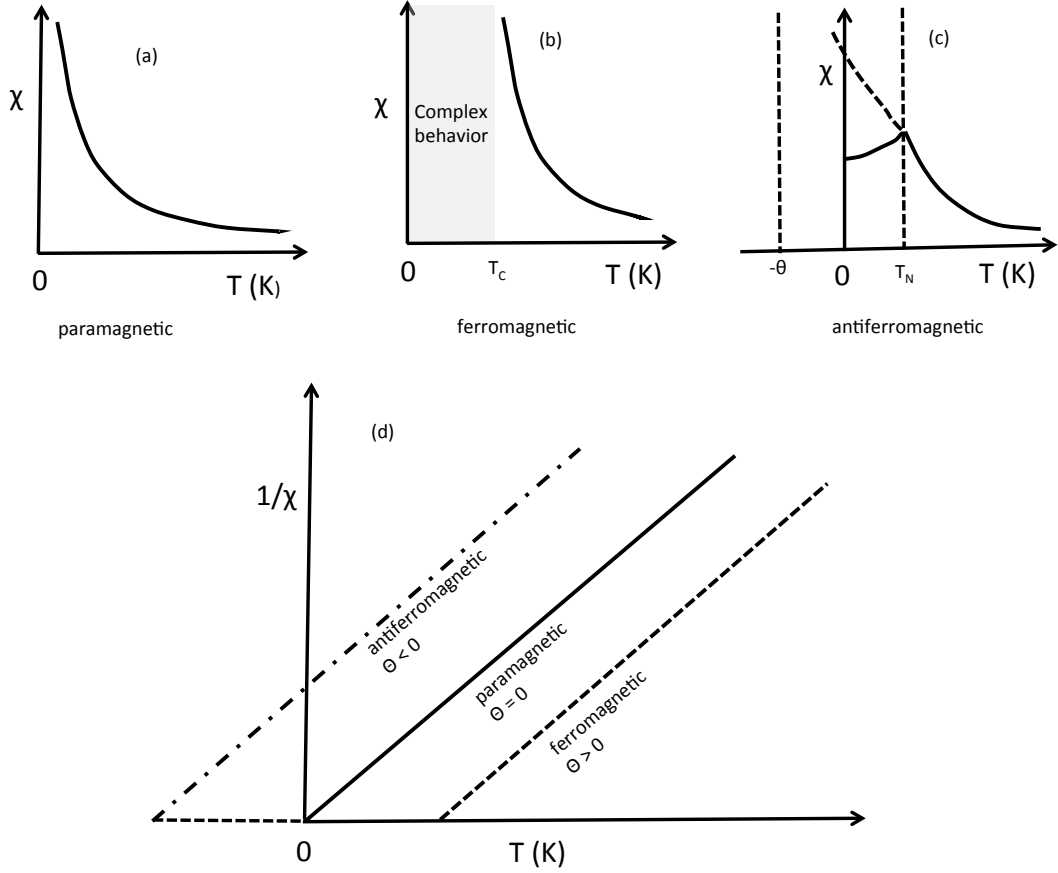


Figure 2.3: Temperature dependence of the magnetic susceptibility and its inverse in paramagnetic, ferromagnetic and antiferromagnetic materials.

get the observed value of  $\frac{\theta}{T_N}$ . Below  $T_N$ , the susceptibility depends on the orientation of the magnetic field. If the applied field  $\mathbf{B}_a$  is perpendicular to the spin orientation, then the susceptibility remains nearly constant ( $\chi_{\perp} = 1/\mu$ ). In contrast, if the field is parallel to the spin orientation, then the susceptibility decreases with temperature and becomes zero at  $T = 0$  K, i.e.,  $\chi_{\parallel}(0) = 0$ . The temperature dependent susceptibilities of different magnetic orders are shown in Fig. 2.3 (a), (b) and (c).

## 2.8 Magnetic frustration

Magnetic frustration in solids can arise either from geometric constraint or from competing magnetic exchange interactions. Geometric frustration can lead to some type metastable spin order which gives rise to frustration. On the other hand, if the next nearest neighbor interaction is significant compared to nearest neighbor interaction, then all the interacting pairs can not minimize their energy at the same time. In this case, the magnetic system prefers a new ground state in which any small perturbation can switch the system into different ground states. Therefore, frustration can possibly induce a large number of complex magnetic phases. In some cases, frustration leads to a lattice distortion via a magnetoelastic coupling, which breaks the inversion symmetry and induces ferroelectricity. The best magnetic phase which can produce a large ferroelectric polarization than the existing known frustrated phases may have been still elusive. As a result of magnetic frustration, in most of the cases, the magnetic unit cell becomes the supercell of the crystallographic unit cell. If the periodicity of the supercell is some integral multiple of the conventional unit cell, then the magnetic order is commensurate with lattice periodicity. In many cases, for instance, the spiral magnetic order, the periodicity of the magnetic unit cell does not follow the integral multiplicity of the conventional unit cell and the magnetic order becomes incommensurate with lattice periodicity. In strongly frustrated systems, the magnetic order switches between commensurate-incommensurate order below  $T_N$ .

## 2.9 Multiferroics

If a material has two or more coexisting ferroic orders in a single phase, it is called multiferroic material. The ferroic orders can be ferromagnetic/antiferromagnetic, ferroelectric, ferroelastic and ferrotoroidic. In this report, the term multiferroic means the coexistence of any type of magnetic and ferroelectric order in the same phase of the material. Both time reversal and space inversion symmetries are broken in the multiferroic phases of these materials as the magnetic order breaks the time reversal symmetry and polarization requires the breaking of space inversion symmetry.

Multiferroics are classified into two classes: type I and type II. When the two order parameters arise from different origins, then the material is classified as type I multiferroic. In these materials, ferroelectricity generally appears well above the room temperature due to a structural transition and the magnetic order arises below room temperature. The magnetoelectric effect is weak as the coupling between the order parameters is weak; however, some anomalies in the polarization can be observed at the magnetic transitions. Hexagonal  $\text{RMnO}_3$  ( $\text{R} = \text{rare earth}$ ) are some examples of type I multiferroics.

In contrast to type I multiferroics, a strong magnetoelectric effect is found in type II multiferroics and is a result of the strong coupling between the spin and charge degrees of freedom. Certain types of magnetic order, such as a spiral magnetic order, can break the inversion symmetry as shown in Fig. 2.4(b) via an antisymmetric Dzyaloshinski-Moriya (DM) exchange interaction [29] and thereby induces a polarization; so called magnetic ferroelectrics. The induced polarization is small in these

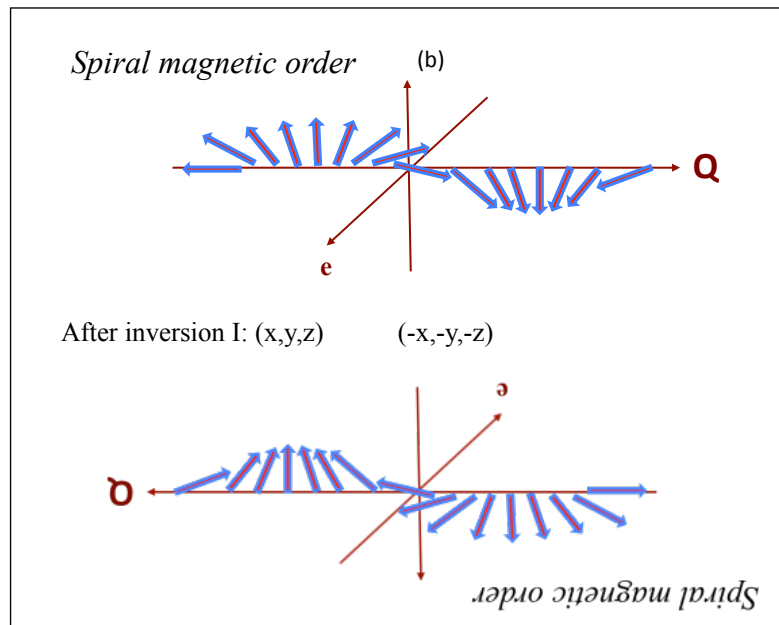
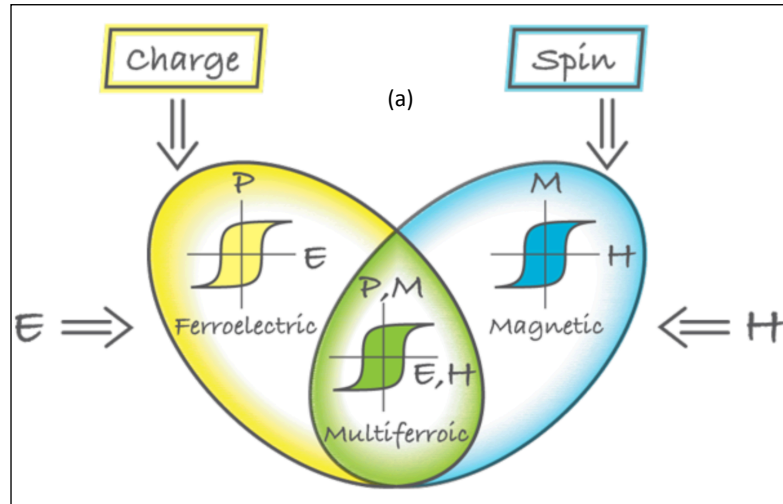


Figure 2.4: (a) Multiferroics combining the ferroelectric and ferromagnetic order in the same phase. (b) Inversion symmetry breaking by a spiral magnetic order under space inversion. The image (a) is taken from ref. [1]

multiferroics as DM interaction requires spin-orbit coupling that is mediated by a relativistic effect. Some examples of spiral magnetic ferroelectrics are TbMnO<sub>3</sub> [25], MnWO<sub>4</sub> [30], CoCr<sub>2</sub>O<sub>4</sub> [31], LiCu<sub>2</sub>O<sub>2</sub> [32], Ni<sub>3</sub>V<sub>2</sub>O<sub>8</sub> [33], CuO [34]. In addition to the spiral order, a collinear magnetic order with different charges on the magnetic ion can also induce polarization via exchange striction mechanism in different multiferroics including RMn<sub>2</sub>O<sub>5</sub> [35, 36, 37]. Since the ferroelectric order depends on magnetic order, the critical temperature of ferroelectric ordering in type II multiferroics is equal or lower than the Néel temperature.

## 2.10 Ferroelectricity in spiral magnets

The frustrated magnetic system may stabilize a spiral magnetic order as shown in Fig. 2.5(b) if  $|\frac{J'}{J}| > \frac{1}{4}$ , where  $J$  and  $J'$  represent the nearest and the next nearest neighbor interactions.

The phenomenological theory of spiral magnets which gives ferroelectric polarization is explained by Mostovoy [38]. Under space inversion  $x \rightarrow -x$ ,  $\mathbf{P} \rightarrow -\mathbf{P}$  and  $\mathbf{M} \rightarrow \mathbf{M}$ . Under time reversal  $t \rightarrow -t$ ,  $\mathbf{P} \rightarrow \mathbf{P}$  and  $\mathbf{M} \rightarrow -\mathbf{M}$ .

The free energy in terms of the order parameter  $\mathbf{P}$  and  $\mathbf{M}$  can be expressed as

$$F = \frac{P^2}{2\chi_e} - \gamma \mathbf{P} \cdot [\mathbf{M}(\nabla \cdot \mathbf{M}) - (\nabla \cdot \mathbf{M})\mathbf{M}] + \dots \quad (2.21)$$

Eq. 2.21 is invariant under space inversion and time reversal symmetry as free energy should be invariant under all variations of the symmetry operations above the phase transition. When minimizing with respect to the order parameter  $\mathbf{P}$  and

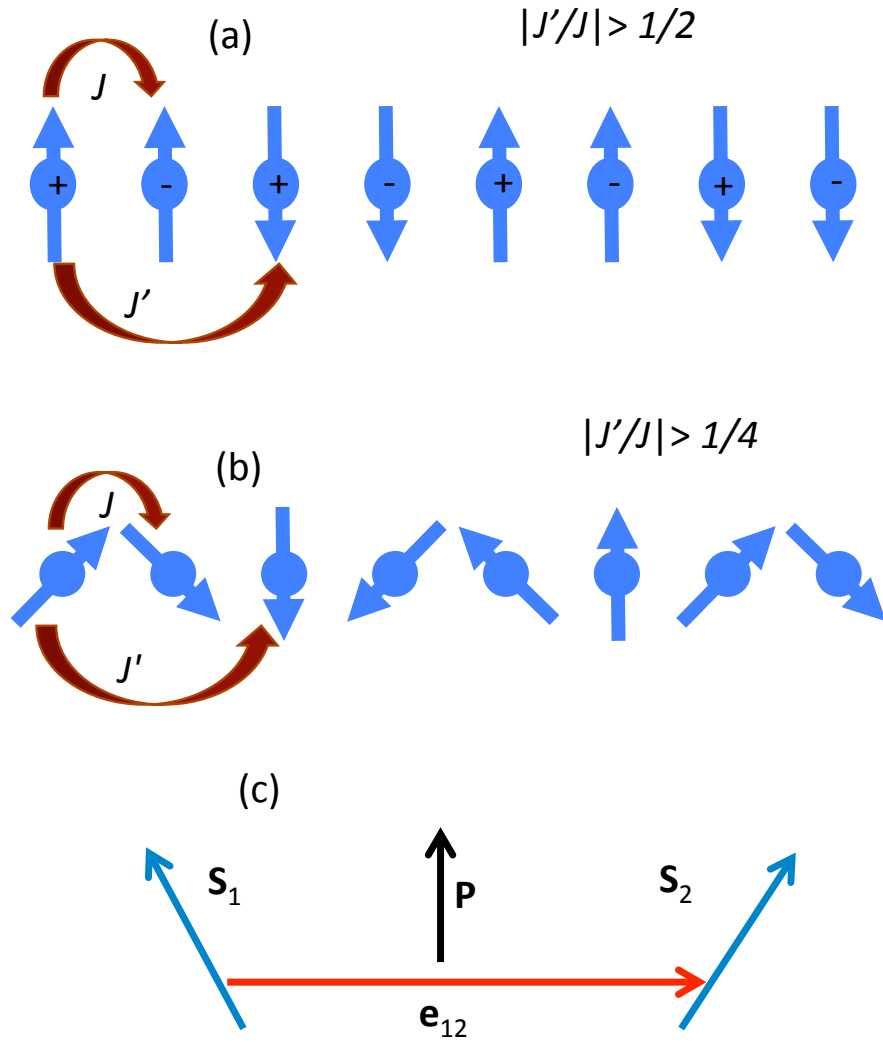


Figure 2.5: (a) Collinear E-type ( $\uparrow\downarrow$ ) spin structure. The collinear spin structure is formed if  $J'/J > 1/2$ . The + and - sign means the neighboring ions have different valence states (different charges) and induce ferroelectricity. (b) Spiral spin structure. The spiral spin structure is formed if  $J'/J > 1/4$ . (c) Polarization induced by two non-collinear spins.

neglecting higher-order terms, Eq. 2.21 can be rewritten as

$$\mathbf{P} = \gamma\chi_e[\mathbf{M}(\nabla \cdot \mathbf{M}) - (\nabla \cdot \mathbf{M})\mathbf{M}], \quad (2.22)$$

for spiral magnet describing the helical order,  $\mathbf{M}$  can be expressed as

$$\mathbf{M} = M_1\mathbf{e}_1\cos\mathbf{Q} \cdot \mathbf{x} + M_2\mathbf{e}_2\sin\mathbf{Q} \cdot \mathbf{x} + M_3\mathbf{e}_3, \quad (2.23)$$

when substituting in Eq.2.22,

$$\mathbf{P} = \gamma\chi_e M_1 M_2 [\mathbf{e}_3 \times \mathbf{Q}]. \quad (2.24)$$

The induced polarization is perpendicular to both  $\mathbf{e}_3$  and  $\mathbf{Q}$ . If either  $M_1$  or  $M_2 = 0$ , equation 2.23 represents collinear sinusoidal wave and from equation 2.24,  $\mathbf{P} = 0$ . If  $M_1, M_2 \neq 0$ , then it represents the elliptical helix with axis  $\mathbf{e}_3$ . If  $M_3 \neq 0$ , it represents the conical helix. The different types of spiral magnetic orders are shown in Fig. 2.6.

The phenomenological theory of ferroelectricity in spiral magnets is supported by the microscopic model of the spin current theory [39]. The microscopic model of the spin current is based on perturbation theory where the non-collinearity between the spins arises due to competing exchange interactions. The polarization due to the non-collinear spins  $\mathbf{S}_i$  and  $\mathbf{S}_j$  as shown in Fig. 2.5 is given by

$$\mathbf{P} \propto \mathbf{e}_{ij} \times (\mathbf{S}_i \times \mathbf{S}_j), \quad (2.25)$$

which gives the same polarization as given by Eq. 2.24. From Eq. 2.25, it is clear that not all the spiral magnetic order gives rise to ferroelectricity. The polarization vanishes if  $(\mathbf{S}_i \times \mathbf{S}_j) \parallel \mathbf{e}_{ij}$  or  $\mathbf{Q} \parallel \mathbf{e}_{ij}$ .

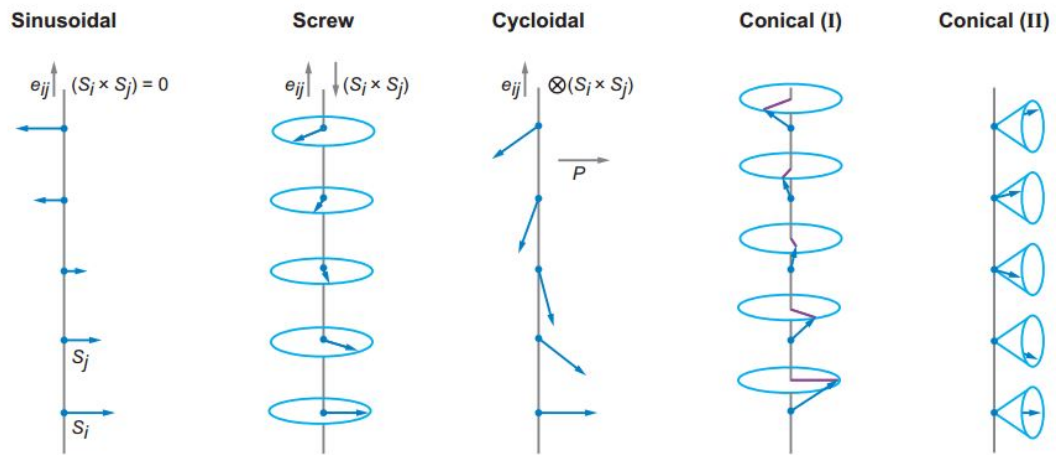


Figure 2.6: Various types of spin orders in frustrated multiferroics. The figure is referenced from [2] with permission.

## 2.11 Ferroelectricity in collinear magnets

In frustrated magnetic systems, ferroelectricity is also observed in the collinear magnetic structure which is mediated by symmetric exchange interaction. If  $|\frac{J'}{J}| > \frac{1}{2}$ , the ground state of the magnetic system would be E-type AFM  $\uparrow\uparrow\downarrow\downarrow$  as shown in Fig. 2.5(a). In this type of spin structure, the inversion symmetry is broken if the charges in two lattice sites are different and ferroelectricity is induced due to lattice distortion [29]. A large polarization compared to the polarization induced by non-collinear spin structure is expected and indeed observed in  $\text{RMn}_2\text{O}_5$  [16, 40]. The exchange interaction in collinear magnets is the Heisenberg type symmetric exchange interaction, which does not involve spin-orbit coupling.

## 2.12 Pressure effect in multiferroics

Pressure can also be used as a tuning parameter for multiferroic properties. Generally speaking, pressure alters the bond distance and bond angles between magnetic cations and ligand ions. In a frustrated magnetic system, this small perturbation may lead to unexpected results in magnetic interactions thus by uncovering a new magnetic ground state. Since the ferroelectric properties are dependent on the magnetic order in type II multiferroics, it is not surprising that these properties also can be altered. Experimental evidence shows that pressure can change multiferroic properties of different materials in many ways [41, 12, 42, 43, 44, 45, 46, 47].

# Chapter 3

## Methods

### 3.1 Sample growth

#### 3.1.1 Single crystal growth of $\text{Mn}_{1-x}\text{Co}_x\text{WO}_4$ and

#### $\text{Mn}_{1-x}\text{Ni}_x\text{WO}_4$

Single crystals of  $\text{Mn}_{1-x}\text{Co}_x\text{WO}_4$  and  $\text{Mn}_{1-x}\text{Ni}_x\text{WO}_4$  ( $0 < x < 0.3$ ) were grown using an optical floating zone furnace with the help of Y. Q. Wang and Dr. B. Lv at TcSUH. The polycrystalline material was synthesized from stoichiometric precursor materials of  $\text{Mn}_2\text{O}_3$ ,  $\text{WO}_3$ , and Co (or Ni for  $\text{Mn}_{1-x}\text{Ni}_x\text{WO}_4$ ) powders via typical solid state reaction. The mixed powder was reacted at 970 °C for 10 hours, reground and then annealed again at the same conditions. The powder X-ray pattern could be well indexed to the monoclinic space group P2/c and showed no signs of impurity phases. The feed rod was prepared by first applying hydrostatic pressure and then sintered

for 10 hours at 1000 °C in a two-step process: first in a horizontal and then vertical furnace. This feed rod was then used in the optical floating zone furnace to grow single crystals, where the Co and Ni content were verified by wavelength-dispersive X-ray spectroscopy (WDS) and was found to be close to the nominal composition. The as-grown crystals cleaved easily and exposed a shiny surface, which is the  $a - c$  plane.

### 3.1.2 Single crystal growth of $\text{RMn}_2\text{O}_5$ ( $\text{R} = \text{Gd}, \text{Tm}$ )

Orthorhombic single crystals of  $\text{GdMn}_2\text{O}_5$  and  $\text{TmMn}_2\text{O}_5$  were grown using flux of  $\text{PbO}/\text{PbF}_2/\text{B}_2\text{O}_3$  in platinum crucible similar to other  $\text{RMn}_2\text{O}_5$ . The mixture was heated at 1280°C for 15 hrs and slowly cooled to 950°C at the rate of 1°C/min. The crystals were grown in Dr. S. W. Cheong's Lab. at Rutgers University. Single crystals of 2 - 4 mm size were used for the measurement.

### 3.1.3 Polycrystal growth of $\text{RCrO}_3$ ( $\text{R} = \text{Ho}, \text{Dy}, \text{Gd}$ )

Polycrystalline samples of  $\text{RCrO}_3$  ( $\text{R} = \text{Ho}, \text{Dy}, \text{Gd}$ ) were grown in Dr. Menka Jain's Lab at the University of Connecticut. The precursor materials  $\text{Dy}(\text{NO}_3)_3$ ,  $\text{Ho}(\text{NO}_3)_3$ ,  $\text{Gd}(\text{NO}_3)_3$  and  $\text{Cr}(\text{NO}_3)_3$  were separately dissolved in water and then mixed together, where citric acid was then added to the mixture as mentioned in ref. [48]. The mixture was dried at 100°C to get a dry powder, which was then annealed at 900°C in oxygen for two hours. The powder was compressed into a pellet shape for dielectric, ferroelectric and magnetic measurements.

## **3.2 Determination of single crystal orientation**

The crystallographic orientations of single crystals were determined by X-ray diffraction using GADDS X-ray diffractometer with the help of Y. Y. Sun and Dr. Z. Wu at HPLT Lab. The crystallographic orientation was determined within  $\pm 3^\circ$ .

## **3.3 Physical property measurement system**

Physical property measurement system (PPMS) from Quantum Design was used for temperature control from room temperature down to 2 K and magnetic fields up to 7 T. A home-made dielectric probe was used for dielectric and pyroelectric measurements which could be inserted into the PPMS from the top. Specific heat measurements were also done using the PPMS which covers the temperature range 1.8 - 400 K.

## **3.4 Magnetic property measurement system**

Magnetic measurements were done using Magnetic Property Measurement System (MPMS) from Quantum Design. MPMS measures the small magnetic signal using the principle of SQUID. The sample in the magnetometer is moved through a detection coil (Fig. 3.1) which picks up the signal and then inductively couples to the SQUID amplifier through a superconducting wire and the signal is converted into a voltage. The MPMS is equipped with a superconducting magnet with a range

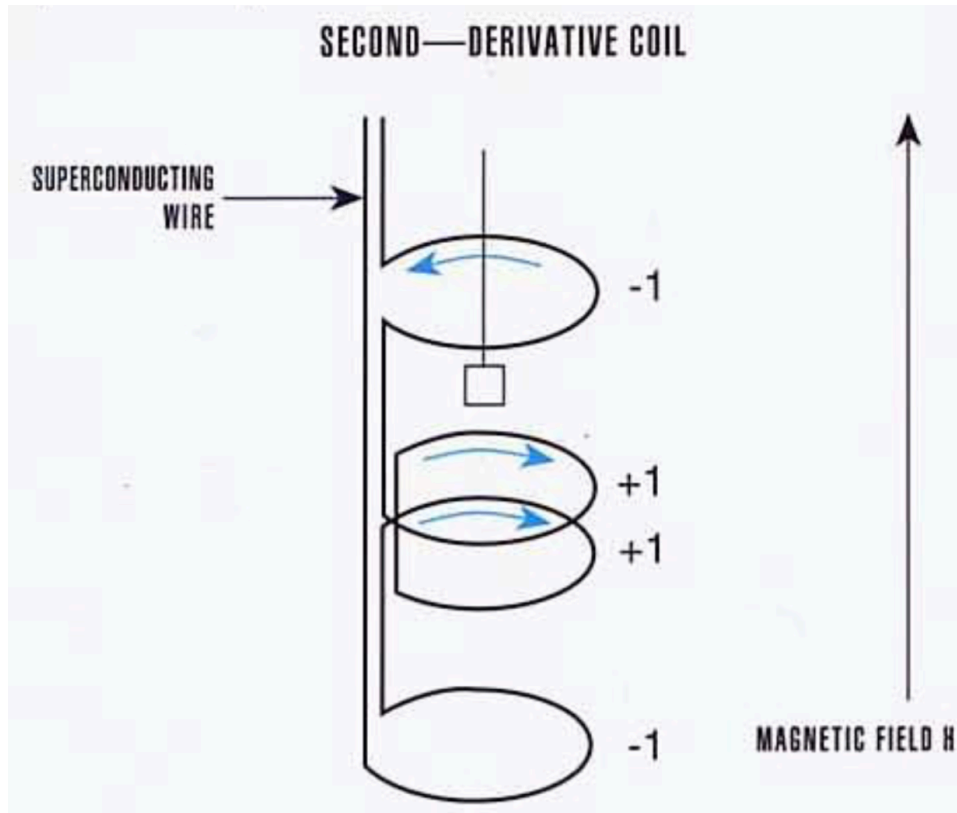


Figure 3.1: Second-order gradiometer superconducting detection coil in MPMS. The figure is taken from ref. [3], fundamentals of magnetism and magnetic measurement system from Quantum Design.

0 - 5 T and a temperature range of 1.8 to 400 K. The SQUID is placed below the magnet inside the superconducting shield.

### 3.5 Dielectric constant measurement

For dielectric measurements, the two surfaces of the sample were made parallel either by cleaving or polishing with sand paper. Electrical contacts were made with

a thin layer of silver paint that was applied on both surfaces and platinum wires were attached with silver paint. Once the sample was mounted on the home-made dielectric probe with the help of GE-varnish, the ends of the platinum wires were soldered to the coaxial cable wired to the probe. Temperature control was provided by the PPMS at the rate of 1 - 2 K/min and the capacitance was measured by Andeen Hagerling (AH 2500A) device at 1 kHz frequency in both cooling and heating cycle. The dielectric constant  $\epsilon_r$  was calculated using Eq.3.1 assuming the sample as parallel plate capacitor, where both the real and the imaginary part of capacitance was measured in each measurement; however, only real part is included in this dissertation. The real part represents the energy stored and imaginary part represents energy loss. The loss factor ( $\tan\delta$ ) was used in data analysis and interpretation. The loss factor also shows anomalies at the ferroelectric transitions. The dielectric constant is given by

$$\epsilon_r = \frac{Cd}{\epsilon_o A}, \quad (3.1)$$

where  $d$  = sample thickness,  $C$  = capacitance of the sample,  $A$  = Area of the sample.

### **3.6 Pyroelectric current and polarization measurement**

The pyroelectric current was measured using a Keithley K6517A electrometer which is capable of measuring current up to 0.1 pA current with great accuracy. The same protocol was used for the sample preparation and mounting on the dielectric

probe as mentioned above in section 3.5. An electric field of 150 kV/m - 300 kV/m was applied using a Keithley K6517A and the pyroelectric current was measured for both forward and reverse biased cases. The temperature of the sample was controlled by PPMS at the average rate of 1 - 2 K/min, where this speed was varied depending on the strength of noise current. The baseline which should be subtracted as background current was determined from the data collected above  $T_C$  as there is no pyroelectric current in the paraelectric region. In some cases, the baseline subtraction becomes tricky if the pyroelectric current is small compared to the noise current or the sample is not perfectly insulating. The observed pyroelectric current was integrated with time, considering no existence of polarization in the paraelectric region, to calculate the polarization using Eq. 3.2, where  $A$  is the contact area of the sample. Fig. 3.2 shows the pyroelectric current of  $\text{GdMn}_2\text{O}_5$  during cooling as a function of temperature.

$$P(t) = \frac{Q}{A} = \frac{1}{A} \int_{t=0}^{t=t'} I(t) dt \quad (3.2)$$

### **3.7 High-pressure measurements of dielectric and pyroelectric current**

For high-pressure measurements of the dielectric and pyroelectric properties, a beryllium-copper (Be-Cu) clamp cell was used. While the cell is primarily made from Be-Cu, a cylindrical Teflon sample holder was prepared to fit inside the Be-Cu

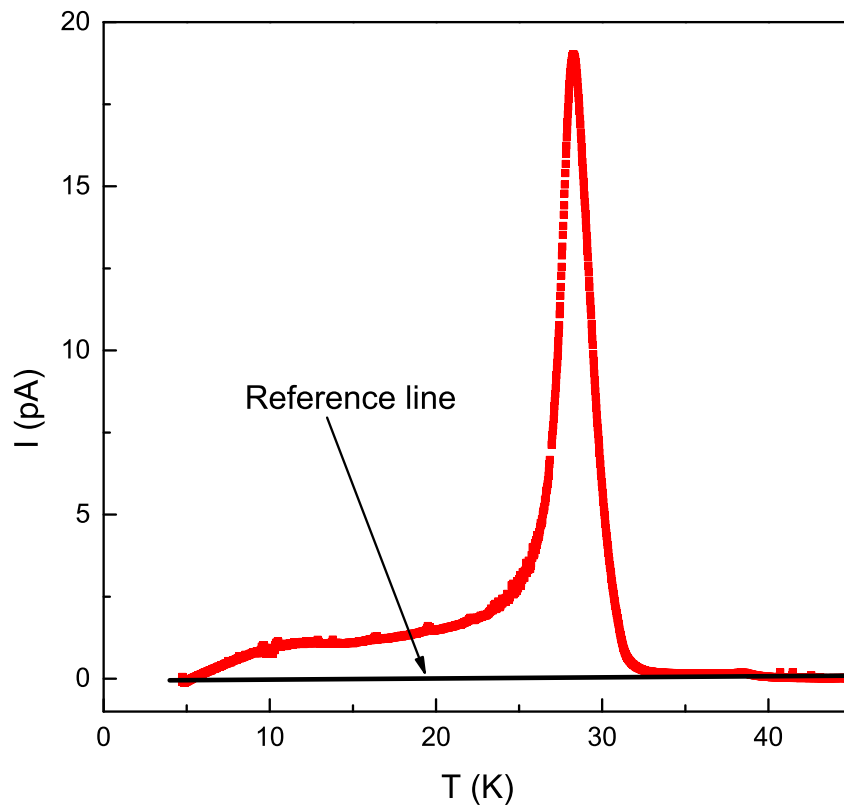


Figure 3.2: Pyroelectric current observed in  $\text{GdMn}_2\text{O}_5$  during cooling cycle. The reference line drawn is used to subtract the background current.

cylinder. The sample (prepared for the measurement in the same way mentioned in section 3.5) goes inside the Teflon sample holder filled with a liquid pressure medium, Fluorinert FC-77. The contact wires are taken out from the small hole on the Be-Cu cap, where the twisted wire pairs are secured with stycast. The Teflon sample holder, along with Be-Cu cap is inserted into the Be-Cu cylinder supplied with two pistons from top and bottom as shown in Fig. 3.3. The cylinder was inserted into the pressure cell and pressure was applied with a hydraulic press. The pressure cell was attached to the probe and inserted into double jacket glass dewar filled with liquid nitrogen (LN2) in the outer space and liquid He<sup>4</sup> in the inner space. The temperature was controlled by moving the pressure cell up-down with respect to the cryostat and temperature was measured by germanium resistor temperature sensor which is mounted in Be-Cu cell body. The *in situ* pressure was measured with a lead manometer, which has a very sharp transition ( $\sim 0.02$  K/min) and a well-studied pressure dependence of the  $T_C$ . The manometer was constructed from a small piece of high purity lead (Pb 99.999%), which was winded with 2 - 4 layers of secondary (inner) coils using 46 gauge copper wire. The manometer was then completed by winding the two layers of primary (outer) coils using 44 gauge copper wire. During the measurement, it was mounted near the sample inside the Teflon sample holder. The primary coil was driven (applied a small current) and the mutual inductance of the secondary coil was measured using 19 Hz LR700. When the lead enters into the superconducting state, a sharp drop in inductance was observed due to the diamagnetic property of superconductor. The mid-point of the sharp drop defines the  $T_C$  of the lead. For reference  $T_C$ , the measurement was also done at

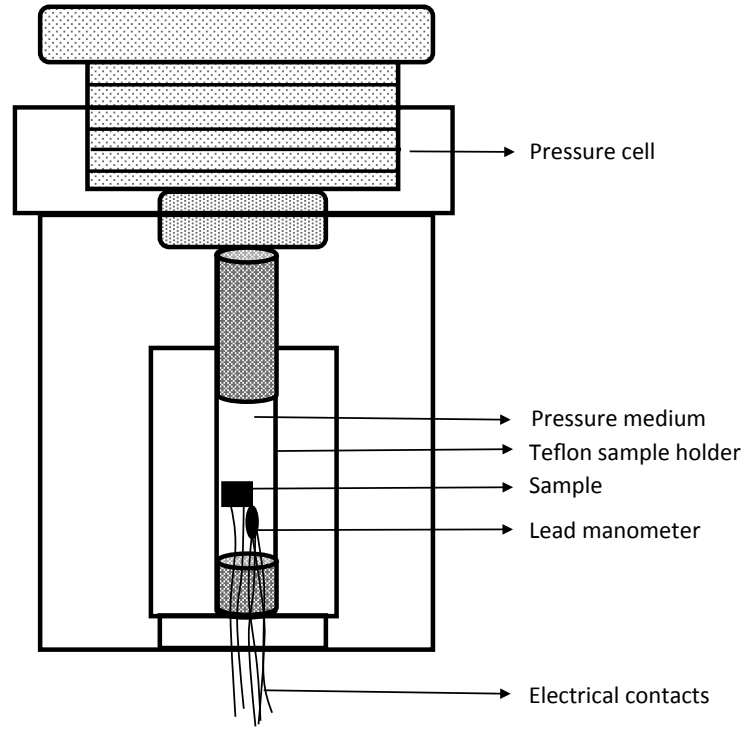


Figure 3.3: The schematic diagram of the pressure cell with sample and lead manometer inside the Teflon sample holder. The Teflon sample holder is filled with the pressure medium FC-77.

ambient pressure. The  $T_C$  of the lead was found to be decreasing with pressure. By knowing the change in  $T_C$ , we can find the actual pressure of the sample environment from the table based on Eq. 3.3 [49],

$$\Delta T_c = -3.689 \times 10^{-2} P + 1.026 \times 10^{-4} P^2. \quad (3.3)$$

### 3.8 Mutual induction measurement under high-pressure

For mutual inductance measurements, a small piece of sample cut from the pellet was prepared by winding with copper wire as explained in the previous section. At first, two layers of 46-gauge copper wire (secondary coil) were wound on the sample and then followed by two additional layers of 44-gauge copper wire (primary coil). Both the sample and the thermocouple go inside the Teflon sample holder where the contact wires were taken out from the Be-Cu cap. The excitation current drives the primary coil and produces the mutual inductance signal in the secondary coil which was measured by 19 Hz LR 700. Ambient pressure measurements were done for all samples before applying pressure. The pressure was applied in the similar way as discussed in section 3.7. As the measurement was performed above LN2 temperature, there is no need of He<sup>4</sup> cryostat. So the pressure cell was attached to the probe and inserted into wide mouth dewar which was filled with LN2. The temperature control was done manually by lowering down and moving up the probe at the rate of 1-3 K/min. Chromel-Alumel thermocouple was used for the temperature measurement. The pressure of the sample was estimated from the calibration curve of the pressure cell. When the magnetic property of the sample changes, the change in mutual inductance of the coil was also observed.

### 3.9 Specific heat measurement

The heat capacity per unit mass of the material at constant pressure is defined as specific heat at constant pressure ( $C_P$ ).

$$C_p = \left(\frac{dQ}{dT}\right)_p \quad (3.4)$$

All the heat capacity measurements were performed in PPMS using heat capacity option and standard heat capacity puck (Fig. 3.4) from Quantum Design [4]. The puck has its own calibration data. The platform of the puck is connected to thermal bath by four pairs of wires. A heater and a temperature sensor are attached at the bottom of the platform. A thin layer of Apiezon N grease was used to provide thermal contact between the sample and the platform. It should be noted that Apiezon H grease should be used instead of N grease for measurements above the room temperature. Before measuring the heat capacity, one must measure the addenda of grease plus sample platform in the desired temperature range. After completing the addenda measurement, a small sample of mass  $< 5$  mg was prepared for the measurement and was placed in the previously affixed N grease making certain that the sample is in good thermal contact with the grease. Depending on the thermal contact of the sample with the platform, the system will use one of two models to fit the data. To provide the best conditions possible, a sample with a flat surface was preferred to guarantee the best possible thermal contact. For a majority of our measurements, the thermal contact was pretty good and simple model (one tau model) was used to fit the data, where the temperature  $T$  of the platform obeys the Eq. 3.5

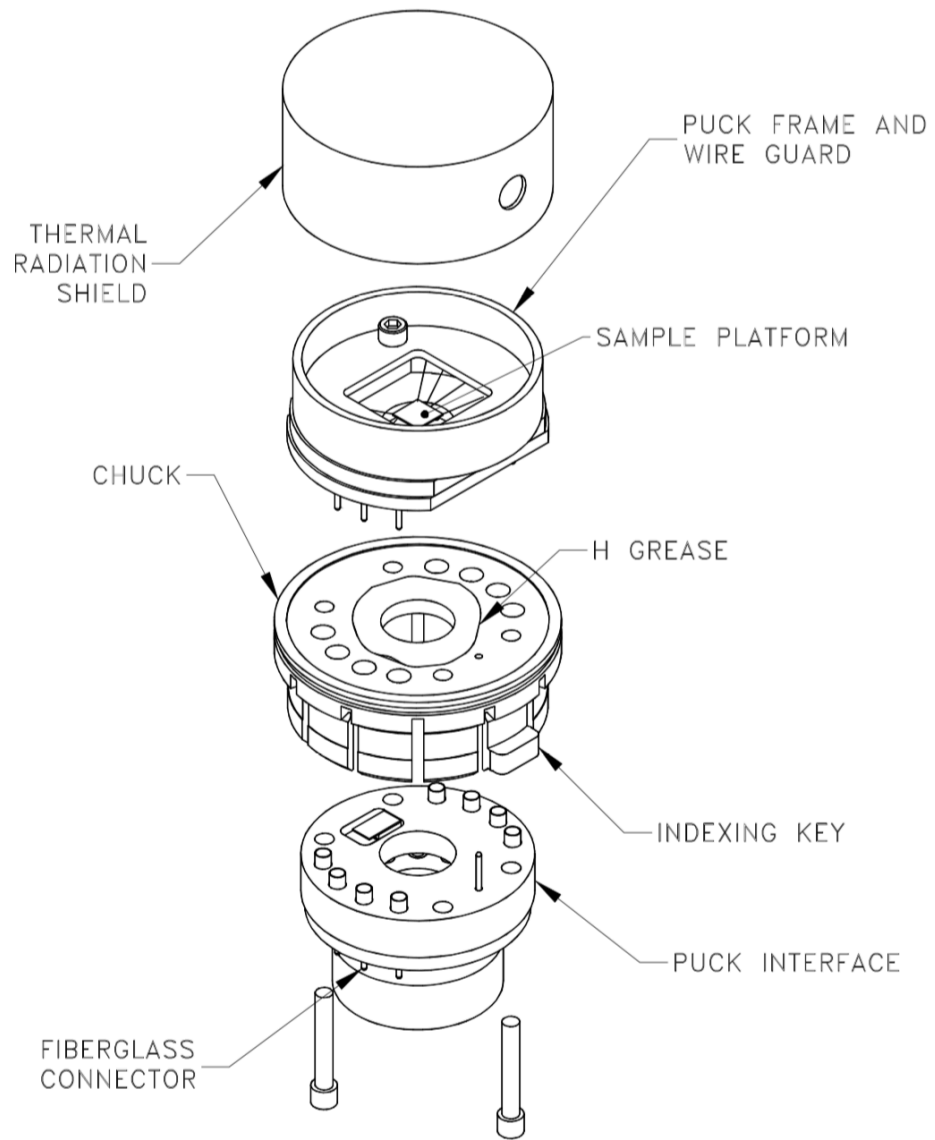


Figure 3.4: Expanded view of Quantum Design heat capacity puck [4]. The diameter of the puck is 20 mm and the height is 15 mm.

as function of time

$$C_{total} \frac{dT}{dt} = -K_w(T - T_b) + P(t). \quad (3.5)$$

Once the measurement is done, the system automatically subtracts the addenda and gives specific heat of the sample in the desired unit. In Eq. 3.5,  $C_{total}$  is the total heat capacity of the sample and sample platform,  $K_w$  is the thermal conductance of the supporting wires,  $T_b$  is the temperature of the thermal bath, and  $P(t)$  is the heater power. The heater power  $P(t)$  is equal to  $P_o$  during the heating portion of the measurement and equal to zero during the cooling portion. The solution of Eq. 3.5 is given by exponential functions with a characteristic time constant  $\tau$  equal to  $C_{total}/K$ .

### 3.10 Dilatometer and thermal expansion measurement

High-precision capacitance dilatometer built from oxygen-free copper was used for thermal expansion measurements which is shown in Fig. 3.5. Any length change experienced by the sample will displace the upper plate of the dilatometer which is secured by two beryllium-copper springs to the lower plate. The upper plate can move farther and closer from the lower plate changing the separation between two capacitor plates. So any change in sample size changes the separation of two plates and thereby changing capacitance. These capacitor plates are polished by 20 nm size diamond grease which increases the sensitivity of capacitance. The capacitor plates

are kept insulating from upper and lower plates by  $75 \mu\text{m}$  thin Kapton films. The diameter of the lower plate is larger than that of upper plate which ensures that the active area of capacitor plates is kept constant ( $A = 78.54 \text{ mm}^2$ ) throughout the motion of upper plate.

The sample whose length change is to be measured was placed in sample stage and secured with the help of adjustable screws. The two sides of sample perpendicular to the direction of measurement was polished and made flat. Prestressing to the sample was applied to make desired fixed separation between two capacitor plates. The room temperature capacitance reading was maintained  $15 \text{ pF} - 20 \text{ pF}$  which corresponds to plate separation of  $70 \mu\text{m} - 46 \mu\text{m}$ . While prestressing, one should be careful that the system should be able to accommodate when the sample expands or contracts during temperature change.

The entire arrangement of dilatometer head shown in Fig. 3.5 was connected to the probe which can be inserted in Janis cryostat having the double reservoir, the outer for LN2 and inner for liquid He<sup>4</sup>. The temperature was controlled by evaporation of He gas and measured by a cernox temperature sensor attached to the copper body of probe head near to the sample. The change in capacitance as a function of temperature was measured by high precision capacitance bridge AH2500A.

The change in length of the sample was calculated from the change in capacitance. However, the calculation is not straightforward. In addition to the sample's length change, the dilatometer also changing its length with temperature variation. In order to correct this, an additional measurement was also done for a reference

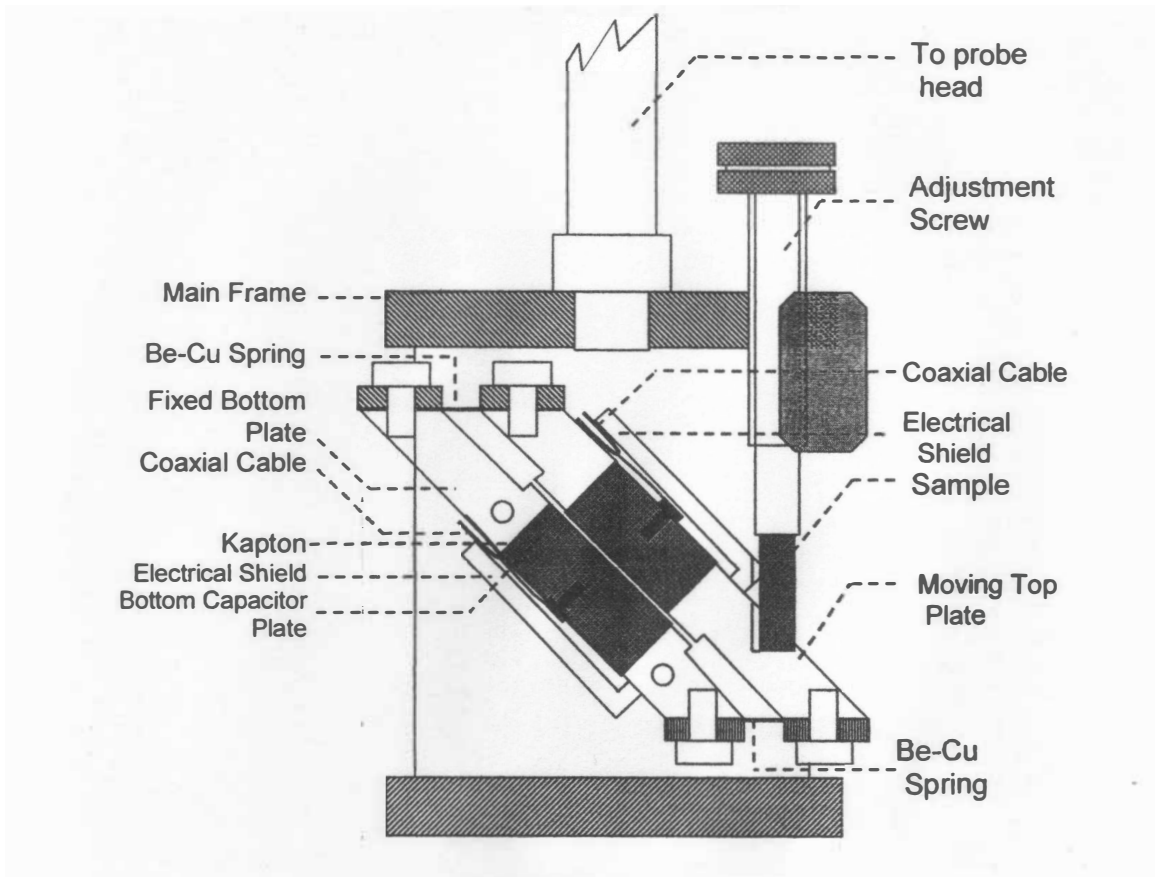


Figure 3.5: The front view of different parts of the high-precision dilatometer.

material (99.999% pure Cu) in the same temperature range used for the sample. The reference material prepared was of the same thickness of the sample and the pre-stressing parameter used for the previous measurement were also for the sample. The capacitance change as a function of temperature was also measured for this reference material. The change in sample length ( $\Delta L_{sample}(T)$ ) is then calculated using Eq. 3.6

$$\begin{aligned}\Delta L_{sample}(T) &= \Delta L_{expt}(T) - \Delta L_{dilat}(T) \\ \Delta L_{sample}(T) &= \Delta L_{expt}(T) - \Delta L_{Cu}^{expt}(T) + \Delta L_{Cu}^{standard}(T)\end{aligned}\quad (3.6)$$

where  $\Delta L_{expt}(T)$  is the total change in length and  $\Delta L_{dilat}(T) = \Delta L_{Cu}^{expt}(T) - \Delta L_{Cu}^{standard}(T)$  is the dilatometer response.

As the plates are  $45^\circ$  counterclockwise from the measurement axis, the relation among the plate separation  $d(T)$ , the length at temperature  $T$ ,  $L(T)$  and the capacitance  $C(T)$  is given by:

$$\Delta L(T) = L(T) - L(T_o) = \sqrt{2}(d(T) - d(T_o)) = \sqrt{2}\epsilon A \left( \frac{1}{C(T)} - \frac{1}{C(T_o)} \right) \quad (3.7)$$

where  $\epsilon$  is the permittivity of air and  $A$  is the area of top plate. The changes are measured with reference to temperature  $T_o$  which can be any arbitrary temperature. The reference temperature in this work was taken 60 K. The thermal expansion along different axes thereby the volume change was measured in cooling and heating cycle.

### 3.11 Neutron diffraction

Neutron diffraction experiments were done at Oak Ridge National Laboratory (ORNL) in collaboration with Dr. Feng Ye. The crystal structures of Ni-doped  $\text{MnWO}_4$  single crystals were examined in detail using a Rigaku X-ray diffractometer equipped with PILATUS 200K hybrid pixel array detector at ORNL. Magnetic neutron diffraction experiments were carried out at the High Flux Isotope Reactor (HFIR) also located at Oak Ridge. Triple axis spectrometer HB-1A was used to study the doping and temperature evolution of the magnetic orders. A neutron beam with a wavelength of  $2.366 \text{ \AA}$  was used and pyrolytic graphite (PG) crystals were used as monochromator and analyzer. The crystals were aligned in several scattering planes to probe the different magnetic reflections. The spin structures were determined using the HB-3A four-circle diffractometer with neutrons of wavelength  $1.536 \text{ \AA}$  at selected temperatures. The structural refinement was performed using the FullProf suite. Magnetic representation analysis was performed to choose appropriate basis vectors to describe the various spin structures. The sample temperature was regulated using a closed cycle refrigerator.

# Chapter 4

## Results

### 4.1 Magnetic field effect in $\text{Mn}_{1-x}\text{Co}_x\text{WO}_4$ ( $x = 0.135, 0.15, 0.17$ )

To explore the magnetic field effect successfully in this compound, it is very important to understand the multiferroic phase diagram of its parent compound  $\text{MnWO}_4$  as well as  $\text{Mn}_{1-x}\text{Co}_x\text{WO}_4$  without magnetic field. So before talking about the magnetic field effect in  $\text{Mn}_{1-x}\text{Co}_x\text{WO}_4$  ( $x = 0.135, 0.15, 0.17$ ), I will discuss some of the multiferroic properties of its parent compound  $\text{MnWO}_4$  and Co doped  $\text{MnWO}_4$ .  $\text{MnWO}_4$  is a naturally occurring mineral known also as Hübnerite and is one of the most studied type II multiferroic over the recent years. It crystallizes in monoclinic structure belonging to space group  $P2_1/c$  and lattice parameters:  $\alpha = \gamma = 90^\circ$  and  $\beta = 91^\circ$ . Several groups began studying the multiferroicity of  $\text{MnWO}_4$  in 2006,

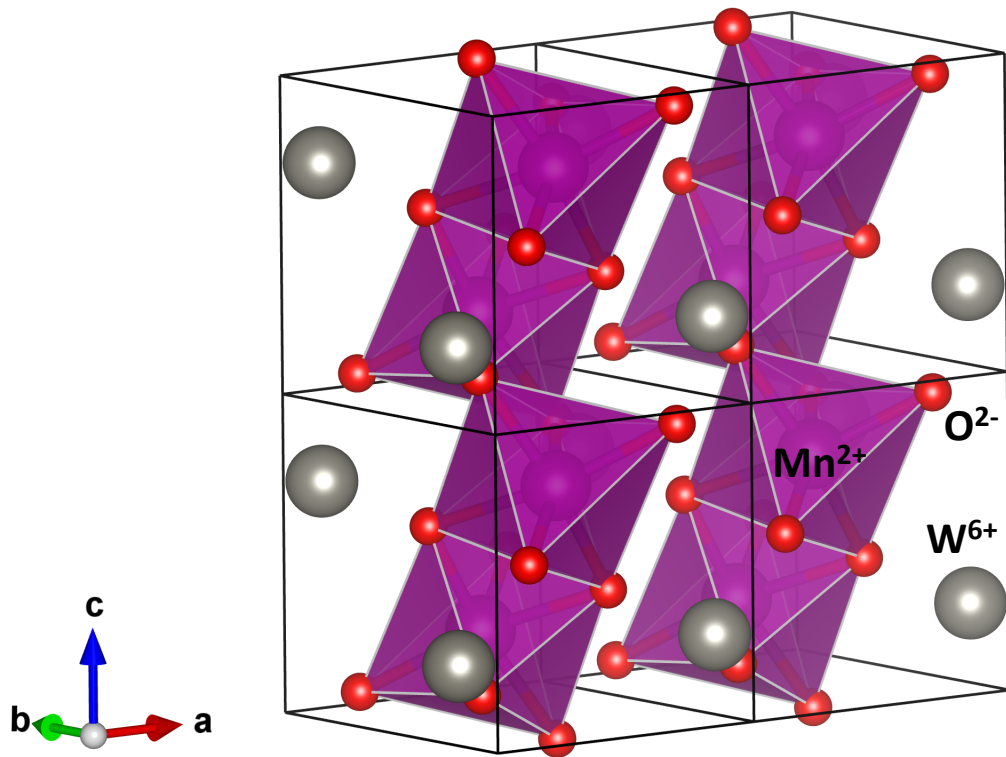


Figure 4.1: Crystal structure of monoclinic  $\text{MnWO}_4$ . The zigzag chains of the Mn ions are surrounded by an oxygen octahedra along the  $c$ -axis and the Mn spins are frustrated along the  $a$ - and  $c$ -directions.

which put this material at the center of interest [30, 50, 51, 52, 53]. However, neutron diffraction studies had already been reported in 1993 by Lautenschlager *et al.* [18] where they studied the various magnetic orders. The  $\text{Mn}^{2+}$  ions (spin  $5/2$ ) are surrounded by spin-lattice octahedra, which form zigzag chains along the  $c$ -axis as shown in Fig. 4.1. Above the Néel temperature ( $T_N = 13.6$  K),  $\text{MnWO}_4$  is paramagnetic and paraelectric; however, due to the highly frustrated nature of the Mn spins along the  $a$ - and  $c$ - directions it shows many exotic antiferromagnetic orders below  $T_N$ . The spin frustration in this material arises due to the significant number of long-range competing exchange interactions that were studied in inelastic neutron scattering experiments by F. Ye *et al.* [6, 7]. Below  $T_N$  the Mn spins order into an incommensurate sinusoidal magnetic order with a modulation vector  $\mathbf{Q}_3 = (-0.214, 0.5, 0.457)$ . In this sinusoidal AF3 phase, the spins are in collinear order which has no ferroelectric polarization. At a slightly lower temperature, 12.6 K, another magnetic phase transition occurs and gives rise to a helical magnetic order of incommensurate AF2 phase with  $\mathbf{Q}_2 = (-0.214, 0.5, 0.457)$  which is same as the  $\mathbf{Q}_3$ . The AF2 phase breaks the inversion symmetry and gives rise to a ferroelectric polarization along the  $b$ -axis ( $P_b$ ) which is consistent with Eq. 2.24. The AF2 phase has both magnetic and ferroelectric order parameters, so it is a multiferroic phase. The multiferroic AF2 phase can not extend up to low temperature as another collinear commensurate AF1 phase  $\mathbf{Q}_1 = (0.25, 0.5, 0.5)$  competes for the ground state below 7.5 K as a result of the magnetic frustration. The AF1 ( $\uparrow\uparrow\downarrow\downarrow$ ) phase is also paraelectric due to its collinear spin structures. So three frustrated magnetic phases are prevalent in  $\text{MnWO}_4$  at different temperatures below  $T_N$ .

Any small perturbation in this material such as chemical doping, magnetic field, or pressure can drastically change the multiferroic properties due to change in exchange interactions and magnetic anisotropy. For example, the substitution of non-magnetic ions such as Zn or Mg suppresses the AF1 phase and stabilize AF2 phase [54, 55] whereas the substitution of the magnetic ions Fe up to 5% quickly suppresses the multiferroic AF2 phase and stabilizes the paraelectric AF3 and AF1 phases [56, 57, 58]. External magnetic fields cause a flop of the polarization towards the  $a$ -axis whereas pressure suppresses the AF2 phase and stabilizes the low-temperature paraelectric AF1 phase [30, 52].

A rich phase diagram of multiferroic and magnetic phases is obtained from Co doping on Mn sites in  $\text{MnWO}_4$  which is shown in Fig. 4.2(a) [5, 6]. The spin-easy-axis of Co in  $\text{CoWO}_4$  is  $-46^\circ$  with  $a$ -axis in  $a - c$  plane [59]. In this way, the spin-easy-axis of Co spins is almost perpendicular to the easy-axis of Mn spins in  $a - c$  plane. The strong anisotropy of Co spins rotates the helical plane of Mn spins in  $\text{MnWO}_4$  towards its hard-axis as shown in Fig. 4.3, affecting the gain in energy in multiferroic phase. The change in polarization is not unusual if the orientation of helical plane changes. Co doping of as low as 2% suppresses the collinear AF1 phase ( $\uparrow\uparrow\downarrow\downarrow$ ) and stabilize helical AF2 phase  $\mathbf{Q}_2 = (Q_x, 0.5, Q_z)$  up to 7.5% Co doping as a ground state multiferroic phase. This AF2 phase is the incommensurate helical structure where the plane of the spin helix makes an angle of  $36^\circ$  with  $a$ -axis at  $x = 0$ . The AF2 phase gives  $b$ -axis polarization and can be explained by the spin current model as  $\mathbf{P} \propto \mathbf{e}_{ij} \times (\mathbf{S}_i \times \mathbf{S}_j)$ . Above 7.5%, the spin helix rotates and confines in the  $a - c$  plane generating incommensurate AF5 phase

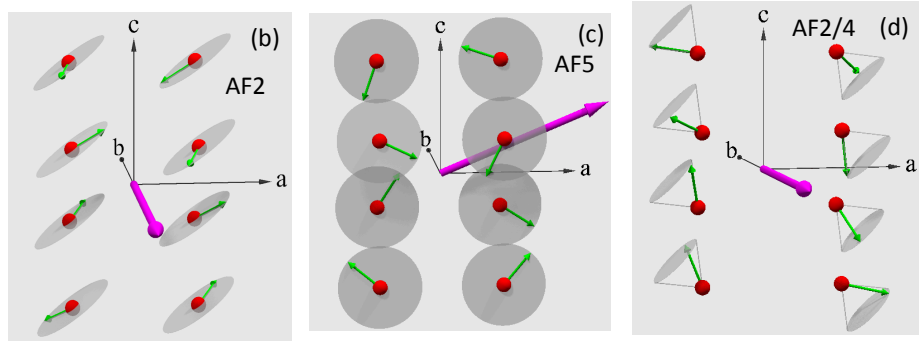
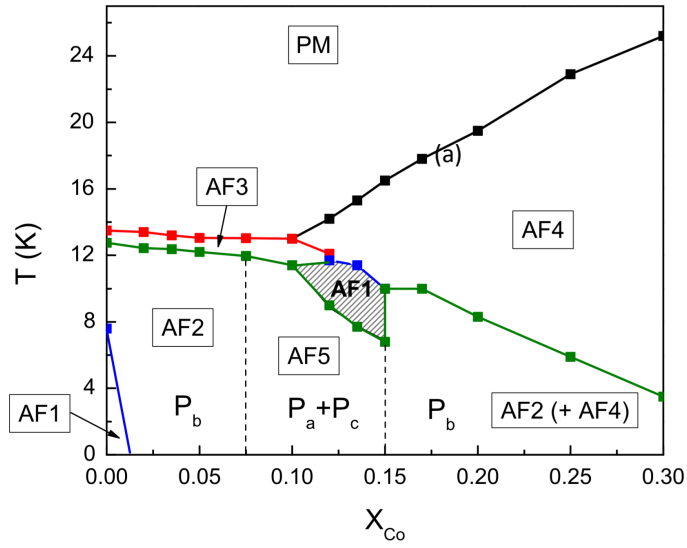


Figure 4.2: (a) Phase diagram of  $\text{Co}$  doped  $\text{MnWO}_4$  without magnetic field [5]. (b), (c) and (d) show the spin helix in different multiferroic phases of  $\text{Mn}_{1-x}\text{Co}_x\text{WO}_4$ . The large arrows indicate the direction of polarization in respective multiferroic phases.

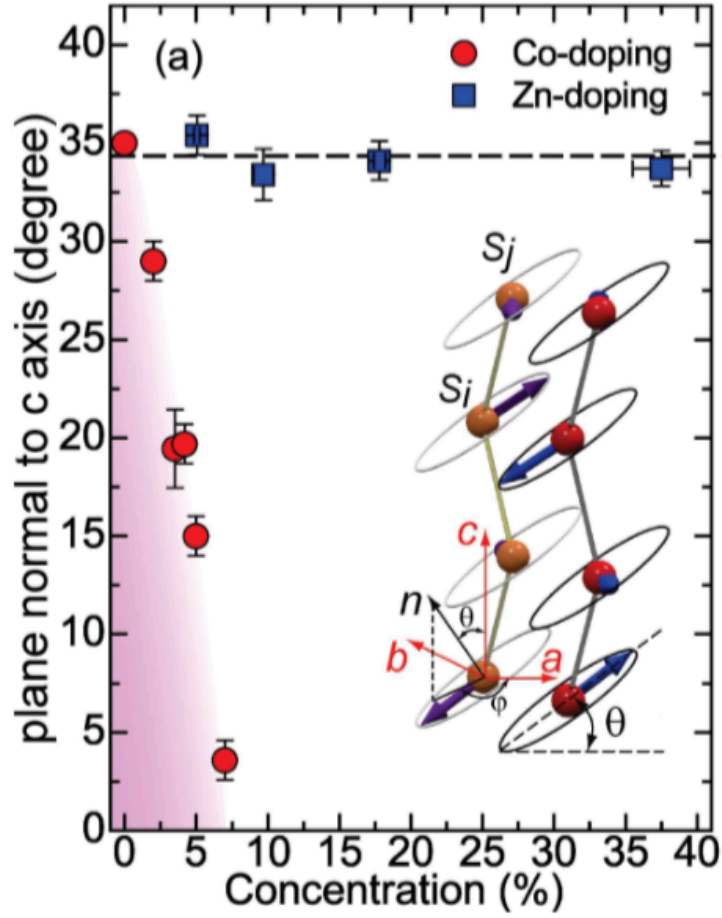


Figure 4.3: The dependence of angle  $\Theta$  with Co and Zn concentration in  $\text{Mn}_{1-x}\text{Co}_x\text{WO}_4$  and  $\text{Mn}_{1-x}\text{Zn}_x\text{WO}_4$ . The angle  $\Theta$  in AF2 phase decreases with increased Co concentration. Above 7.5% Co doping,  $\Theta$  vanishes and the helical plane flips into  $a - c$  plane (not shown in the figure). The image is taken from [6] with permission.

$\mathbf{Q}_5 = (Q_x, 0.5, Q_z)$  which gives the polarization along the  $a$ - and  $c$ - direction. The rotation of the spin helix can be explained by the change in the spin helix angle with  $a$ -axis. The AF5 phase survives up to 15% Co doping. A new conical phase arises above 15% and extends up to 30% Co doping. This conical phase can be explained from two modulation vectors of incommensurate AF2 phase  $\mathbf{Q}_2 = (Q_x, 0.5, Q_z)$  and commensurate AF4 phase  $\mathbf{Q}_4 = (0.5, 0, 0)$ , so called AF2/4 phase. The AF2/4 phase is a multiferroic phase and allows  $b$ -axis polarization. However, at high temperature collinear paraelectric AF4 phase evolves. Above 30% Co doping, the conical phase is completely disappeared and high-temperature collinear AF4 phase becomes ground state magnetic phase in  $\text{Mn}_{1-x}\text{Co}_x\text{WO}_4$ . Spin orientations of different ground state multiferroic phases are shown in Fig. 4.2 (b), (c) and (d). The collinear AF3 phase is existing in the same temperature range as in  $\text{MnWO}_4$  up to 12% Co doping.

$\text{Mn}_{0.85}\text{Co}_{0.15}\text{WO}_4$  is right at the boundary of two complex ground-state multiferroic phases, AF5 phase and AF2/4 phase. It contains five magnetic phases in the different temperature range where two low-temperature multiferroic phases (AF5 and AF2/4) are coexisting. Both phases are verified from neutron diffraction. So we focused on this complex multiferroic material and applied the magnetic field along  $c$ - and  $a$ -axis and found an unusual result. To explain the unusual result, we did the magnetic field study of both magnetic phases AF5 and AF2/4 separately in 13.5% and 17% Co doped  $\text{MnWO}_4$ . In the following sections, first I will discuss the effect of magnetic field separately in multiferroic AF5 and AF2/4 phases and discuss the case of these two coexisting multiferroic phases.

### 4.1.1 Magnetic field induced spin-flop transition in



A frustrated antiferromagnetic system can be easily distracted by an external magnetic field in different ways. The effects of the magnetic field depend on the strength and direction of the field, anisotropy of magnetic ions and nature of frustration. In a frustrated antiferromagnetic system, the magnetization suddenly changes at  $T_N$  due to magnetic domain formation. A sharp drop in magnetization is observed below  $T_N$  due to the decrease in longitudinal component of the magnetic moment if the field is parallel to spins whereas it remains almost unchanged with temperature if the field is perpendicular to the spin orientations.  $\text{Mn}_{1-x}\text{Co}_x\text{WO}_4$  is a highly frustrated system which goes through many magnetic phase changes below  $T_N$  and forms helical structure at low temperature. When the external magnetic field is parallel with the helical plane, the conical spin structure is formed with a change in  $M(T)$  below  $T_N$ . The longitudinal components of the spins tend to flop and becomes almost perpendicular to the field if the applied field is above the critical field. The similar behavior is observed in  $\text{Mn}_{0.865}\text{Co}_{0.135}\text{WO}_4$  and  $\text{Mn}_{0.85}\text{Co}_{0.15}\text{WO}_4$  when the magnetic field is applied along the  $c$ -axis.

The magnetic measurements  $M(T)$  for  $x = 0.135$  along all three crystallographic axes are shown in Fig. 4.4. At zero field, the magnetic system passes through three magnetic transitions below  $T_N$  [6]. A commensurate order of collinear AF4 phase sets below  $T_N = 15.5$  K, which is indicated by the slope change in  $M(T)$ . At slightly lower temperature (11.7 K), another slope change indicates the origin of collinear

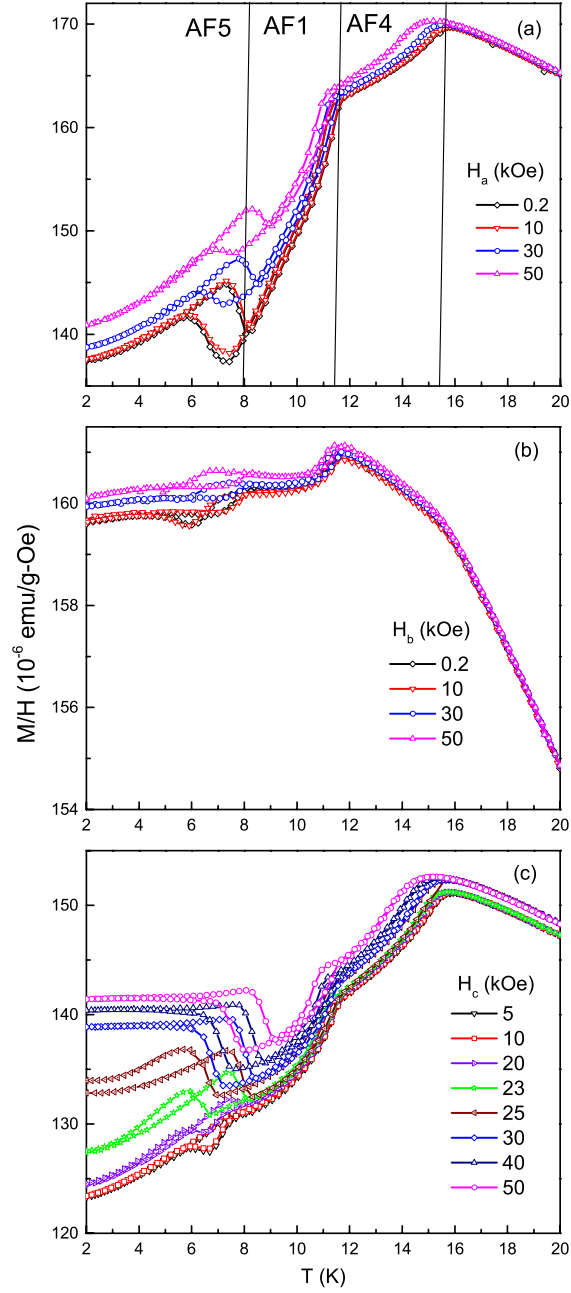


Figure 4.4: Magnetic measurement  $M(T)$  of  $\text{Mn}_{0.865}\text{Co}_{0.135}\text{WO}_4$  in the magnetic field along different directions. The sharp increase of  $M(T)$  in the  $c$ -axis magnetic field above 25 kOe indicates the spin-flop transition in AF5 helical phase.

AF1 phase which exists down to 7 K and is consistent with the phase diagram shown in Fig. 4.2. Below 7 K, the incommensurate AF5 phase becomes the ground state with the helical plane in the  $a - c$  plane. In this in-plane helical structure, the spin-flop transition is expected above the critical field where  $c$ -axis field gives  $a - b$  spiral and  $a$ -axis field gives  $b - c$  spiral. The  $a$ -axis magnetic field up to 50 kOe doesn't show any spin-flop in the AF5 phase, which is consistent with the previous report that shows the magnetic field of more than 6 T is required for spin-flop in  $\text{Mn}_{0.9}\text{Co}_{0.1}\text{WO}_4$  [60]. However, a sharp jump in  $M(T)$  is observed below 7 K in the  $c$ -axis magnetic field above 23 kOe and remains constant at the lower temperature (Fig. 4.5). This type of phase transition is related to spin-flop transition where the  $a - c$  spiral in the AF5 phase now flips into  $a - b$  spiral in the conical form similar to the sketch shown in Fig. 4.11(b).

The effect of spin-flop transition is clearly reflected in the ferroelectric polarization shown in Fig. 4.5(a). The helical AF5 phase has no  $P_b$  in zero magnetic field, however, it allows polarization along  $a$ - and  $c$ - direction [5]. The  $c$ -axis magnetic field above 20 kOe induced  $P_b$  in AF5 phase at  $T_C = 8$  K which remains constant at low temperature. The  $P_b$  increases with increased magnetic field and the  $T_C$  moved to 9 K at the magnetic field of 70 kOe. The increase of  $T_C$  with the field is in agreement with  $M(T)$  data shown in Fig. 4.4. The stabilization of the  $P_b$  in  $c$ -axis field and its saturation at low temperature can be considered as the consequence of the spin-flop transition in the magnetic field. The  $a - b$  spiral (spin helix) formed after the spin-flop transition is a conical structure with its axis along the  $c$ -axis. It is called high field AF5 phase and allows the  $P_b$ . Similar type of spin-flop transition

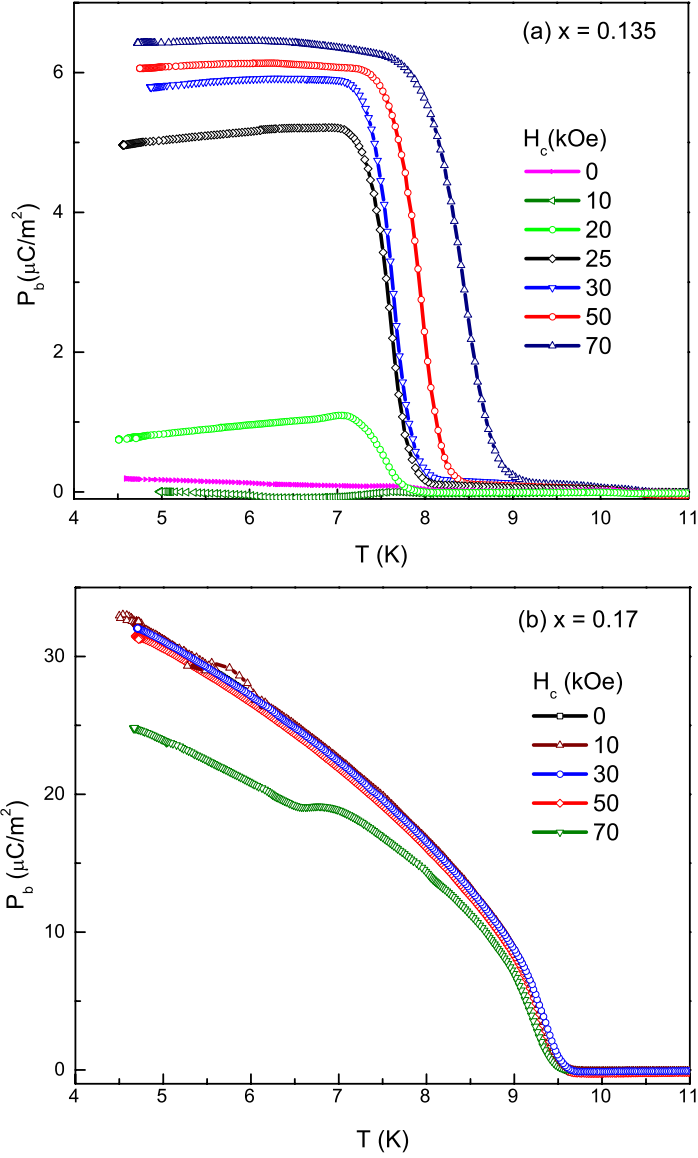


Figure 4.5: Magnetic field dependence of  $P_b$  in  $\text{Mn}_{1-x}\text{Co}_x\text{WO}_4$ . (a) For  $x = 0.135$ ,  $P_b$  appears suddenly above 20 kOe in the AF5 phase and remains constant at low temperature. The  $T_C$  increases with the magnetic field and reaches to 9 K at 70 kOe. (b) For  $x = 0.17$ ,  $P_b$  is unaffected by the  $c$ -axis magnetic field up to 50 kOe. A small drop in  $P_b$  is observed at low temperature above 50 kOe.

into AF2/4 phase is also observed for  $x = 0.135$  under hydrostatic pressure above 15 kbars from neutron diffraction and polarization measurements [61, 62]. The different contributions which give rise to  $P_b$  in high field AF5 phase will be discussed later.

#### 4.1.2 Magnetic field effect in $\text{Mn}_{0.83}\text{Co}_{0.17}\text{WO}_4$

The magnetic field effect for  $x = 0.17$  shown is completely different than the magnetic field effect for  $x = 0.13$ . For  $x = 0.17$ , the magnetic ground state is the conical AF2/4 phase and the high-temperature phase is the collinear AF4 phase. The AF2/4 phase is ferroelectric whereas AF4 phase is paraelectric. The change in  $T_N$  of AF4 phase and  $T_C$  of AF2/4 phase with Co concentration is shown in Fig. 4.2. The onset temperature of AF2/4 phase decreases with increasing Co concentration above  $x = 0.15$ . The AF2/4 phase has conical spin structure (Fig. 4.11(d)) consisting of two modulation vectors  $\mathbf{Q}_2 = (0.5, 0, 0)$  and  $\mathbf{Q}_4 = (0.22, 0.5, -0.44)$  [6]. In our magnetic measurement, a sharp drop in  $M(T)$  is observed at  $T_N = 18$  K with field along  $a-$  and  $c-$  direction which is shown in Fig.4.6. This is due to the reduction of longitudinal component of spins in the AF4 phase. The slope of  $M(T)$  changes at  $T_C = 10.2$  K as the AF2/4 phase evolves but still decreases with temperature. The  $b-$ axis response to  $M(T)$  is different than  $a-$  and  $c-$  axis measurements. Below  $T_N$ ,  $M(T)$  still increases as the field is perpendicular to  $a - c$  plane where the spins are in  $a - c$  plane. Below  $T_C$ , the  $M(T)$  decreases since the AF2/4 phase has longitudinal components along all three axes. So the  $M(T)$  decreases with temperature in AF2/4 phase in all directions. The AF2/4 phase which exists between  $x = 0.15$  to  $x = 0.3$  is the most stable phase in the magnetic field up to 50 kOe.

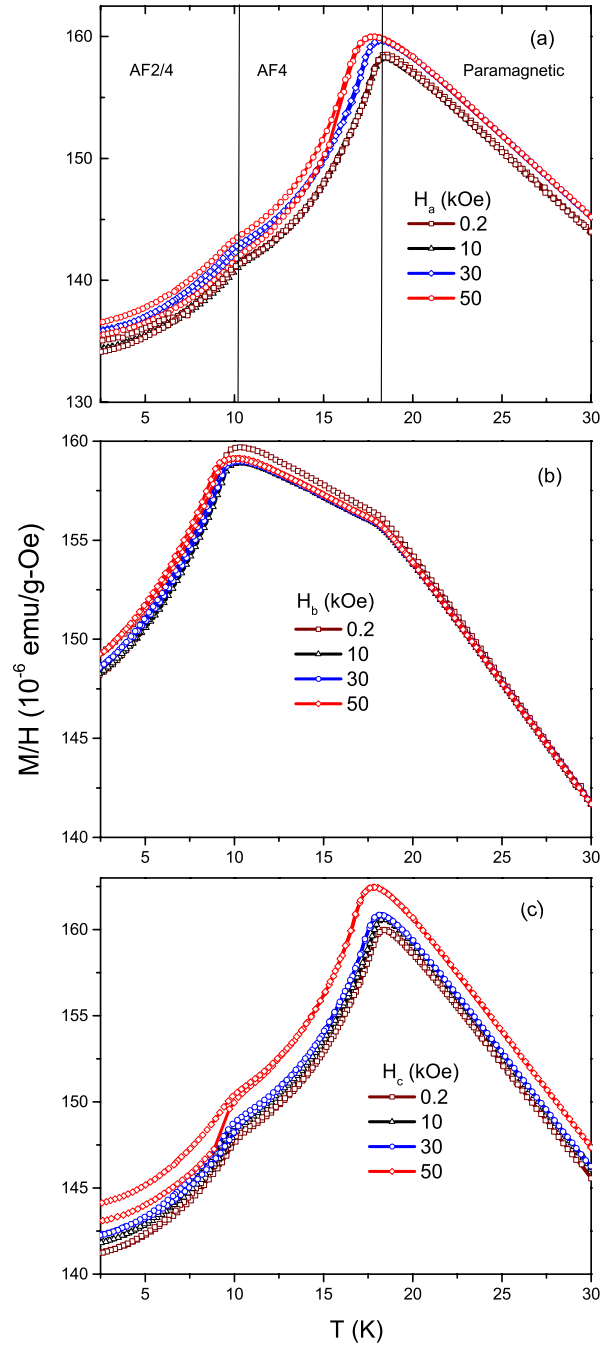


Figure 4.6: Magnetic measurement  $M(T)$  for  $\text{Mn}_{0.83}\text{Co}_{0.17}\text{WO}_4$  along different directions.  $M(T)$  along the  $b$ -axis is different than other directions due to transverse magnetic field with spin orientation in the AF4 phase.

The FE polarization in the AF2/4 phase is almost unaffected by the  $c$ -axis magnetic field up to 70 kOe. The zero field  $P_b$  starts  $\sim 10$  K and increases continuously at low temperature. At 5 K, it reaches the maximum value of  $32 \mu\text{C}/\text{m}^2$ . The magnitude of polarization and  $T_C$  remains unchanged up to the magnetic field of 50 kOe. A small decrease of  $P_b$  to  $25 \mu\text{C}/\text{m}^2$  and the ferroelectric  $T_C$  by 0.1 K is observed at 70 kOe. No ferroelectric polarization was observed in other directions up to field of 70 kOe. This also signifies that AF2/4 phase is the most stable ferroelectric phase of  $\text{Mn}_{1-x}\text{Co}_x\text{WO}_4$  in the magnetic field up to 70 kOe.

### 4.1.3 Polarization reversal by magnetic field in

#### $\text{Mn}_{0.85}\text{Co}_{0.15}\text{WO}_4$

$\text{Mn}_{0.85}\text{Co}_{0.15}\text{WO}_4$  lies right at the boundary of two ground state multiferroic phases, AF5 phase and AF2/4 phase, which is shown in phase diagram shown in Fig. 4.2. The study of multiferroic properties of this material without magnetic field was previously reported [63, 6]. During cooling, it enters into collinear AF4 phase at  $T_N = 17$  K. Below 10.2 K, multiferroic AF2/4 phase arises and coexists with collinear AF1 phase in narrow temperature region between 6.5 K and 10.2 K. The  $P_b$  appears at  $T_{C1} = 10.2$  K as peak due to AF2/4 phase and continues to grow towards low temperature which is shown in Fig. 4.7. The small magnitude of  $P_b$  reflects the small volume fraction of AF2/4 phase coexisting with the collinear AF1 phase at high temperature and with the helical AF5 phase at low temperature. This

high-temperature AF1 phase is existing in the of region  $0.12 < x < 0.15$  which is paraelectric phase [6]. Below 6.5 K, AF5 phase coexists with AF2/4 phase and the system becomes more complex as both are multiferroic phases with different multiferroic properties. Neutron diffraction study of this material shows the coexistence of AF2/4 phase with AF1 and AF5 phases in different temperature range [6].

The  $c$ -axis magnetic field in this material has unusual effect in  $P_b$ . At low magnetic field ( $< 20$  kOe), no significant effect in  $P_b$  arises. However, above 20 kOe,  $P_b$  makes a sharp step-like transition at  $T_{C2} = 7$  K which is shown in Fig. 4.7. This temperature exactly corresponds to the onset of AF5 phase in the phase diagram. With increased magnetic field, the step becomes more prominent and the polarization changes sign above 25 kOe although the applied poling voltage is positive. This effect is very unusual in multiferroic materials. The  $T_{C2}$  increases with the magnetic field while  $T_{C1}$  slightly decreases. Thus, we observed magnetic field induced polarization reversal in  $\text{Mn}_{0.85}\text{Co}_{0.15}\text{WO}_4$  in positive poling voltage. The  $M(T)$  data for  $x = 0.15$  in the magnetic field up to 50 kOe is shown in Fig. 4.8. The magnetization decreases below  $T_N$  and passes through different magnetic phase transitions. These data are similar to the spin-flop transition seen in  $\text{Mn}_{0.865}\text{Co}_{0.135}\text{WO}_4$ . At this point, it can be suggested that the AF5 phase is also contributing to  $P_b$  due to spin-flop transition in the AF5 helical phase similar to  $\text{Mn}_{0.865}\text{Co}_{0.135}\text{WO}_4$ . The critical magnetic field and the nature of transition at  $T_{C2}$  are also consistent with the spin-flop transition in  $\text{Mn}_{0.85}\text{Co}_{0.15}\text{WO}_4$ . So the polarization is possibly arising from the spin-flop transition in AF5 phase in addition to coexisting AF2/4 phase but it is still unknown why the polarization is negative in positive poling field. In order to unveil this unusual effect,

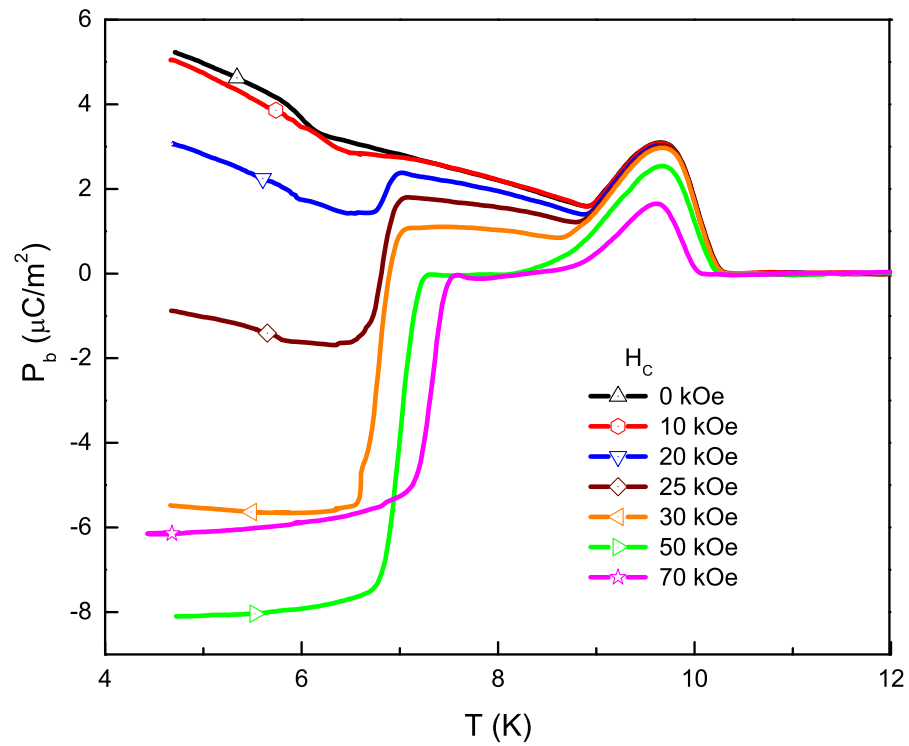


Figure 4.7: Polarization reversal in  $\text{Mn}_{0.85}\text{Co}_{0.15}\text{WO}_4$  in the  $c$ -axis magnetic field. The  $P_b$  becomes negative below  $T_{C2}$  above 25 kOe.  $T_{C2}$  increases with the magnetic field while  $T_{C1}$  slightly decreases above 50 kOe.

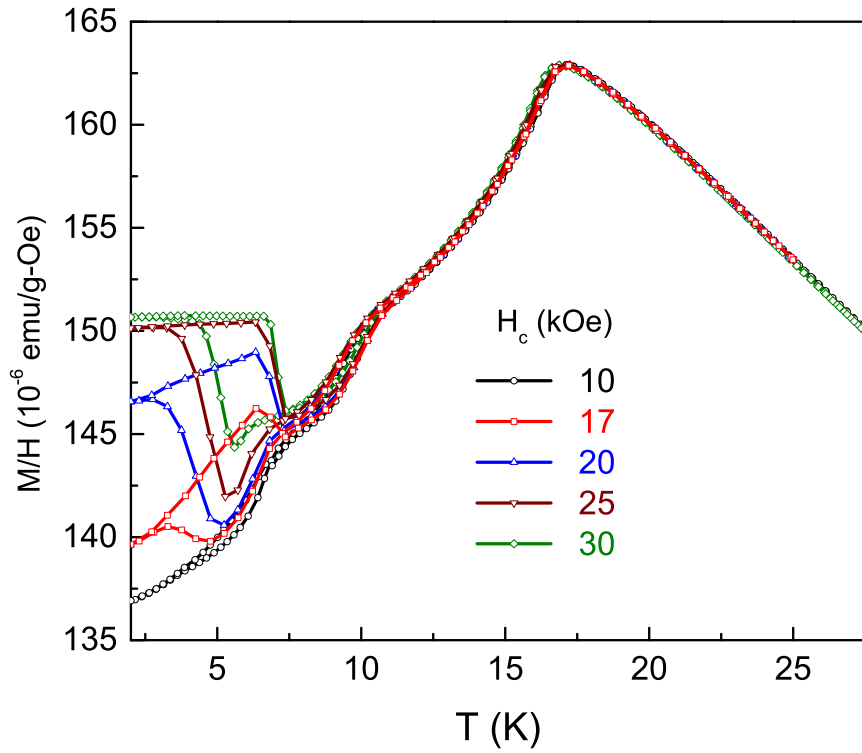


Figure 4.8: Magnetic measurements  $M(T)$  of  $\text{Mn}_{0.85}\text{Co}_{0.15}\text{WO}_4$  in the  $c$ -axis magnetic field.  $M(T)$  decreases below  $T_N$  and suddenly increases due to the spin-flop transition in AF5 phase at 7 K above 20 kOe.  $M(T)$  remains constant at low temperature after the spin-flop transition.

different contributions to  $P_b$  in high field AF5 and AF2/4 phases needs to be discussed in more detail.

The reason of polarization reversal could be related to the coexistence of magnetic phases and magnetic field effect on these phases which triggered us for more detailed investigation of the origin of polarization in this material. However, exploring microscopic origin of all magnetic phases and their contribution to macroscopic polarization is not a trivial task in the frustrated system. The AF5 phase in  $\text{Mn}_{1-x}\text{Co}_x\text{WO}_4$  has polarization in  $a - c$  plane and is maximum between  $x = 0.075$  and  $0.10$ , which decreases quickly above  $x > 0.1$ , whereas the conical AF2/4 phase which exists above  $x = 0.15$  allows only  $P_b$  [5]. The magnetic field effect in multiferroicity of these two separate phases is totally different as discussed previously for  $x = 0.135$  (pure AF5 phase) and for  $x = 0.17$  (pure AF2/4 phase).

The magnetic frustration in  $\text{Mn}_{1-x}\text{Co}_x\text{WO}_4$  is similar to the frustration in  $\text{MnWO}_4$ . In both cases frustration arises from competing exchange interactions of Mn spins along  $a-$  and  $c-$  axis. The magnetic phases in  $\text{MnWO}_4$  are stabilized by many long-range competing exchange interactions. This can be evidenced from the spin wave excitations in  $\text{MnWO}_4$  obtained from inelastic neutron scattering. The spin wave excitation shows best fitting to Heisenberg model with single ion anisotropy when 11 pairs of exchange interactions from  $J_1$  to  $J_{11}$  are considered [7]. The exchange energy values  $J$ 's vary from 0.02 eV to 0.43 eV in magnitude. The strength of polarization arising from those spin interactions depends on how strongly the spin pairs are interacting with each other. In order to make the complex problem simple from those 11 pairs, we consider only those pairs which have exchange energy up

to 50% of the maximum. With this limitation, the relevant exchange pathways of interactions ( $J1$ ,  $J3$ ,  $J4$ ,  $J6$ ,  $J9$ ) are shown in Fig. 4.9.

In  $\text{Mn}_{1-x}\text{Co}_x\text{WO}_4$ , only the spiral and conical phases contribute to ferroelectric polarization. So it is necessary to evaluate which spin pairs contribute significantly to polarization in these phases according to spin current model. In the spin current model, the polarization is proportional to the vector product of two spins ( $\mathbf{S}_i \times \mathbf{S}_j$ ) which consists the angle between two spin directions. As the incommensurate modulation ( $Q_x, Q_z$ ) is known for different phases, the angle between spin pairs can be estimated easily. Only two spin pairs interacting through  $J1$  and  $J3$  exchange pathways shown in Fig. 4.9 contribute significantly in this model. The angle between spin pairs of these pathways is nearly perpendicular which makes the cross product maximum. For other pairs  $J4$ ,  $J6$  and  $J9$ , the spins are almost parallel or antiparallel vanishing the cross product. The  $J1$  pathways correspond to the intrachain exchange interaction along the  $c$ -axis whereas  $J3$  corresponds to the interchain exchange interaction along  $a$ -axis and both interactions contribute to total ferroelectric polarization separately.

The contribution to FE polarization by different exchange pairs can be calculated mathematically using the spin current model where  $\mathbf{P} \propto \mathbf{e}_{ij} \times (\mathbf{S}_i \times \mathbf{S}_j)$ . If  $\mathbf{P}^{J1}$  and  $\mathbf{P}^{J3}$  are the polarizations due to  $J1$  and  $J3$  exchange pathways and  $m_{\parallel}$ ,  $m_{\perp}$  are the long and short axes of the spin helix, then using the geometry shown in Fig. 4.10, we derived the expression for polarization as

$$\mathbf{P}^{(J1)} = C^{(J1)} m_{\parallel} m_{\perp} \sin(\pi Q_z) [-\sin\Theta \sin\varphi \mathbf{e}_x + \sin\Theta \cos\varphi \mathbf{e}_y] \quad (4.1)$$

and

$$\mathbf{P}^{(J3)} = C^{(J3)} m_{\parallel} m_{\perp} \sin(2\pi Q_x) [-\cos\Theta \mathbf{e}_y + \sin\Theta \sin\varphi \mathbf{e}_z] \quad (4.2)$$

The equations we derived are dependent in unit normal vector  $\mathbf{n} = \sin\Theta \cos\varphi \mathbf{e}_x + \sin\Theta \sin\varphi \mathbf{e}_y + \cos\Theta \mathbf{e}_z$  of the helical plane where  $\Theta$  is the angle between normal  $\mathbf{n}$  and z-axis,  $\varphi$  is the angle made by the projection of  $\mathbf{n}$  in the x-y plane with the x-axis. The a, b and c axes correspond to x, y and z-axes respectively.  $C^{(J1)}$  and  $C^{(J3)}$  are constants whose values depend on various factors, for example, interactions along  $J1$  and  $J3$  exchange pathways.  $\Theta$  and  $\varphi$  vary for different magnetic phases. For AF5 phase in Fig. 4.2(c),  $\Theta = 90^\circ$ ,  $\varphi = 90^\circ$  and both exchange pathways  $J1$  and  $J3$  contribute to the polarization.  $J1$  and  $J3$  contributions give rise to  $P_a$  and  $P_c$  respectively. However, in high field AF5 phase,  $\Theta = 0^\circ$  and only gives  $P_b$  via  $J3$  exchange pathways. For AF2/4 phase,  $\varphi = 0^\circ$  gives only  $P_b$  from both exchange pathways  $J1$  and  $J3$ .

The total  $b$ -axis polarization  $P_b$  can be extracted from Eq. 4.1 and Eq. 4.2. With Eq. 4.3 we can explain the polarization reversal in  $\text{Mn}_{0.85}\text{Co}_{0.15}\text{WO}_4$  above the critical magnetic field.

$$P_b = m_{\parallel} m_{\perp} [C^{(J1)} \sin(\pi Q_z) \sin\Theta \cos\varphi - C^{(J3)} \sin(2\pi Q_x) \cos\Theta] \quad (4.3)$$

#### 4.1.4 Origin of polarization reversal in $\text{Mn}_{0.85}\text{Co}_{0.15}\text{WO}_4$

The total contribution to  $P_b$  in Eq. 4.3 is derived from the spin current model. In  $\text{Mn}_{0.85}\text{Co}_{0.15}\text{WO}_4$ , two magnetic phases are coexisting and become multiferroic

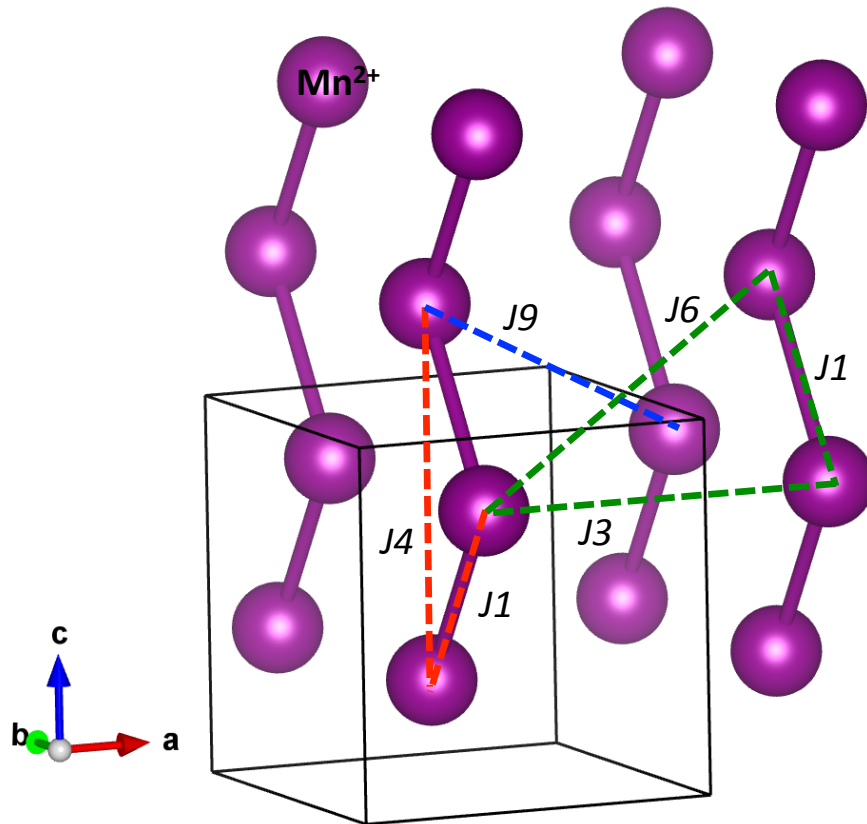


Figure 4.9: Relevant exchange interaction pathways in MnWO<sub>4</sub> based on exchange energy ( $J$ ). The exchange energies of the spin pairs were obtained by fitting spin wave excitation of MnWO<sub>4</sub> with the Heisenberg model [7]. The strength of interaction between spin pairs is proportional to the polarization if allowed by symmetry.

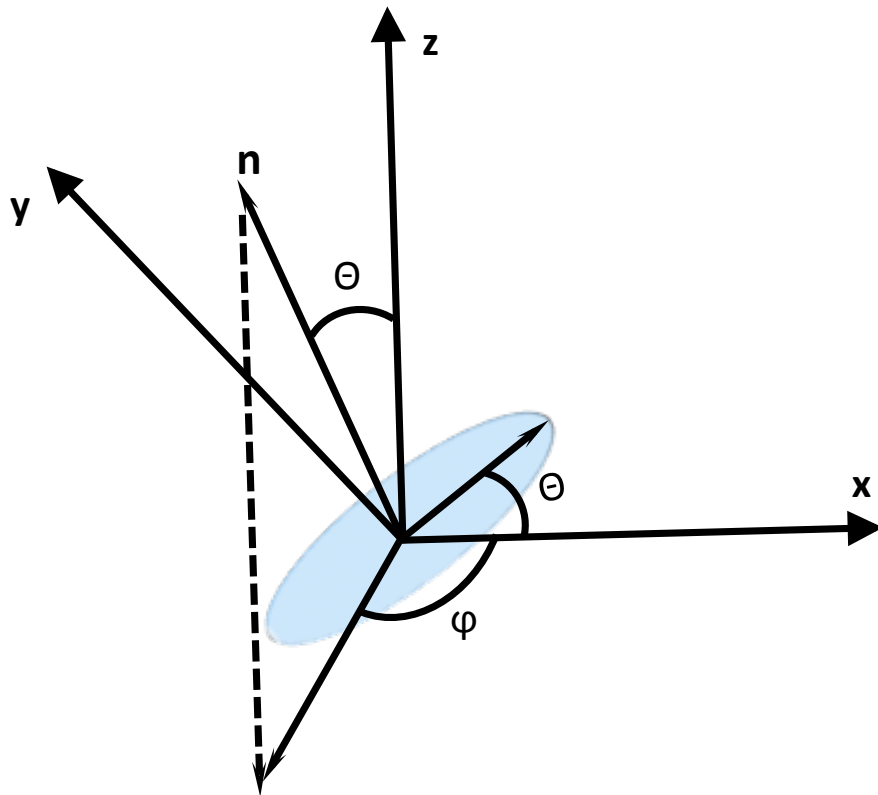


Figure 4.10: The schematic diagram of normal vector  $\mathbf{n}$  to the helical plane, angle  $\Theta$  between the normal  $\mathbf{n}$  and the  $z$ -axis, angle  $\varphi$  made by projection of  $\mathbf{n}$  in the  $x$ - $y$  plane with the  $x$ -axis. The  $x$ ,  $y$  and  $z$ -axes correspond to the  $a$ ,  $b$  and  $c$ -axes of the crystal geometry.

at different temperature with polarization in different directions. The direction of polarization is determined by the chirality of spin helix in the corresponding phase. While cooling the sample in the magnetic field, the electric field determines the chirality of spin helix at ferroelectric transition in such a way that total polarization is positive in the positive electric field. In  $\text{Mn}_{0.85}\text{Co}_{0.15}\text{WO}_4$ , the  $P_b$  at  $T_{C1} = 10.2$  K in  $c$ -axis magnetic field is positive as expected. However,  $P_b$  suddenly changes its sign at  $T_{C2}$  above the critical field, increasing the magnitude of  $P_b$  with the magnetic field. At low temperature and above the critical field, when the spin-flop happens in AF5 phase, the chirality of high field AF5 phase should be same as the chirality of AF2/4 phase to minimize the domain wall energy of two different phases. The chirality of the spin helix is preserved across the domain wall due to strong coupling between the two magnetic domains of different phases. Preserved chirality is favorable in the spiral magnetic system to minimize the domain wall energy. The sketch of smooth transition across the domain wall between two phases is shown in Fig. 4.11. Although the spin-flop transition occurs in AF5 phase above 20 kOe, the AF4/4 phase is stable in the magnetic field up to 70 kOe.

When the sample is cooled below critical magnetic field, only AF2/4 phase contributes to  $P_b$  below  $T_{C1}$ . As discussed in the previous section, both  $J1$  and  $J3$  exchange pathways in Fig. 4.9 contribute to  $P_b$ , but  $P_b^{J1}$  is greater than  $P_b^{J3}$  which gives total  $P_b$  as a positive value. Above the critical field and below  $T_{C2}$ , the helical plane of AF5 phase flops in  $a - b$  plane preserving the chirality of the spin helix as shown in Fig. 4.11(b). The spin helix in  $a - b$  plane now allows  $P_b$  via  $J3$  exchange pathways whereas the contribution to  $P_b$  due to  $J1$  exchange pathways vanishes

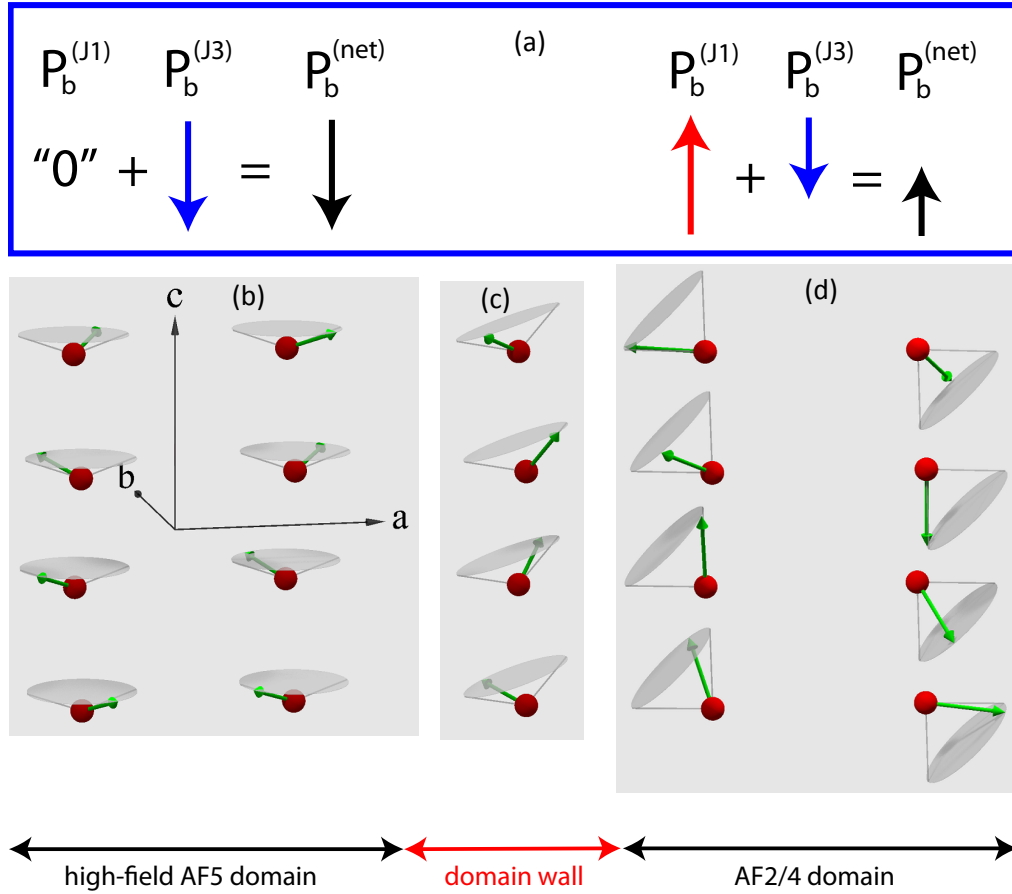


Figure 4.11: The smooth transition across the domain wall of two multiferroic phases [8]. (a) Sketch of total contribution to  $P_b$  by  $J1$  and  $J3$  exchange pathways in the two domains. (b) Domain structure of the AF5 phase after spin-flop transition. (c) Domain wall transition between the AF2/4 phase and AF5 phase in the  $c$ -axis magnetic field. (d) Domain structure of the AF2/4 phase.

( $\Theta = 0^\circ$ ). Only the second term in Eq. 4.3 contributes to  $P_b$  which is negative although the poling electric field is positive. Thus the total  $P_b$  become negative in high field AF5 phase. A schematic sketch of how  $P_b$  becomes negative is shown in Fig. 4.11(a).

The spin-flop transition in  $\text{Mn}_{0.85}\text{Co}_{0.15}\text{WO}_4$  that happens in AF5 phase coexisting with AF2/4 phase similar to spin-flop transition in  $\text{Mn}_{0.865}\text{Co}_{0.135}\text{WO}_4$ . Although the AF5 phase doesn't allow  $P_b$ , the high field AF5 phase gives rise to  $P_b$ . The chirality of the spin helix in high field AF5 phase is preserved during spin-flop transition due to strong coupling of two coexisting magnetic phases. The preserved chirality forces the  $P_b$  to be negative as multiple exchange pathways contribute to polarization differently. If the coupling is not strong enough, the high field AF5 phase can independently determine its chirality at  $T_{C2}$  and the total  $P_b$  would be positive at low temperature.

Our explanation of polarization reversal in  $\text{Mn}_{0.85}\text{Co}_{0.15}\text{WO}_4$  is supported by  $P_b$  measurement of  $\text{Mn}_{0.85}\text{Co}_{0.15}\text{WO}_4$  in  $a$ -axis magnetic field shown in Fig. 4.12 [64]. In  $a$ -axis field, the spin helix in  $a - c$  plane flops to  $b - c$  plane due to spin-flop transition, making spins orientation transverse to the field. In this spin configuration, the spin current vector is parallel to  $a$ -axis and only the  $J1$  exchange pathways contribute to  $P_b$  ( $\Theta = 90^\circ$ ). So only the first term in Eq. 4.3 exists and we expect the total positive polarization if the chirality of the AF2/4 phase and  $b - c$  spiral is preserved. The  $P_b$  measurement in  $\text{Mn}_{0.85}\text{Co}_{0.15}\text{WO}_4$  shown in Fig. 4.12 is in agreement with our expectation. The  $P_b$  increases with  $a$ -axis magnetic field up to 55 kOe with the sharp transition in AF5 phase at  $T_{C2}$ . Above 55 kOe,

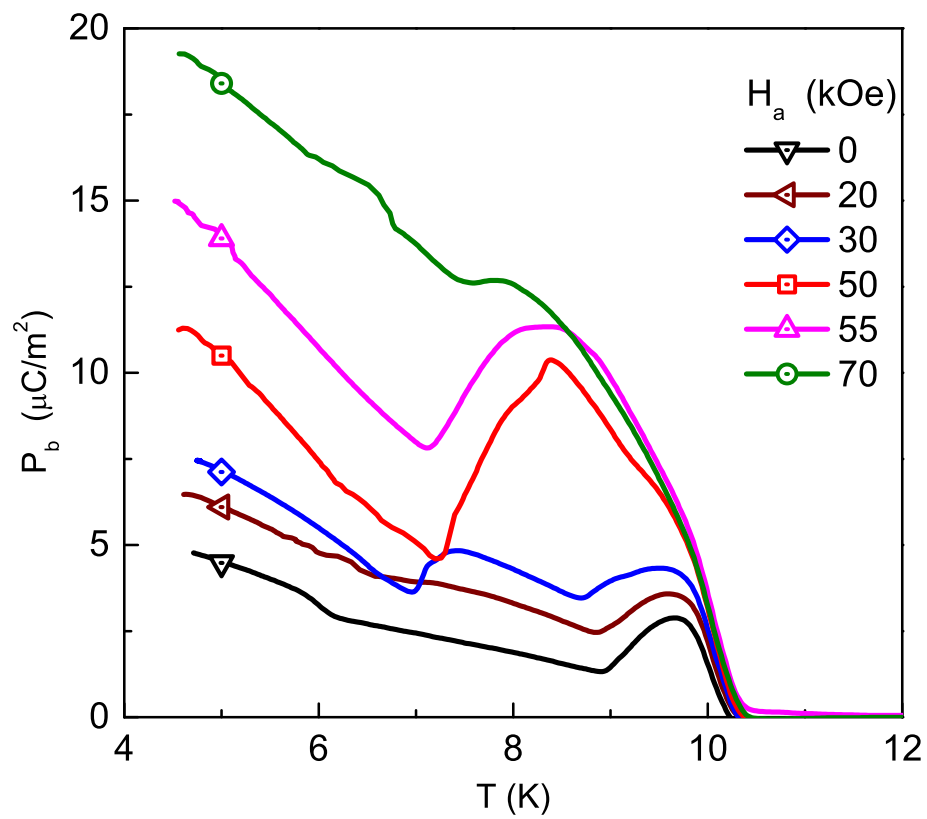


Figure 4.12: Ferroelectric polarization ( $P_b$ ) of  $\text{Mn}_{0.85}\text{Co}_{0.15}\text{WO}_4$  in the  $a$ -axis magnetic field. Unlike in the  $c$ -axis magnetic field, the total  $P_b$  is positive in the  $a$ -axis magnetic field.

$P_b$  suddenly increases at  $T_{C2}$  due to spin-flop transition with total  $P_b$  positive in agreement with Eq. 4.3. The  $a$ -axis critical magnetic field for spin-flop transition is different than  $c$ -axis critical field mentioned previously, however it is in agreement with the  $a$ -axis critical field of spin-flop transition in  $\text{Mn}_{0.9}\text{Co}_{0.1}\text{WO}_4$  reported from neutron scattering [60]. Thus the spin-flop transition and preserved chirality of magnetic domains successfully explain the magnetic field effect in  $\text{Mn}_{0.95}\text{Co}_{0.05}\text{WO}_4$ .

#### 4.1.5 Magnetic field induced polarization rotation in

##### $\text{Mn}_{0.95}\text{Co}_{0.05}\text{WO}_4$

An interesting magnetic field effect is also observed at lower Co doping. The ground state of  $\text{Mn}_{0.95}\text{Co}_{0.05}\text{WO}_4$  is the AF2 phase which by its symmetry gives the  $b$ -axis polarization. The magnetic field applied along  $b$ -axis continuously rotates the  $b$ -axis polarization towards the  $a$ -axis due to the rotation of the AF2 helical plane by  $90^\circ$  [65]. In order to reveal the microscopic mechanism of polarization rotation, the domain wall study in this type II multiferroic material using the Second Harmonic Generation (SHG) imaging and atomistic Landau-Lifshitz-Gilbert (LLG) simulations were performed [9]. The SHG images clearly show the configuration domain wall states changes from side-by-side ( $\uparrow\downarrow$ ) configuration to head-to-head ( $\rightarrow\leftarrow$ ) or tail-to-tail ( $\leftarrow\rightarrow$ ) configuration without changing the position of the domain wall under the magnetic field.

Fig. 4.13(a) shows the bulk measurement of polarization in  $\text{Mn}_{0.95}\text{Co}_{0.05}\text{WO}_4$  along the  $a$ - and  $b$ -axes in the  $b$ -axis magnetic field at 5 K. Only  $P_b$  was observed

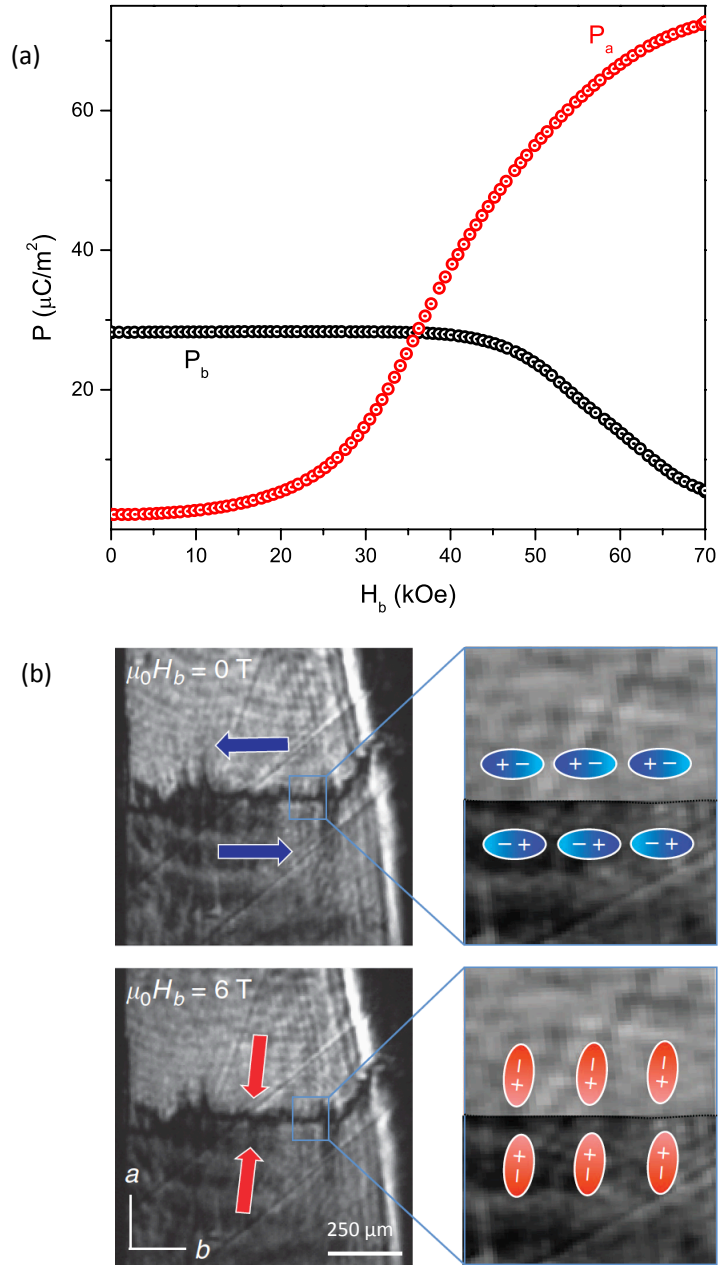


Figure 4.13: (a) Continuous rotation of the polarization direction in  $\text{Mn}_{0.95}\text{Co}_{0.05}\text{WO}_4$  from the  $b$ -axis to  $a$ -axis in the  $b$ -axis magnetic field at 5 K. (b) The SHG image of side-by-side domain wall at 0 T ( $P \parallel b$ ) converting to head-to-head domain wall at 6 T ( $P \parallel a$ ) at 5 K. The SHG images are taken from ref.[9].

in zero magnetic field. When the magnetic field is applied along the  $b$ -axis, the  $P_b$  decreases and at the same time the  $a$ -axis polarization ( $P_a$ ) appears and continues to grow with increased magnetic field. At 70 kOe, the maximum value of  $P_a$  reaches to  $72 \mu\text{C}/\text{m}^2$  whereas  $P_b$  continuously decreases towards zero. This confirms the continuous rotation of polarization in the  $b$ -axis magnetic field. The origin of this type of polarization rotation is indeed different than the spin-flop induced polarization in  $\text{Mn}_{0.865}\text{Co}_{0.135}\text{WO}_4$  discussed in the previous section and the sudden switching of the polarization from the  $b$ -axis to the  $a$ -axis above 10 T in  $\text{MnWO}_4$  [30]. The effect of Co spin anisotropy is the key parameter for the continuous rotation of polarization in the AF2 phase above 30 kOe, as this type of effect was not observed in the AF2 phase of other multiferroics, for example,  $\text{MnWO}_4$ .

The SHG susceptibility and images [9] confirms that the polarization can be controlled at the ferroelectric domain wall by external magnetic field. The presence of Néel component and non-zero polarization at the center of domain wall observed in LLG simulations indicates that charged domain walls are arising from the fluctuation of local distribution of carriers. As shown in the Fig. 4.13(b), the domain wall remains fixed although the polarization is continuously rotating in the magnetic field. This can transform the side-by-side  $\uparrow\downarrow$  domain wall states to head-to-head  $\rightarrow\leftarrow$  or tail-to-tail  $\leftarrow\rightarrow$  states which make the domain walls charged. So it is worthy to look for if the domain wall conductivity is measurable in  $\text{Mn}_{0.865}\text{Co}_{0.135}\text{WO}_4$  with our available techniques. For this, a thin sample of thickness 0.4 mm and area  $34.6 \text{ mm}^2$  was prepared to measure the domain wall conductivity. The sample was prepared in the same way to measure the pyroelectric current and cooled to 6 K

without poling field to create domain walls and then applied the magnetic field of 7 T along the  $b$ -axis. The  $180^\circ$  head-to-head domain wall ( $\uparrow\downarrow$ ) created during cooling is now expected to rotate and orient in the head-to-head ( $\rightarrow\leftarrow$ ) or tail-to-tail ( $\leftarrow\rightarrow$ ) configuration with the magnetic field. We tried to measure the current by sweeping the voltage from 0 - 100 V and 100 - 0 V with steps of 10 V increment/decrement. From this technique, we couldn't see any domain wall current, which is not unusual as the polarization is too small in this material and the expected current is  $\sim O(\text{fA})$  while the resolution of our ammeter is 0.1 pA. The other possible reason might be the domain wall is not penetrating completely along the thickness of the sample so that the conduction is blocked. More sophisticated measurements using conductive atomic force microscope (AFM) and piezo-response force microscope are required to detect the domain wall current in  $\text{Mn}_{0.865}\text{Co}_{0.135}\text{WO}_4$ . The anisotropic domain wall conductance was indeed observed by Meier *et al* in improper ferroelectric  $\text{ErMnO}_3$  [66] using the atomic force microscope and piezo-response force microscope. Although the detectable transport measurement is not successful, a new way of tuning of the ferroelectric polarization by the magnetic field in complex multiferroic domain wall is found.

## 4.2 Effects of Ni doping on the multiferroic properties of $\text{MnWO}_4$

As discussed in the earlier section, the substitution of magnetic and non-magnetic transition metals in the Mn site tunes the multiferroic properties of  $\text{MnWO}_4$ . Doping

compound	MnWO <sub>4</sub>	CuWO <sub>4</sub>	FeWO <sub>4</sub>	CoWO <sub>4</sub>	NiWO <sub>4</sub>
$\theta_a$	35°	40°	27.5°	-46.3°	57.6°

Table 4.1: Magnetocrystalline anisotropy of the transition metal ions in T<sub>2</sub>WO<sub>4</sub> (T = Mn, Cu, Fe, Co, Ni) in  $a - c$  plane.  $\theta_a$  is the anisotropy angle with respect to the  $a$ -axis in the  $a - c$  plane. These values are referenced from [18, 19].

of transition metal Zn, up to 50% and Mg up to 30% retains the multiferroicity even though it is nonmagnetic [54, 55], while Fe doping of as low as 5% suppresses the polarization quickly [57, 56, 67]. Similarly, Cu doping up to 10% was also studied by Liang *et al.* which shows the mixture of collinear AF1 and helical AF2 phases at low temperature [68].

The most complex phase diagram is found in Co doping with the multitude of complex multiferroic and magnetic phases [6, 5]. In MnWO<sub>4</sub>, the helical plane includes the easy-axis of Mn spins. When it is doped with Co, the strong anisotropy of Co spins is able to rotate the helical plane of MnWO<sub>4</sub> towards its direction (Fig. 4.3) generating multiple ground state multiferroic phases as a function of Co concentration which is shown in Fig. 4.2 in section 4.1. Table 4.1 shows the direction of easy-axis of magnetization  $\theta_a$  for various T<sub>2</sub>WO<sub>4</sub> (T = Mn, Cu, Fe, Co, Ni) in the  $a - c$  plane in collinear phase. The easy-axis of Mn and Co spins are almost perpendicular to each other in  $a - c$  plane, which means the easy-axis of magnetization for Mn ions becomes the hard-axis of magnetization for Co ions. So the helical plane prefers the direction of the spin-easy-axis of magnetic ions if the magnetic anisotropy is strong enough.

In case of Ni, the easy-axis of Ni spins in NiWO<sub>4</sub> make an angle  $\theta_a = 57.6^\circ$  with

the  $a$ -axis in the  $a - c$  plane which is higher than anisotropy of Mn spins ( $35^\circ$ ) in  $\text{MnWO}_4$  [59, 19, 18]. If Ni doping acts in the similar way as in Co doping, then it could pull the helical plane towards its easy-axis. It is expected that the angle  $\Theta$  made by the helical plane with  $a$ -axis increases and thus enhances the  $P_b$  in Ni doped  $\text{MnWO}_4$  as the polarization is proportional to  $\Theta$ . However, our results showed that Ni doping as low as 5% reduces the polarization and completely suppresses the multiferroicity in  $\text{Mn}_{1-x}\text{Co}_x\text{WO}_4$  above 20% Ni doping. Magnetic and heat capacity measurements also show the suppression of multiferroic AF2 phase with increased Ni concentration. The reduction of the polarization is explained by the anti-correlation effect of Mn and Ni spins, where Ni spin pushes the helical plane further away from the helical plane of  $\text{MnWO}_4$  towards the  $a - b$  plane.

#### 4.2.1 Magnetic properties of $\text{Mn}_{1-x}\text{Ni}_x\text{WO}_4$

The magnetization measured along the monoclinic  $b$ -axis is shown in Fig. 4.14 for Ni concentrations up to  $x = 0.3$ . The three transitions observed in the undoped  $\text{MnWO}_4$  are reflected in clear anomalies of  $b$ -axis magnetization  $M(T)$ . A change of slope at a maximum of  $M(T)$  indicates the onset of sinusoidal magnetic order at  $T_N$ . At slightly lower temperature,  $T_C$ , another slope change is followed by a distinct decrease of  $M(T)$ . At lock-in transition  $T_L$ , a sharp increase of  $M(T)$  indicates the onset of commensurate AF1 phase. The decrease of  $M(T)$  below  $T_N$  is due to decrease in longitudinal component of helical AF2 phase along the field direction. The magnetization is nearly constant with temperature in the sinusoidal AF3 phase and  $\uparrow\uparrow\downarrow\downarrow$  AF1 phase below  $T_L$  as the magnetic field is transverse with

the magnetic moment.

Upon Ni substitution of 5%, the low-temperature AF1 phase is completely suppressed and the multiferroic AF2 phase is stabilized at low temperature. The similar effect was also observed in  $\text{MnWO}_4$  with doping of transition metals Co and Zn [55, 69, 5]. The  $T_N$  and  $T_C$  are not clearly marked from the magnetic susceptibility in 5% Ni doping shown in Fig. 4.14, although they are distinct in heat capacity measurement shown in Fig. 4.15.

Above  $x = 0.1$ , a collinear AF4 phase arises at high temperature which was first seen in heat capacity data for  $x = 0.1$  as a shoulder (Fig. 4.15) and in neutron diffraction data for  $x=0.15$  shown in Fig. 4.17(b). So the critical Ni content to the onset of AF4 magnetic phase is  $x_c = 0.1$ . Below  $x_c$ , both incommensurate phases, the sinusoidal AF3 and the cycloidal AF2, are present and well distinguished through sharp peaks of  $C_P(T)$ . Above  $x_c$ , the incommensurate AF2 phase becomes unstable and moves towards lower temperature. The  $T_C$  decreases with increased Ni content and reaches 5 K for  $x = 0.3$ . On the other hand, the critical temperature of onset of collinear AF4 phase increases with Ni content and reaches to 32 K for  $x = 0.3$ . Above  $x_c$ , the decrease of magnetization below  $T_C$  is less dramatic with increased Ni concentration and shows almost no decrease for  $x = 0.3$ . This behavior indicates the decrease in longitudinal component of the magnetic moment along the field direction. The rotation of the spin helix towards  $a - b$  plane reduces the  $b$ -axis component of the magnetization.

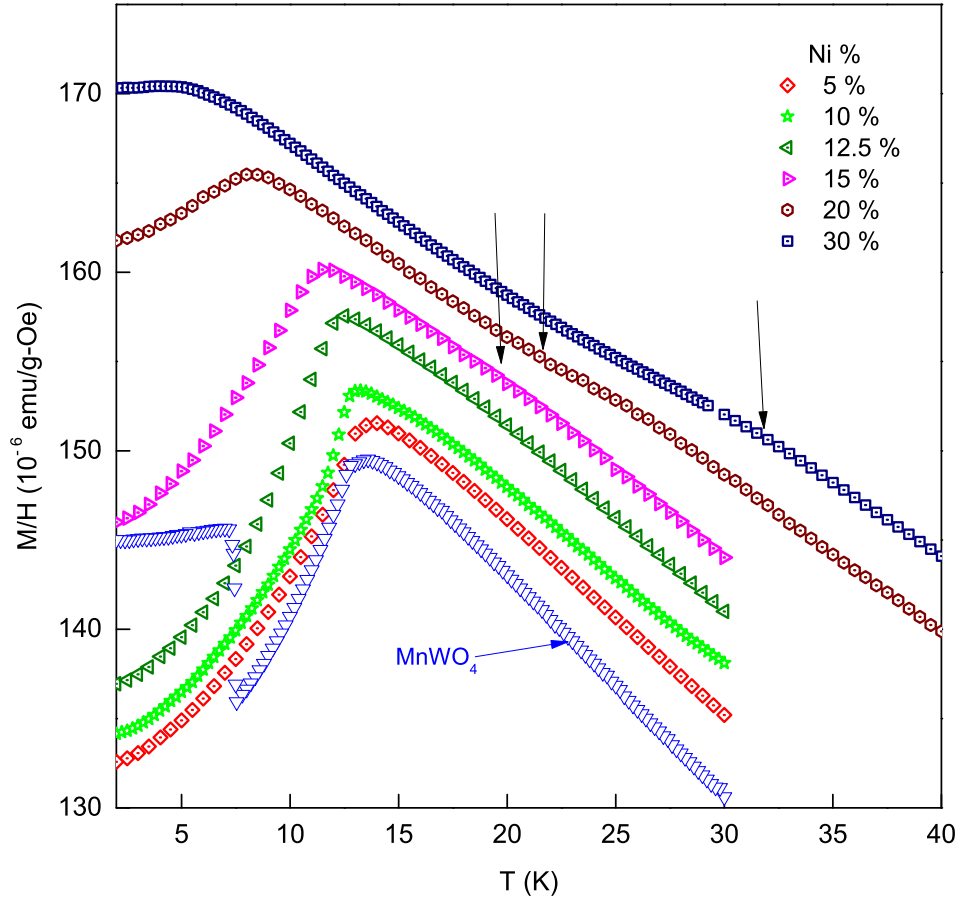


Figure 4.14: DC susceptibility ( $M/H$ ) of  $Mn_{1-x}Ni_xWO_4$  along the  $b$ -axis. The shifting of peaks towards low temperature indicates that the onset temperature of the AF2 phase moves to the lower value with increased Ni concentration. The vertical arrows indicate the onset of AF4 phases for different Ni concentration. The  $M/H$  data are vertically offset for better visualization.

### 4.2.2 Heat-capacity measurement of $\text{Mn}_{1-x}\text{Ni}_x\text{WO}_4$

The heat-capacity  $C_P(T)$  measurements of  $\text{Mn}_{1-x}\text{Ni}_x\text{WO}_4$  shown in Fig. 4.15 clearly reflects the two sharp peaks at the transitions into the sinusoidal AF3 and helical AF2 phases for  $x = 0.05$  similar as in  $\text{MnWO}_4$  (shown in the inset of Fig. 4.15). The two peaks are separated by 1 K where both the  $T_C$  and  $T_N$  are increased by 0.5 K than in  $\text{MnWO}_4$ . The low-temperature peak seen at 7.6 K in  $\text{MnWO}_4$  is completely removed which indicates the suppression of collinear AF1 phase by Ni doping as low as 5%. For 10% Ni doping, the peaks of the AF3 and AF2 phases merged and become one slightly broadened peak. A small shoulder-like anomaly appeared on the higher-temperature side which could be the signal for developing AF4 phase. With increased Ni content, the  $T_C$  of AF2 phase moves to lower temperature whereas the anomaly of AF4 phase becomes pronounced and moves to the higher temperature and this is consistent with the subtle anomaly seen in the magnetic susceptibility. The origin and development of the AF4 phase are indeed observed in our neutron diffraction data above 15% Ni content. Above 30% Ni, only the AF4 survives and multiferroicity is lifted in this material. The collinear AF4 phase is also the ground state and only the magnetic phase of  $\text{NiWO}_4$  below  $T_N = 67$  K [19]. The phase diagram in Fig.4.19 is derived from both magnetic and heat capacity data.

### 4.2.3 Neutron diffraction study of $\text{Mn}_{1-x}\text{Ni}_x\text{WO}_4$

The neutron diffraction of  $\text{Mn}_{1-x}\text{Ni}_x\text{WO}_4$  was done to explore the magnetic structure and explain the multiferroic properties combining with the magnetization or

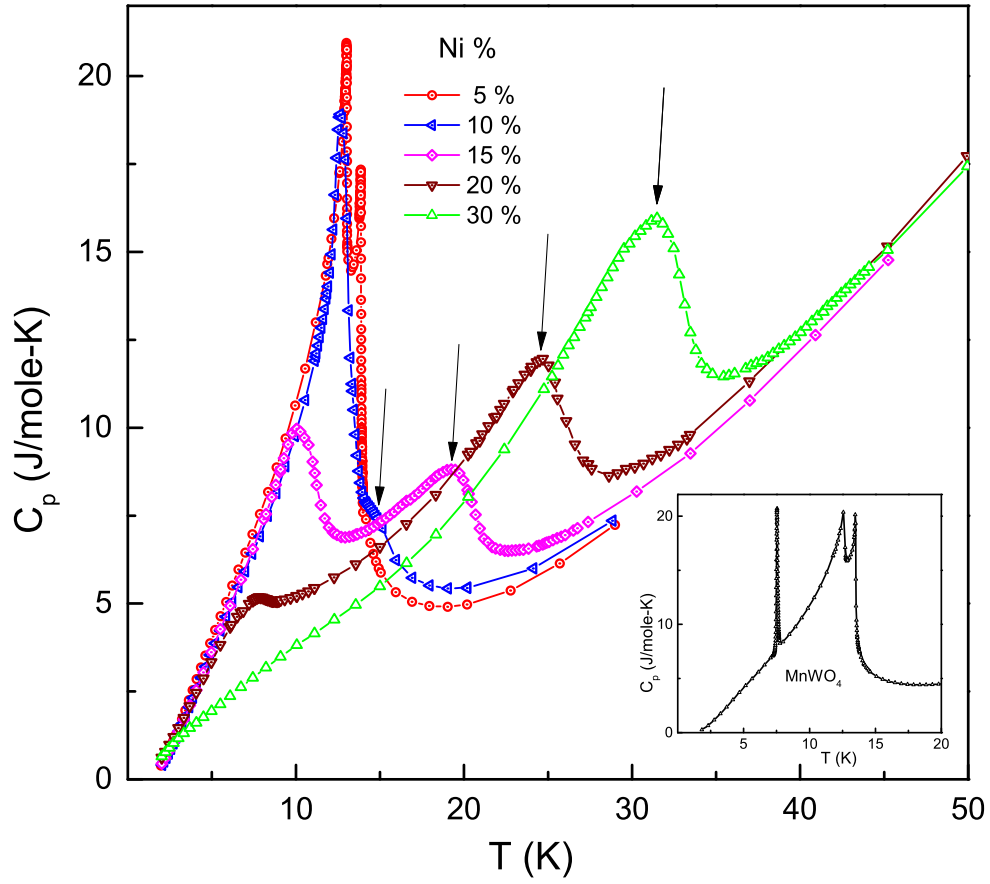


Figure 4.15: Heat capacity  $C_P(T)$  of  $Mn_{1-x}Ni_xWO_4$ . All the magnetic phase transitions are clearly reflected in the heat capacity data. The vertical arrows indicate the onset of AF4 phases for different Ni concentration. The inset shows the heat capacity of pure  $MnWO_4$  which shows additional phase transition into AF1 phase at 7.6 K.

heat capacity data. The details of the magnetic orders in different phases have to be determined by microscopic probes such as neutron scattering to explain the origin of ferroelectricity. Fig. 4.16 shows the results of a systematic study of the magnetic reflections for  $x = 0.05, 0.1$  and  $0.2$  [10]. For low Ni doping,  $x = 0.05$ , the magnetic modulation of the AF2 phase is  $\mathbf{Q}_2 = (0.23, 0.5, 0.46)$  and for  $x = 0.1$ ,  $\mathbf{Q}_2 = (0.235, 0.5, 0.47)$  [10]. At higher Ni doping,  $x = 0.2$ , a new commensurate magnetic phase AF4 with  $\mathbf{Q}_4 = (0.5, 0, 0)$  appears at 28 K, coexisting with the incommensurate AF2 phase below 9 K.

Fig. 4.17 shows the temperature dependence of the magnetic reflections of  $\text{Mn}_{1-x}\text{Ni}_x\text{WO}_4$  corresponding to the incommensurate AF2 phase and the collinear AF4 phases for various Ni concentrations. At  $x = 0.05$ , the collinear AF3 phase sets in below 14 K, followed by the non-collinear AF2 phase at 13 K which persists at the lowest temperature. It is difficult to separate AF3 phase from AF2 phase in the image as the AF3 phase exist in narrow temperature range  $\sim 1$  K and the modulation vector of AF3 and AF2 phase are identical. With increased Ni doping, the transition temperature to the AF2 phase gradually decreases, at the same time the integrated intensities of the associated reflections decrease, indicating the suppression of this non-collinear phase for  $x > 0.05$ . For  $x = 0.15$ , the commensurate AF4 phase with  $\mathbf{Q}_4 = (0.5, 0, 0)$  appears around 20 K, while the integrated intensities of this phase shownon-collinear a drop at lower temperature  $\sim 10$  K. At the same temperature, the intensity of AF2 phase rises and extends to low temperature. This shows the coexistence of both AF2 and AF4 phases below 9 K. Similar phenomenon is observed for  $x = 0.2$  with slightly different onset temperature. At  $x = 0.3$ , only the

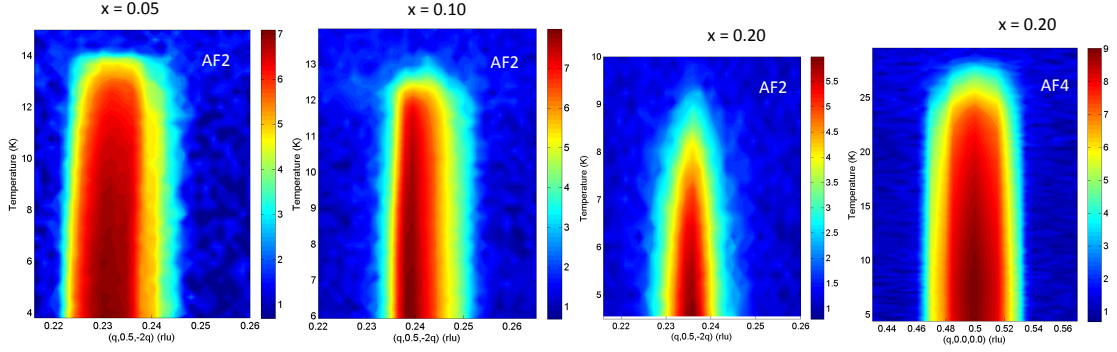


Figure 4.16: Temperature dependence of the wave vector scan of AF2 and AF4 phases for  $\text{Mn}_{1-x}\text{Ni}_x\text{WO}_4$ . The AF4 and AF2 phases are coexisting for  $x = 0.2$  below 9 K. The colors of the images represent the intensities of magnetic reflections in corresponding phases.

collinear AF4 phase is observed which develops at 35 K and survives to the lowest temperature which is in agreement with magnetic and heat capacity measurement.

The low-temperature ( $T = 5$  K, 10 K) refined parameters of AF2 and AF4 phases at different doping levels are summarized in Table 4.2. The AF2 phase for  $x = 0.05$  and 0.10 is characterized by an elliptical helical phase with ellipse principle axes lying along the crystallographic  $b$ -axis and in the  $a - c$  plane. The tilt angle  $\Theta$  of the magnetic component  $m_{\perp b}$  that lies in the  $a - c$  plane makes  $28.1^\circ$  to the crystallographic  $a$ -axis. This is less by  $7^\circ$  than in pure  $\text{MnWO}_4$ . With increased Ni doping at  $x = 0.15$ ,  $m_{\perp b}$  rotates quickly towards the  $a$ -axis. The refinement of the commensurate AF4 phase for  $x = 0.15$  shows that the collinear spin configuration has a moment similar to the pure  $\text{NiWO}_4$ , which is  $\sim 58^\circ$  from the  $a$ -axis [19]. This direction of the moment is different from that of Co-doped  $\text{MnWO}_4$  in the AF4 phase, which is about  $-53^\circ$  from the  $a$ -axis [5]. For  $x = 0.15$ , the principal axis of

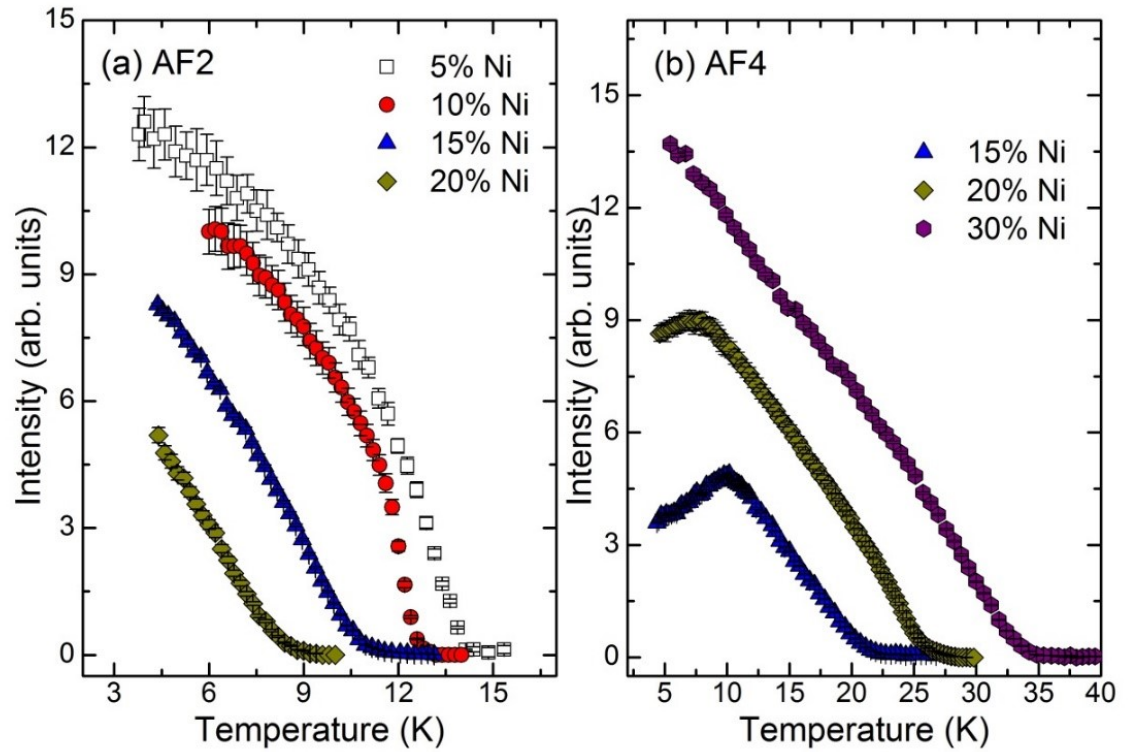


Figure 4.17: (a) Integrated intensities of magnetic reflections of AF2 phase [10]. (b) Integrated intensities of the magnetic reflections of AF4 phase. The intensity and  $T_C$  of the AF2 phase decrease with increased Ni content while the intensity and  $T_N$  of the AF4 phase increase with increased Ni content. For  $x = 0.15$  and  $0.2$ , the two phases are coexisting at low temperature.

x	Magnetic phase	$\Theta^\circ$	Magnetic moment ( $\mu_b$ )	
0.05	AF2 (5 K)	28.1	$m_b = 3.37$	$m_{\perp b} = 4.10$
	AF2 (10 K)	27.4	$m_b = 3.35$	$m_{\perp b} = 3.22$
0.10	AF2 (5 K)	32.2	$m_b = 3.32$	$m_{\perp b} = 3.70$
	AF2 (10 K)	32.6	$m_b = 2.31$	$m_{\perp b} = 2.86$
0.15	AF2 (5 K)	10.0	$m_b = 3.22$	$m_{\perp b} = 2.98$
	AF2 (10 K)	-3.0	$m_b = 1.78$	$m_{\perp b} = 1.03$
	AF4 (5 K)	67.7	$m_a = 0.75$	$m_c = 1.83$
	AF4 (10 K)	71.9	$m_a = 01.25$	$m_c = 2.39$
0.30	AF4 (5 K)	67.5	$m_a = 3.35$	$m_c = 3.01$

Table 4.2: Refined magnetic structure parameters of  $\text{Mn}_{1-x}\text{Ni}_x\text{WO}_4$  for  $x = 0.05, 0.10, 0.15, 0.30$  at 5 K and 10 K.  $\Theta$  is the angle made by  $m_{\perp b}$  with  $a$ -axis.

helical plane that lies in the  $a - c$  plane,  $m_{\perp b}$ , initially makes negative angle ( $-3^\circ$ ) with the  $a$ -axis at 10 K, but changes to a positive angle ( $10^\circ$ ) at 5 K. This change of the orientation of the spin helix causes the observed polarization to be maximum and slightly negative at the lowest temperature.

#### 4.2.4 Ferroelectric properties of $\text{Mn}_{1-x}\text{Ni}_x\text{WO}_4$

As shown in Fig. 4.18, the maximum  $P_b$  for  $x = 0.05$  is  $40 \mu\text{C}/\text{m}^2$  at 5 K which is already smaller than the extrapolated value of  $P_b$  in pure  $\text{MnWO}_4$  ( $60 \mu\text{C}/\text{m}^2$ ). However, the  $T_C$  is increased by 0.5 K and  $P_b$  extends to the lowest temperature. A similar increase in  $T_C$  was also observed in  $\text{Mn}_{1-x}\text{Cu}_x\text{WO}_4$  up to  $x = 0.1$  [68]. So Ni doping as low as  $x = 0.05$  completely suppresses the AF1 phase and stabilize spiral AF2 phase below 13 K. A complete suppression of collinear AF1 phase was also reported in Zn doping of as low as 5% [55], however, a mixture of collinear AF1 and

spiral AF2 phase was observed in  $\text{Mn}_{1-x}\text{Cu}_x\text{WO}_4$  up to  $x = 0.1$  [68]. The collinear AF3 phase is also existing in  $\text{Mn}_{0.95}\text{Ni}_{0.5}\text{WO}_4$ , which is reflected by a sharp peak in heat-capacity measurement shown in Fig. 4.15. For  $x = 0.1$ , the  $P_b$  and  $T_C$  are almost same as in 5% Ni doping, however, the different nature of slope change at the onset of polarization could be related to the development of AF4 phase. For  $x > 0.1$ , the polarization quickly drops and completely vanishes above  $x = 0.2$ . This is due to sudden flop of the spin helical plane close to the  $a - b$  plane as confirmed by neutron diffraction. After flipping the helical plane close to  $a - b$  plane, it rotates with temperature so that the polarization passes through the maximum and becomes negative at low temperature.

It is observed that the angle  $\Theta$  decreases with increased Ni content in  $\text{Mn}_{1-x}\text{Ni}_x\text{WO}_4$  although the in-plane anisotropy of Ni ( $55^\circ$ ) in  $\text{NiWO}_4$  is higher than anisotropy of Mn ( $36^\circ$ ) in  $\text{MnWO}_4$  [59].  $\Theta$  decreases quickly from  $32.2^\circ$  to  $10^\circ$  at 5 K as we go from  $x = 0.10$  to  $x = 0.15$ . Since the polarization is proportional to  $\Theta$ , the sudden decrease of  $\Theta$  with increasing Ni content forces the polarization to reduce quickly. This suggests that the effect of Ni doping is opposite with the effect of Co doping. If the effects were similar, the angle of the helix with  $a$ -axis would increase which ultimately enhances the  $P_b$ . The Ni doping actually pushes the spin helix away from the helical plane of  $\text{MnWO}_4$ , towards the  $a - b$  plane. On the contrary, the Co spins pull the helical plane towards its easy-axis [6]. For Ni content above  $x = 0.1$ , the  $P_b$  is quickly dropped and passes through a maximum near 9 K that turns negative at low temperature. The sign change of  $P_b$  at low temperature can be explained from the rotation of spin helix with temperature. As shown in Table 4.2,  $\Theta$  is  $-3^\circ$  at

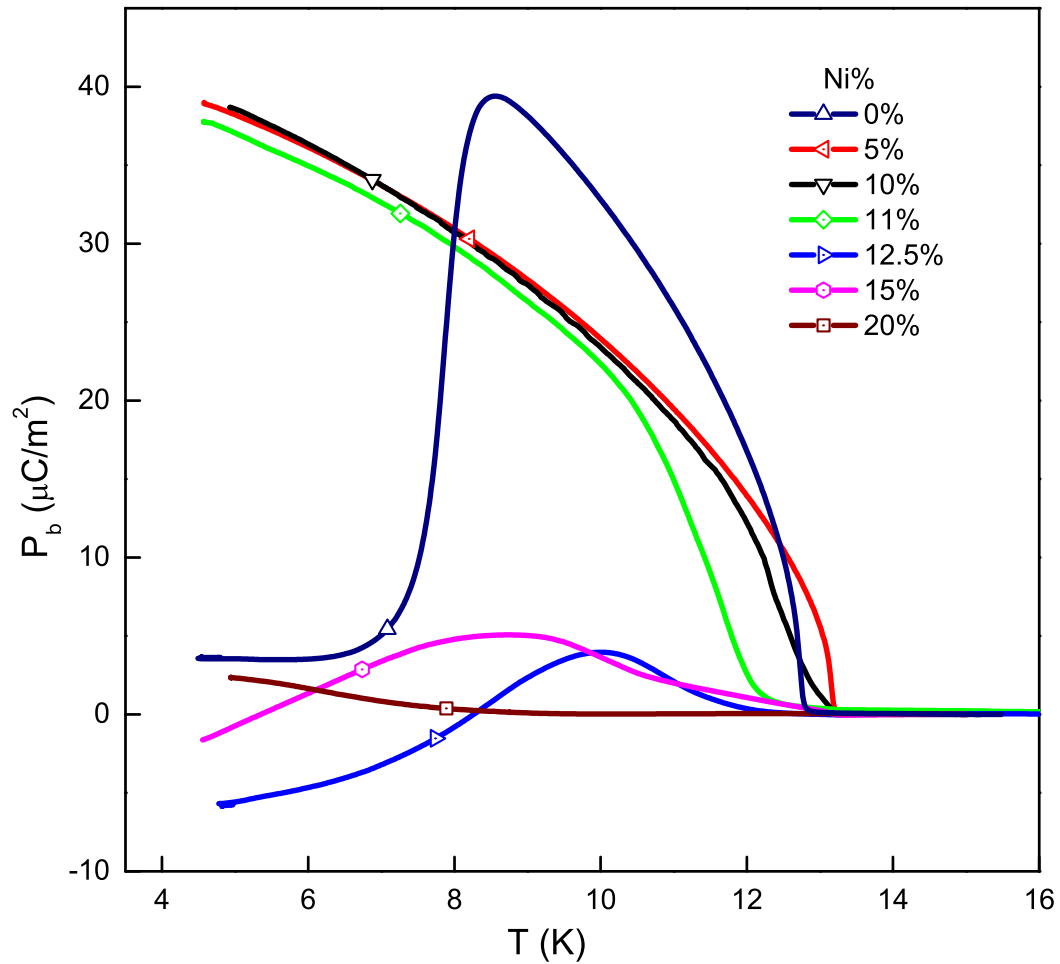


Figure 4.18: Ferroelectric polarization in  $\text{Mn}_{1-x}\text{Ni}_x\text{WO}_4$  for different  $x$  values along the  $b$ -axis. The  $P_b$  of  $\text{Mn}_{1-x}\text{Ni}_x\text{WO}_4$  is smaller than the extrapolated  $P_b$  of  $\text{MnWO}_4$ . Above 10% Ni doping, the  $P_b$  quickly drops and reverses sign at low temperature and completely vanishes above 20% Ni doping.

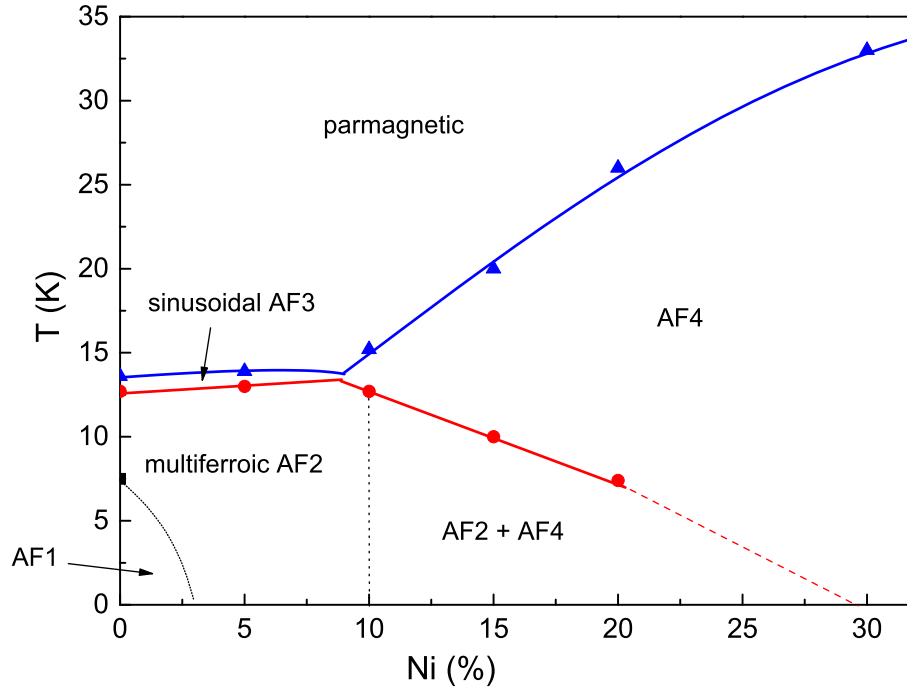


Figure 4.19: Evolution of the magnetic and multiferroic phases with Ni concentration. The phase diagram is derived from magnetic and heat capacity data which is in agreement with neutron diffraction and polarization measurement. The  $T_C$  decreases and  $T_N$  increases above 10% Ni doping. The AF2 and AF4 phases coexist between 15% to 30% Ni doping. The dotted line shows the extrapolation to low temperature.

10 K and becomes  $10^\circ$  at 5 K for  $x = 0.15$ . This change in orientation of the spin helix makes the polarization negative at low temperature. For 20% Ni doping, the polarization is rarely detected and  $T_C$  goes below 10 K, consistent with the phase diagram (Fig. 4.19) derived from magnetic and heat capacity measurement [10]. The rotation of the helical plane will, therefore, change the net value of  $P_b$ . The other possible reasons of decrease in polarization and its sign change are mentioned below.

The contribution to the polarization in  $\text{MnWO}_4$  arises from of different exchange

pathways. The different coupling parameters of long-range exchange pathways are calculated from the spin-wave model that best fits the spin wave spectrum of  $\text{MnWO}_4$  [7]. Depending on those parameters, we derived two major magnetic exchange pathways contributing to the ferroelectric polarization in  $\text{Mn}_{0.85}\text{Co}_{0.15}\text{WO}_4$ , the intrachain neighboring exchange interactions between spins along the  $c$ -axis and the interchain exchange interactions between spins aligned along the  $a$ -axis [8]. The two competitive contributions to  $P_b$  with opposite signs are explained in Eq. 4.3. If the positive term is dominant at higher temperature and the negative term is dominant at lower temperature in Eq. 4.3, then it may lead to polarization reversal upon the decreasing temperature.

The other possible reason for reduction of polarization upon doping lies on the coexistence of two magnetic phases. The neutron diffraction of  $\text{Mn}_{1-x}\text{Ni}_x\text{WO}_4$  in Fig. 4.17 shows the coexistence of two magnetic phases AF2 and AF4 above 15% Ni content. The coexistence of collinear AF4 phase and its growth towards low temperature multiferroic AF2 phase results in the suppression of the ferroelectric polarization since only the fraction of the AF2 phase will contribute to the polarization. The small angle of the spin helix  $-3^\circ$  at 10 K with the  $a$ -axis above 10% Ni doping suggests the anti-correlation effect of the easy spin axes of Ni and Mn, mediated through the exchange interactions between Ni and Mn moments. The microscopic study of these interactions has not been done yet. The spatial coexistence of the AF4 and AF2 phases requires the formation of domains of both phases separated by their respective domain walls. A strong correlation between different magnetic domains and its effect on the polarization of  $\text{Mn}_{0.85}\text{Co}_{0.15}\text{WO}_4$  is already discussed in the previous

chapter. The formation of the AF4 phase at higher temperature and its coexistence with the AF2 phase at the lower temperature could affect the orientation of the spin helix in the ferroelectric AF2 phase through a similar coupling of the magnetic orders across the domain boundaries. This effect can further be explored by the study of magnetic domains and their coupling across the domain walls.

### 4.3 Pressure effect on the ferroelectric properties of $\text{GdMn}_2\text{O}_5$ and $\text{TmMn}_2\text{O}_5$

Orthorhombic  $\text{RMn}_2\text{O}_5$  ( $\text{R} = \text{Y}$ , rare earth) are type II multiferroics which show multiple magnetic and ferroelectric phase transitions below  $T_N$  due to their frustrated nature of spins. In these family of compounds, an incommensurate magnetic order of Mn spins  $\mathbf{Q}_{ICM} = (Q_x, 0, Q_z)$  sets in at  $T_N \sim 40$  K which is paraelectric phase. This phase is followed by a commensurate order of Mn spins at slightly lower temperature where  $\mathbf{Q}_{CM} = (0.5, 0, 0.5)$  for  $\text{R} = \text{Bi}$  and  $\mathbf{Q}_{CM} = (0.5, 0, 0.25)$  for  $\text{R} = \text{Y}$ ,  $\text{Ho}$  and  $\text{Tb}$  [70, 71, 72]. This commensurate magnetic phase is ferroelectric phase. At low temperature, the spin modulation unlocks and again an incommensurate phase arises with a sharp change in polarization. The low-temperature incommensurate phase has different modulation than the high-temperature incommensurate phase. Thermal expansion measurements of these materials show strong spin-lattice coupling which gives rise to the ferroelectricity via exchange striction mechanism [13]. The Mn ions in these materials have two valence states  $\text{Mn}^{3+}$  and  $\text{Mn}^{4+}$ . The  $\text{Mn}^{4+}$  ions are surrounded by edge-sharing oxygen octahedra running along the  $c$ -axis and the

Mn<sup>3+</sup> ions are surrounded by oxygen pyramid, the two pyramids sharing one edge of the base plane. The rare-earth ions are in between octahedral chains and bipyramidal layers. In the commensurate phase, five Mn spins of nearest neighbor Mn<sup>3+</sup>-Mn<sup>3+</sup>-Mn<sup>4+</sup>-Mn<sup>3+</sup>-Mn<sup>4+</sup> repeating units in  $a-b$  plane propagate along the  $a$ -axis [36, 37]. The Mn<sup>3+</sup> and Mn<sup>4+</sup> spins pair (enclosed by the dotted ellipse) in Fig. 4.20(a) are frustrated (almost parallel spins). These unstable pairs minimize their Heisenberg exchange interactions producing lattice distortion in Mn<sup>3+</sup> site, which breaks the inversion symmetry and gives rise to the  $b$ -axis polarization. The magnetic unit cell (which consists two crystallographic unit cell) with Mn<sup>4+</sup>O<sub>6</sub> octahedra and Mn<sup>3+</sup>O<sub>5</sub> bipyramids of GdMn<sub>2</sub>O<sub>5</sub> along with moment direction (arrows) of Gd and Mn spins in the commensurate phase are shown in Fig. 4.20(a).

GdMn<sub>2</sub>O<sub>5</sub> has some different characteristics than other RMn<sub>2</sub>O<sub>5</sub> multiferroics. The incommensurate phase of modulation  $\mathbf{Q}_{ICM} = (0.49, 0, 0.18)$  sets in at  $T_N = 40$  K where it locks to commensurate phase of modulation  $\mathbf{Q}_{CM} = (0.5, 0, 0)$  at 33 K [16, 73]. This commensurate phase has the simplest form with no spin modulation along the  $c$ -axis as seen in other RMn<sub>2</sub>O<sub>5</sub>. Furthermore, the commensurate phase extends to low temperature and no additional incommensurate phase is reported down to 2 K. With  $Q_z = 0$ , the closest pair of Mn<sup>3+</sup> and Gd ions ( $d = 3.303 \text{ \AA}$ ) form the antiferromagnetic zigzag chain along the  $c$ -axis as shown in Fig. 4.26. So the main exchange interactions that couple both magnetic sub-systems in the commensurate phase are the Gd- Mn<sup>3+</sup> interactions along the  $c$ -axis where the moments are aligned approximately along the  $a$ -axis. The more exciting property of GdMn<sub>2</sub>O<sub>5</sub> is the giant  $b$ -axis polarization  $P_b \sim 3000 \mu\text{C}/\text{m}^2$  and its tunability in

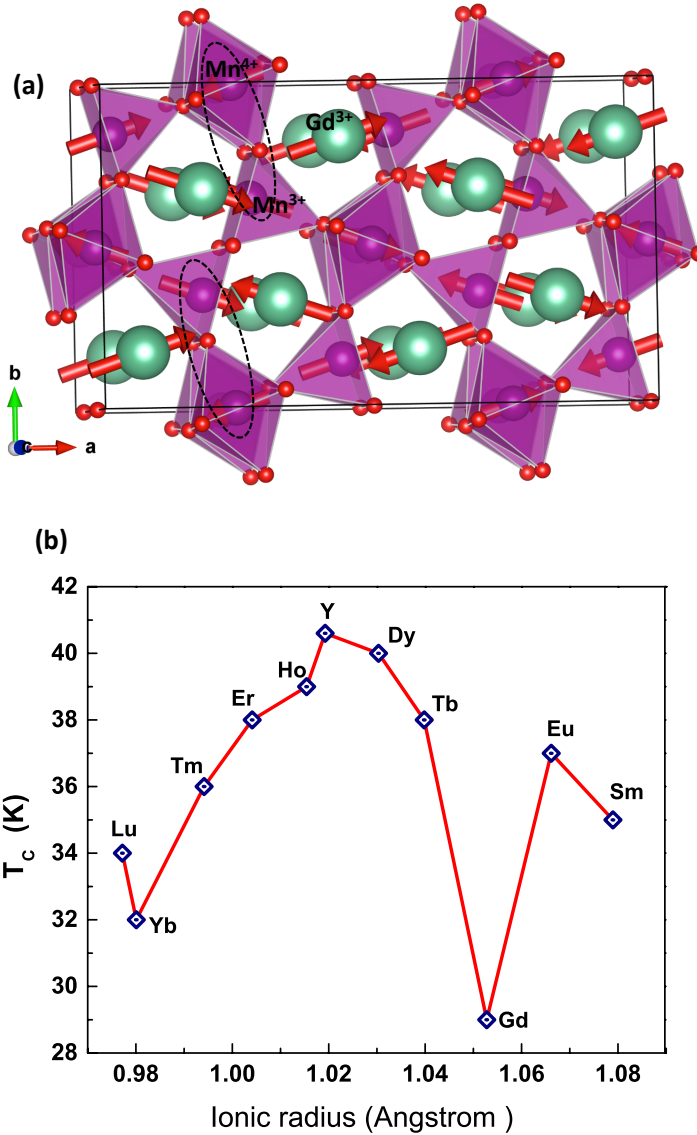


Figure 4.20: (a) Magnetic unit cell (supercell) of  $\text{GdMn}_2\text{O}_5$  in the commensurate phase. The arrows show the direction of magnetic moment of respective ions. The  $\text{Gd}^{3+}$  ions are surrounded by  $\text{Mn}^{3+}$ - $\text{Mn}^{3+}$ - $\text{Mn}^{4+}$ - $\text{Mn}^{3+}$ - $\text{Mn}^{4+}$  repeating units in the  $a-b$  plane. The labelled pair of  $\text{Mn}^{3+}$ - $\text{Mn}^{4+}$  ions are frustrated and produce lattice distortion to minimize frustration. (b) Ferroelectric  $T_C$  of  $\text{RMn}_2\text{O}_5$  vs ionic radii of rare-earth ions. The  $T_C$ 's are extracted from [11, 12, 13, 14, 15, 16].

external magnetic field [16]. The giant FE polarization in the commensurate phase is due to the additional FE lattice distortion in  $\text{GdMn}_2\text{O}_5$  provided by the symmetric exchange striction of Gd-Mn<sup>3+</sup> pair in the same direction produced by Mn<sup>3+</sup>-Mn<sup>4+</sup> exchange striction. Fig. 4.20(b) shows the onset of ferroelectricity ( $T_C = 30$  K) is the lowest compared with the  $T_C$  of other  $\text{RMn}_2\text{O}_5$  family members. The lowest ferroelectric  $T_C$  in  $\text{GdMn}_2\text{O}_5$  could be related to the ordering of Gd-moments at the relatively high temperature as the system needs more magnetic energy to order the rare earth moments at this temperature. The unique feature of Gd<sup>3+</sup> is that all f-electrons are in the high-spin state making magnetic moment isotropic which can easily be aligned with nearest neighbor Mn<sup>3+</sup> ( $m = 4 \mu_B$ ) spin.

The pressure effect in type II multiferroics has been studied by different groups. Pressure acts as a perturbation in the frustrated magnetic system and in many cases leads to unexpected results. Application of pressure in  $\text{RMn}_2\text{O}_5$ , (R = Ho, Tb, Y, Dy) enhances the polarization in low-temperature incommensurate phase by changing the incommensurate phase into commensurate phase [41, 12, 42, 43, 44, 45]. A giant increase in polarization is also reported in  $\text{RMnO}_3$  by Aoyama *et al.* [46, 47]. So in the following sections, I will discuss the pressure effect in  $\text{GdMn}_2\text{O}_5$  up to 18 kbars.

### 4.3.1 Pressure effect on dielectric constant of $\text{GdMn}_2\text{O}_5$

The measurement of real and imaginary part of dielectric constant  $\epsilon$  becomes important in ferroelectric materials. The  $\epsilon_b$  at ambient pressure and under different

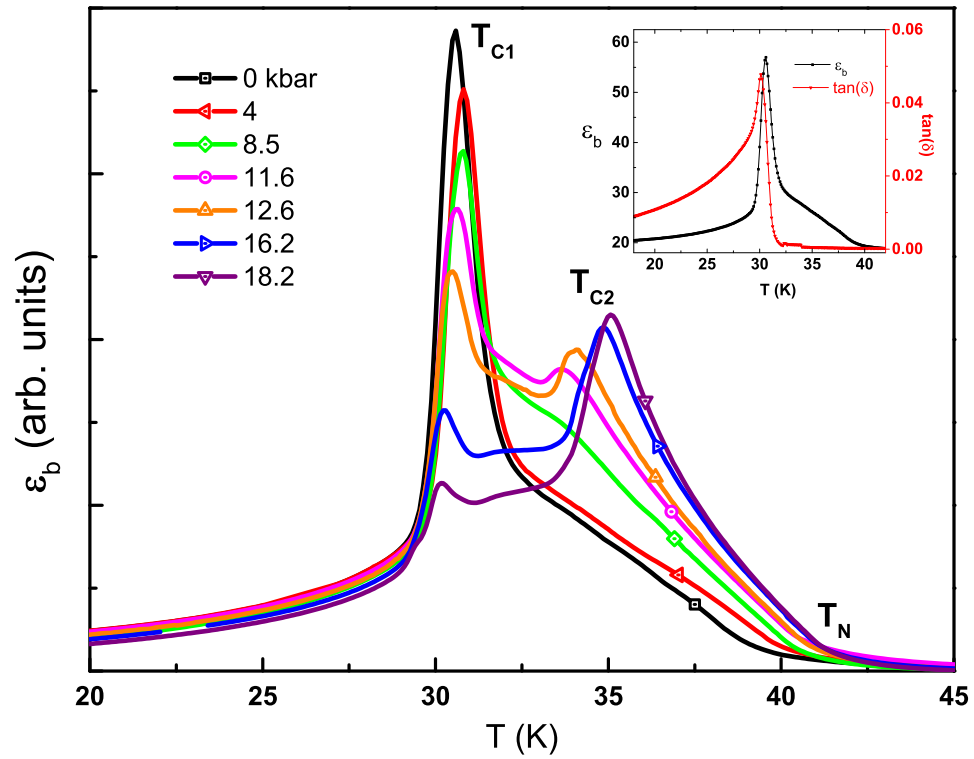


Figure 4.21: Temperature dependence of the dielectric constant of  $\text{GdMn}_2\text{O}_5$  at different pressure values. The new dielectric peak observed above  $P_C$  moves to higher temperature with pressure. The inset shows the dielectric constant and dielectric loss  $\tan(\delta)$  at ambient pressure.

pressure values is shown in Fig. 4.21. At  $T_N = 40$  K, where the Mn spins order into incommensurate phase  $\mathbf{Q}_{ICM} = (0.49, 0, 0.18)$ , the dielectric constant changes the slope and increases as shoulder towards lower temperature. The shoulder gradually increases and appears as a sharp peak at  $T_{C1} = 30$  K where the incommensurate phase locks into commensurate phase  $\mathbf{Q}_{CM} = (0.5, 0, 0)$ . This dielectric peak actually appears at the onset of first ferroelectric transition at  $T_{C1}$ . The inset of Fig. 4.21 shows that the loss factor ( $\tan\delta$ ) has sharp peak only at  $T_{C1}$  and no anomaly appears in  $\tan\delta$  at  $T_N$ . This confirms that the transition at  $T_N$  is only magnetic and transition at  $T_{C1}$  is ferroelectric. An additional small anomaly is seen in dielectric constant and loss factor at 12 K (not shown in the figure), which also reflected in magnetic measurement and indicated by slope change in polarization.

However, the dielectric constant under pressure has different behavior. The shoulder of dielectric constant just below  $T_N$  increases with pressure and a new peak (second dielectric peak) appears between  $T_N$  and  $T_{C1}$  above the critical pressure  $P_C = 11$  kbars. Upon increasing the pressure above  $P_C$ , the second dielectric peak is enhanced and moved to the higher temperature where as the ambient pressure dielectric peak moved slightly to the lower temperature. At the highest pressure of 18.16 kbars, the upper dielectric peak moved to  $T_{C2} = 35$  K and the  $T_N$  is also increased from 40 K to 42.5 K. So, a new anomaly in dielectric constant and also in loss factor (not shown in the figure) is observed under pressure.

### 4.3.2 Pressure effect on ferroelectric polarization of $\text{GdMn}_2\text{O}_5$

The ferroelectric polarization at ambient pressure shows the large value of  $P_b$  ( $\sim 3000 \mu\text{C}/\text{m}^2$ ) which is shown in Fig. 4.22(a). The ambient pressure polarization measurement is in agreement with the previously reported value [16]. The onset of ferroelectricity appears at  $T_{C1}$  reflecting the sharp transition in first ferroelectric (FE1) phase. No significant pressure effect in  $P_b$  is observed up to 8.5 kbars. At 11.6 kbars, a small  $P_b$  ( $\sim 70 \mu\text{C}/\text{m}^2$ ) in second ferroelectric (FE2) phase appears at 33 K followed by large  $P_b$  in the FE1 phase at 30 K. The onset of FE2 phase coincides with the first observed dielectric peak at this pressure. With further increase in pressure, the polarization in the FE2 phase increases to ( $\sim 600 \mu\text{C}/\text{m}^2$ ) and  $T_{C2}$  reaches to 35 K at highest pressure of 18.16 kbars which is more clear in expanded view of the FE2 phase in Fig. 4.22(b). The magnitude of the  $P_b$  in the FE1 phase is almost unaffected by the pressure. Thus we observed two-step transition in  $P_b$  under pressure.

The FE2 phase is the unique ferroelectric phase in  $\text{GdMn}_2\text{O}_5$  as this type of separate pressure induced phase at the higher temperature has not been observed previously in other  $\text{RMn}_2\text{O}_5$  family members. However, It is reported that pressure transforms the low-temperature incommensurate phase into high-temperature commensurate phase and enhances the polarization [43, 44]. The sharp transition from the FE2 phase to the FE1 phase is qualitatively different than incommensurate-commensurate phase transition, which suggests that the two phases have the different origin of ferroelectricity. The FE1 phase can not be considered as the continuation

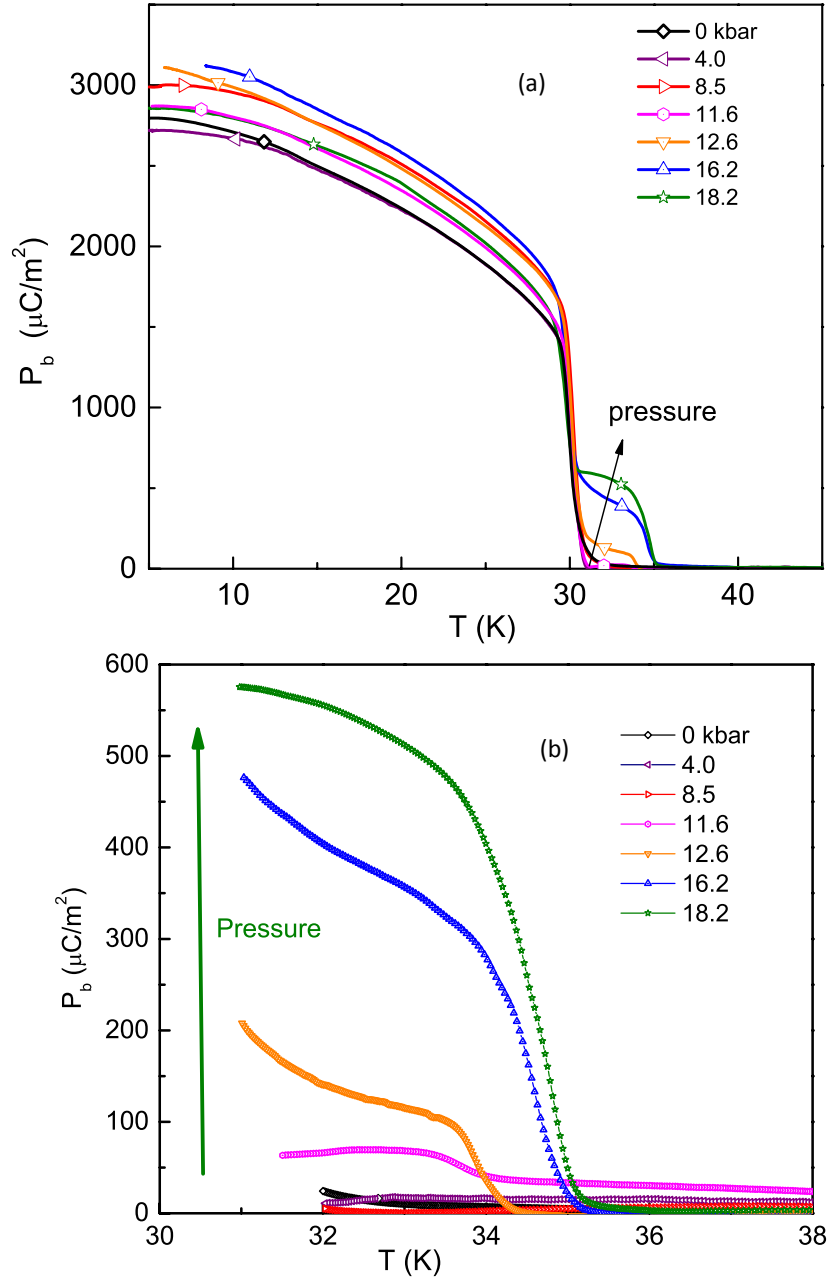


Figure 4.22: Pressure effect on FE polarization of  $\text{GdMn}_2\text{O}_5$ . (a) A new FE phase is observed above  $P_C$  in the incommensurate paraelectric region. (b) Large scale view of the new FE phase at higher temperature. The  $P_b$  and  $T_{C2}$  both increase with pressure.

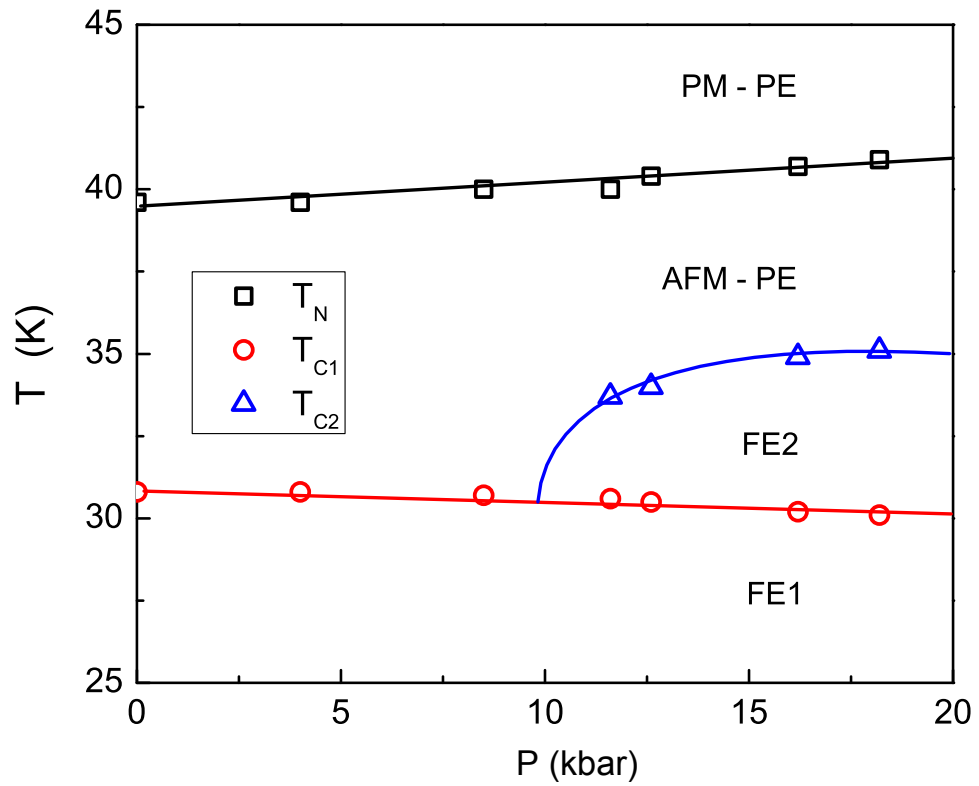


Figure 4.23: P-T phase diagram of GdMn<sub>2</sub>O<sub>5</sub> up to 18 kbars [17]. The T<sub>N</sub> and T<sub>C2</sub> increase, while T<sub>C1</sub> decreases with pressure.

of the FE2 phase which means the magnetic order in these two phases must be different. Moreover, the magnitude of polarization in the FE2 phase is comparable to other  $\text{RMn}_2\text{O}_5$  where only the Mn spins contribute to the ferroelectric polarization [43, 44, 74].

The P-T phase diagram shown in Fig. 4.23 [17] is derived from the dielectric and ferroelectric properties. It clearly shows that the stability range of incommensurate phase increases under pressure. The  $T_N$  slightly increases whereas  $T_{C1}$  slightly decreases with pressure. The FE2 phase appears above 30 K and 11 kbars in the region of incommensurate phase. The  $T_{C2}$  increases with pressure and tends to saturate at the highest pressure.

### 4.3.3 Thermal expansion and heat capacity measurement of $\text{GdMn}_2\text{O}_5$ .

The lattice anomalies at the magnetic transitions show the evidence for exchange striction mechanism in these type II multiferroics. Different exchange interactions, as well as superexchange interactions contribute to the lattice distortion in frustrated multiferroics. The lattice distortion gains the required magnetic energy by minimizing those spin frustration. The macroscopic thermal expansion measurement of  $\text{GdMn}_2\text{O}_5$  along all three crystallographic axes provides a qualitative approach of which magnetic interactions are affected at the ferroelectric transition. The lattice anomalies measured using high precision capacitance dilatometer along three crystallographic axes are shown in Fig. 4.24(a). These anomalies are more enhanced

at ferroelectric transitions than in magnetic transitions. Similar anomalies are also observed in other members of  $\text{RMn}_2\text{O}_5$  at ferroelectric and magnetic transitions [13].

The thermal expansion in  $\text{GdMn}_2\text{O}_5$  is highly anisotropic. Large expansion observed along the  $c$ -axis at  $T_C$  whereas small compression observed along the  $a$ - and  $b$ - axis. Small anomalies are also detected at other magnetic transitions. The expansion of  $c$ -axis becomes crucial to understand the most relevant exchange interactions of Gd-moments and Mn spins in  $\text{GdMn}_2\text{O}_5$ . The relative volume change near the phase transitions is shown in Fig. 4.24(b). The volume of the high-temperature incommensurate phase is smaller than the volume of the low-temperature commensurate phase and the high-temperature paraelectric phase which is seen from extrapolation to lower and higher temperature. This explains the increased stability range of the incommensurate phase and slight increase in  $T_N$  of  $\text{GdMn}_2\text{O}_5$  under pressure. This volume increase in the commensurate phase qualitatively describes the slight decrease of  $T_{C1}$  with pressure (Fig. 4.23). The volume of sample tends to decrease when pressure is increased, which favors the non-ferroelectric phase with the smaller volume by decreasing the  $T_{C1}$  and increasing the  $T_N$ .

The heat-capacity measurement of  $\text{GdMn}_2\text{O}_5$  at ambient pressure is shown in Fig. 4.23. The magnetic and ferroelectric transitions are clearly marked by two peaks at  $T_N = 40$  K and  $T_{C1} = 30$  K which are consistent with dielectric and ferroelectric measurements.

The ferroelectric phase transition appears as first-order structural phase transition which can be verified from Clausius-Clapeyron equation  $\frac{dP}{dT} = \frac{\Delta S}{\Delta V}$ . The ratio of the change in entropy  $\Delta S$  to the change in volume  $\Delta V$  i.e.  $\frac{\Delta S}{\Delta V} = -776.57$  J/cm<sup>3</sup>K

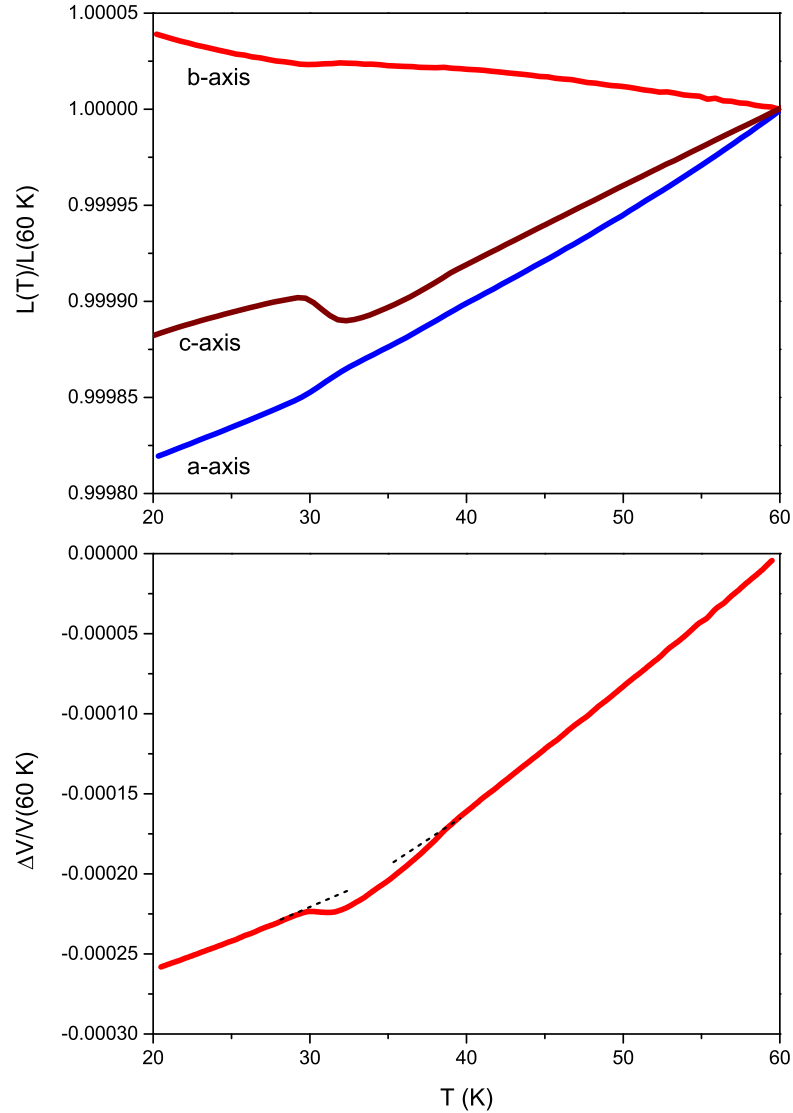


Figure 4.24: Thermal expansion measurement of  $\text{GdMn}_2\text{O}_5$  using high precision capacitance dilatometer. (a) The relative length change along the three crystallographic axes. Lattice anomalies are observed at the ferroelectric and magnetic transitions. (b) The relative volume change is calculated from the change in length of the sample. The volume of incommensurate phase is smaller than the volume of the high-temperature paramagnetic phase and the low-temperature commensurate phase. The volume increases at the FE transition in the commensurate phase.

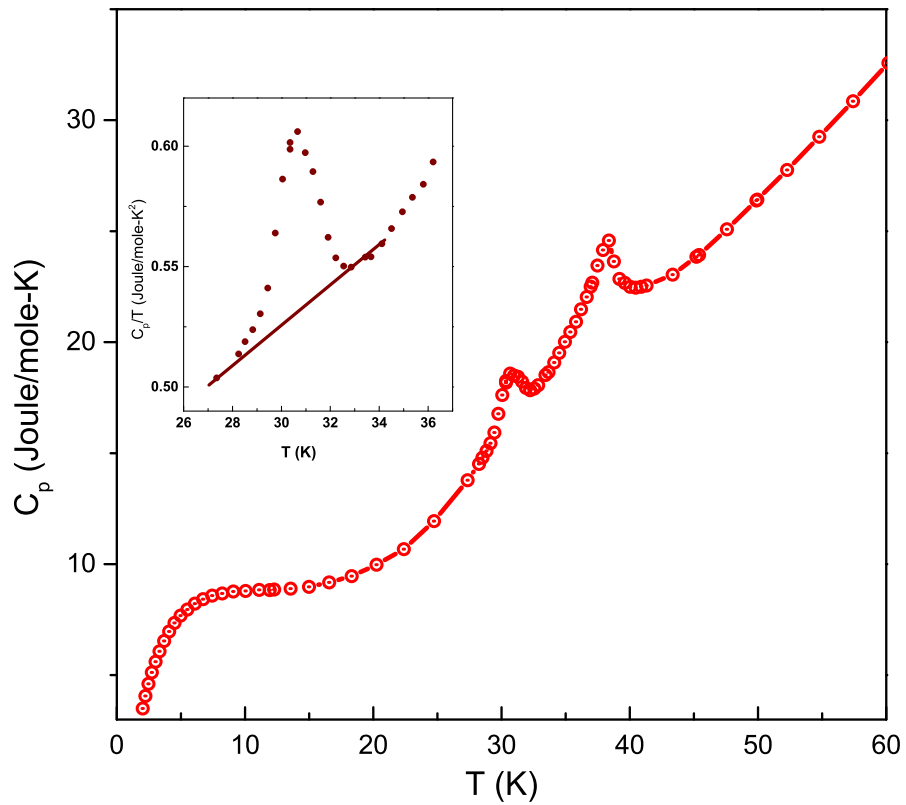


Figure 4.25: Heat capacity of  $\text{GdMn}_2\text{O}_5$  at constant pressure. The two anomalies are observed at  $T_N = 40$  K and  $T_{C1} = 30$  K. The inset shows the abrupt change in heat capacity ( $C_p/T$ ) at the ferroelectric transition.

across the ferroelectric phase transition is close to the slope  $\frac{dP}{dT} = -981 \text{ J/cm}^3\text{K}$ . The  $\Delta S$  was calculated from area under the peak of  $C_p/T$  data shown in the inset of Fig. 4.27 and the slope  $\frac{dP}{dT}$  was calculated from Fig. 4.23.

### 4.3.4 Origin of pressure-induced ferroelectric phase in $\text{GdMn}_2\text{O}_5$

The simplest commensurate phase  $\mathbf{Q}_{CM} = (0.5, 0, 0)$  and the lowest ferroelectric transition temperature  $T_C = 30 \text{ K}$  draws the attention that whether this could be related to the large polarization in  $\text{GdMn}_2\text{O}_5$ .  $Q_z = 0$  in the commensurate phase produces the AFM order between the closest pair of Gd-Mn<sup>3+</sup> along the  $c$ -axis which is the main exchange interaction that couples with the rare earth. These Gd and Mn<sup>3+</sup> ions form zigzag chains along the  $c$ -axis as shown in Fig. 4.26 with Gd-Mn<sup>3+</sup>-Gd angle,  $\theta = 118.6^\circ$ . More magnetic energy is required to maintain the AFM order of the Gd-Mn<sup>3+</sup> correlated system, which explains the lower ferroelectric  $T_C$  in  $\text{GdMn}_2\text{O}_5$ . The polar distortion produced by the Gd-Mn<sup>3+</sup> spin ordering is in the same phase of the polar distortion of Mn<sup>3+</sup>-Mn<sup>4+</sup> spin ordering [73] and gives rise to large ferroelectric polarization. Our thermal expansion measurement gives a good insight of the spin-lattice coupling at the ferroelectric transition. The large expansion of the  $c$ -axis at  $T_{C1}$  qualitatively explains that the major coupling of Gd-moments and Mn spins happen along the  $c$ -axis via Gd-Mn<sup>3+</sup> AFM exchange interaction. This Gd-Mn exchange interaction is the key parameter for the large  $P_b$  in  $\text{GdMn}_2\text{O}_5$ .

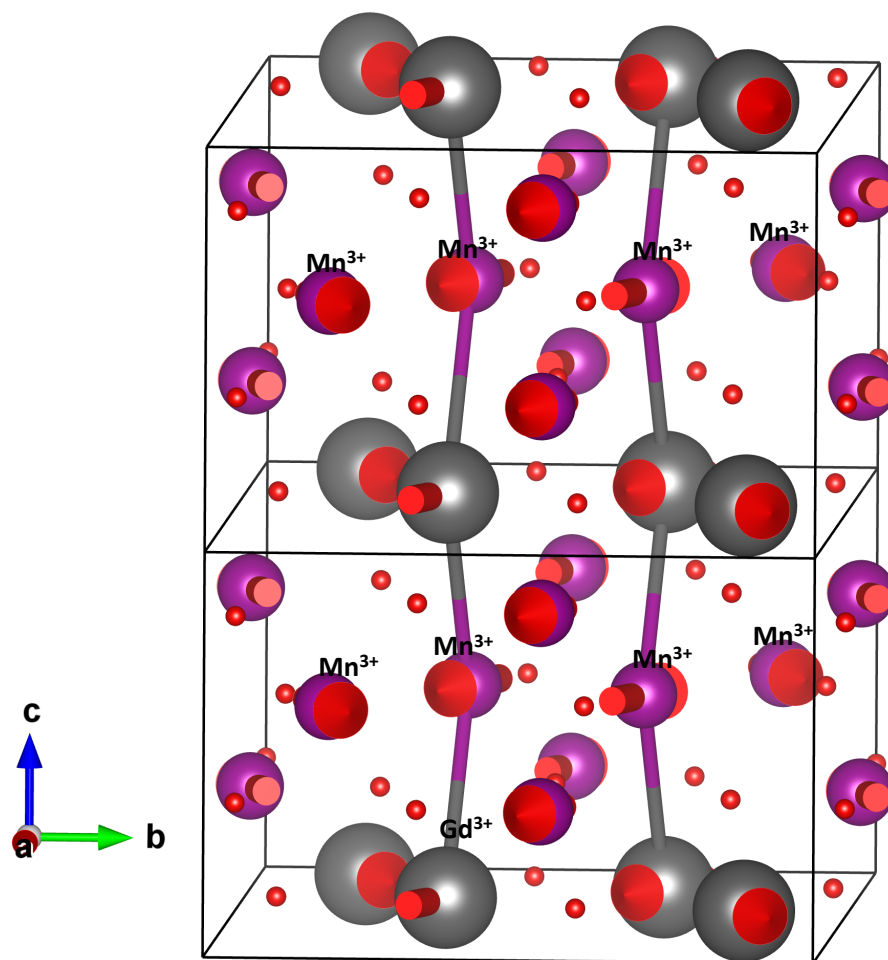


Figure 4.26: The Gd-Mn<sup>3+</sup> antiferromagnetic zigzag chains along the *c*-axis. Only Mn<sup>3+</sup> ions are labelled in the image and the smallest spheres indicate oxygen ions. The arrows show the direction of spins in the commensurate phase.

The application of pressure compresses the lattice and the significant effect of compression would be along the  $c$ -axis as indicated by Fig. 4.24(a). The compression decreases the Gd-Mn<sup>3+</sup>-Gd angle along the  $c$ -axis. As a result, the Gd-Mn interaction decreases. Above  $P_C$ , Mn-spins decouple from Gd-moments and become free from rare earth moments so that they can order antiferromagnetically in a commensurate phase possibly with  $\mathbf{Q}_{CM} = (0.5, 0, 0)$  at higher onset temperature ( $T_{C2}$ ). The proposed magnetic order needs to be confirmed from other microscopic measurements, for example, neutron diffraction. The ordering of only Mn-spins at the higher temperature gives the new ferroelectric phase in GdMn<sub>2</sub>O<sub>5</sub>. It should be noted that the Mn-spins order at the higher temperature and FE polarization arises only from Mn-spins ordering in other RMn<sub>2</sub>O<sub>5</sub> without rare earth participation in polar distortion. At lower temperature (below  $T_{C1}$ ), the Gd-Mn<sup>3+</sup> spin ordering still exists, enhances the lattice distortion in the same phase and gives the large  $P_b \sim 3000 \mu\text{C}/\text{m}^2$ . The thermal expansion measurement at ambient pressure helps to understand the decoupling of Mn-spins from Gd-moments under pressure. The large expansion of the  $c$ -axis compared to  $a$ - and  $b$ - axis indicated that the main exchange couplings between Mn and Gd ions are along the  $c$ -axis zigzag chain shown in Fig. 4.26. The stretching of the zigzag chain at  $T_{C1}$  results in the gain in magnetic energy in the commensurate phase which leads to the polar distortion. Application of pressure compresses the zigzag chains, reduces the magnetic interaction and decouples the Gd and Mn<sup>3+</sup> spin ordering above  $P_C$ . So there must be a new magnetic order of decoupled Mn-spins in the FE2 phase between (30 - 35) K which allows  $P_b$ . Future work should be focused on the more sophisticated experiments such as

neutron diffraction (ongoing study) or X-ray magnetic scattering in synchrotron facilities under high-pressure to explore the new magnetic order in the pressure induced ferroelectric phase.

### 4.3.5 Pressure effect on ferroelectricity of $\text{TmMn}_2\text{O}_5$

$\text{TmMn}_2\text{O}_5$  is one of the iso-structural members of the  $\text{RMn}_2\text{O}_5$  family which shows three ferroelectric phase transitions at ambient pressure. The first transition occurs at  $\sim 35$  K into commensurate magnetic phase and gives rise to the  $b$ -axis polarization ( $P_b$ ), the second transition at  $\sim 26$  K into incommensurate magnetic phase and also gives rise to the  $P_b$  with sharp drop in magnitude, and the third transition at  $\sim 5$  K gives rise to the  $a$ -axis polarization [74, 75]. We measured the  $P_b$  under different pressure values and the results are shown in Fig. 4.27 [76]. The polarization first appears at 35 K which corresponds to the commensurate phase. As system enters into incommensurate phase at 26 K, the polarization suddenly drops to lower value and slightly increases in further cooling. At  $\sim 5$  K, the  $b$ -axis polarization suddenly vanishes as it rotates towards the  $a$ -axis [75]. The  $a$ -axis polarization was not measured in this work. The  $P_b$  measurement up to 16.6 kbars shows no significant pressure effect in  $\text{TmMn}_2\text{O}_5$  which is shown in Fig. 4.27 [76]. However, we noticed a systematic decrease in onset temperature of the incommensurate phase and small increase in onset of the commensurate phase with increased pressure. This behavior indicates that pressure would favor the commensurate phase in  $\text{TmMn}_2\text{O}_5$ . The low-temperature incommensurate phase was completely removed and transformed into the commensurate phase with maximum polarization for  $R = \text{Y, Ho, Dy}$  and  $\text{Tb}$  up

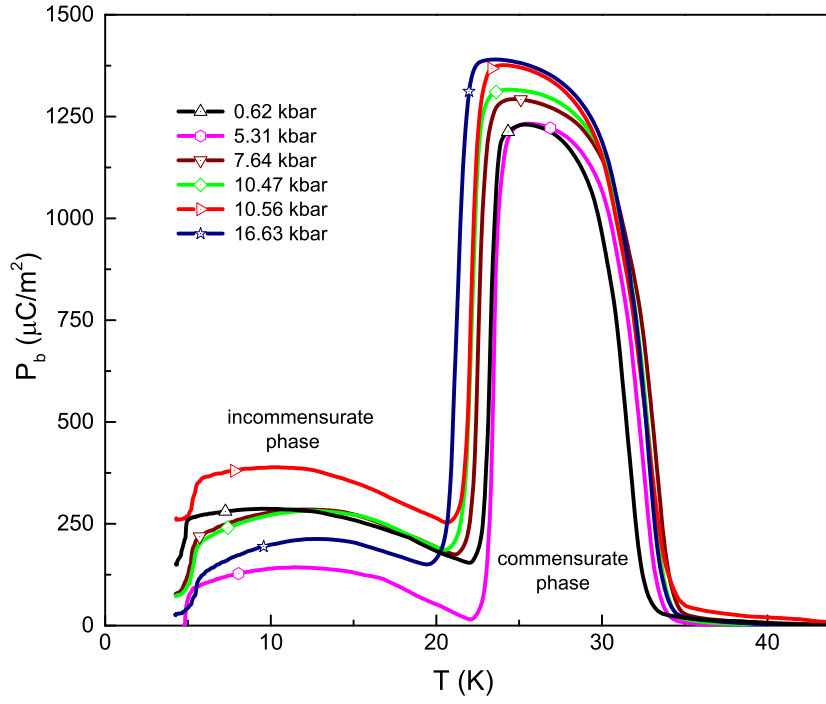


Figure 4.27: Pressure effect on the ferroelectric properties of  $\text{TmMn}_2\text{O}_5$  up to 16.6 kbars. The  $P_b$  drops to lower value in the incommensurate phase. The commensurate region slightly increases under pressure.

to this pressure limit [44, 12]. This effect is not observed in  $\text{TmMn}_2\text{O}_5$  in the same pressure range.  $\text{TmMn}_2\text{O}_5$  is found to be the most-stable member of  $\text{RMn}_2\text{O}_5$  family in the pressure range mentioned above. So, further study with higher pressures is suggested to confirm whether the pressure could convert the incommensurate phase to commensurate phase and thereby affect the polarization as well.

## 4.4 Pressure effect on Néel temperature of $\text{RCrO}_3$ ( $\text{R} = \text{Ho}, \text{Dy}, \text{Gd}$ )

Recently,  $\text{RCrO}_3$  have been reported as magnetic ferroelectrics by different groups. The interest in these class of materials arises from the relatively high  $T_N$  in these materials. The  $T_N$  in  $\text{GdCrO}_3$  was reported as high as 169 K due to the ordering of Cr spins with the additional spin ordering of rare earth at very low temperature ( $< 4$  K) [77, 78]. The ferroelectric properties of the single crystalline  $\text{RCrO}_3$  have not been reported yet. However, polarization in the polycrystalline material of different  $\text{RCrO}_3$  ( $\text{R} = \text{Ho}, \text{Sm}, \text{Gd}, \text{Er}$ ) has been reported claiming these materials as multiferroics below  $T_N$  [79, 80, 81]. Theoretical calculation shows that pressure can increase the  $T_N$  above room temperature in multiferroic  $\text{CuO}$  and increases the polarization [27]. So we were interested if we could see the pressure effect on multiferroic properties of those polycrystalline materials.

The pyroelectric current of the polycrystalline samples  $\text{HoCrO}_3$ ,  $\text{GdCrO}_3$ ,  $\text{DyCrO}_3$ , and  $\text{Ho}_{0.7}\text{Dy}_{0.3}\text{CrO}_3$  were measured using the same method mentioned in section 3 at ambient pressure. The pyroelectric current was measured with poling voltage turned off at low temperature. We end up with large leakage current in those pellet samples during both cooling and warming cycle. The background current was significant even at constant temperature (5 K). The peak in the pyroelectric current was observed in  $\text{HoCrO}_3$ ,  $\text{DyCrO}_3$ ,  $\text{Ho}_{0.7}\text{Dy}_{0.3}\text{CrO}_3$  below  $T_N$ , although the temperature was not consistent with the magnetic transition and no pyroelectric current was observed in  $\text{GdCrO}_3$  except background current. So it is difficult to decide whether the observed

current is ferroelectric current or it is coming from some trapped charges during cooling. It is also difficult to decide the base line for the integration of pyroelectric current to get the polarization.

Although the pyroelectric current and polarization are not clearly defined in these materials, it's always worth to see how the pressure affects the magnetic transition if it can be detected. So, we measured the mutual induction of the coils with the sample at ambient pressure and under pressure as mentioned in section 3 to see the magnetic transitions. In the following, I will address the pressure effect on magnetic transitions of  $\text{RCrO}_3$ .

No magnetic transition was observed in  $\text{GdCrO}_3$  from our mutual induction measurement method both at ambient pressure and under pressure but we were able to see magnetic anomalies at  $T_N$  in  $\text{DyCrO}_3$ ,  $\text{Ho}_{0.7}\text{Dy}_{0.3}\text{CrO}_3$  and  $\text{HoCrO}_3$ . The  $T_N$  values in our measurement at ambient pressure are in agreement with previously reported values somewhere in [77, 78]. Fig. 4.28 shows the effect of pressure on magnetic transition of  $\text{DyCrO}_3$ . Pressure increases the  $T_N$  from 145.7 K to 150 K up to pressure of 14 kbar. The increase of  $T_N$  with pressure is almost linear. The  $T_N$  of  $\text{HoCrO}_3$  is found to be 139.2 K as shown in Fig. 4.29 [82], which is lower by 6.5 K than the  $T_N$  of  $\text{DyCrO}_3$ . The  $T_N$  of  $\text{HoCrO}_3$  also increases with pressure and reaches to 148.2 K at pressure of 16.5 kbar. The increase in  $T_N$  of  $\text{HoCrO}_3$  with pressure is greater than the increase of  $T_N$  in  $\text{DyCrO}_3$  and also at faster rate up to 16.5 kbar.

Fig. 4.30 shows the effect of pressure on magnetic transition of Dy substituted  $\text{HoCrO}_3$ . Substitution of 30% Dy in Ho site of  $\text{HoCrO}_3$  increases the  $T_N$  by 3 K.

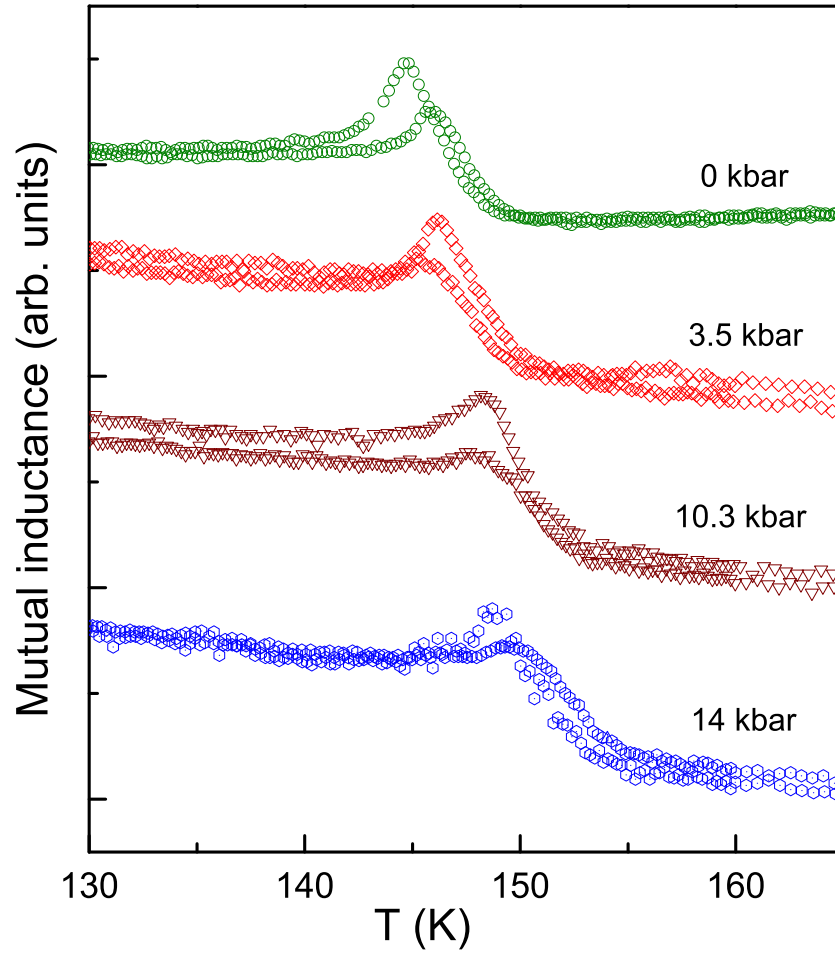


Figure 4.28: Pressure effect on the magnetic transition of  $\text{DyCrO}_3$ . The mutual inductance data are vertically offset by constant values for better visualization.

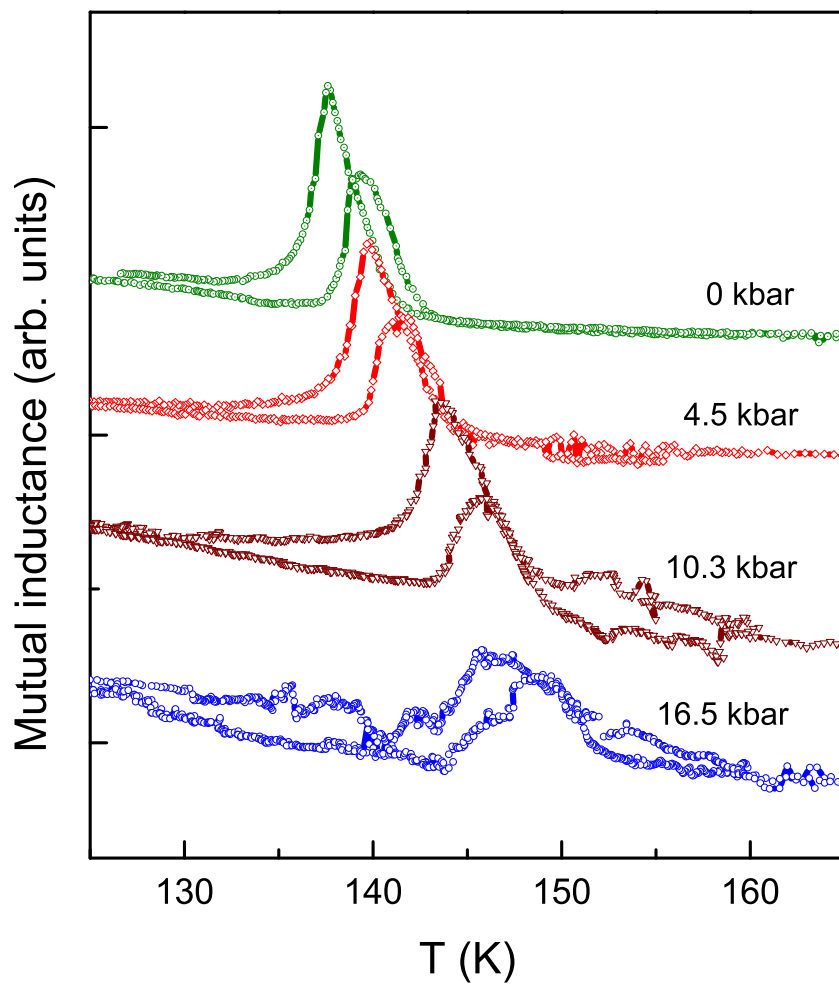


Figure 4.29: Pressure effect on the magnetic transition of HoCrO<sub>3</sub> (unpublished). The mutual inductance data are vertically offset by constant values for better visualization.

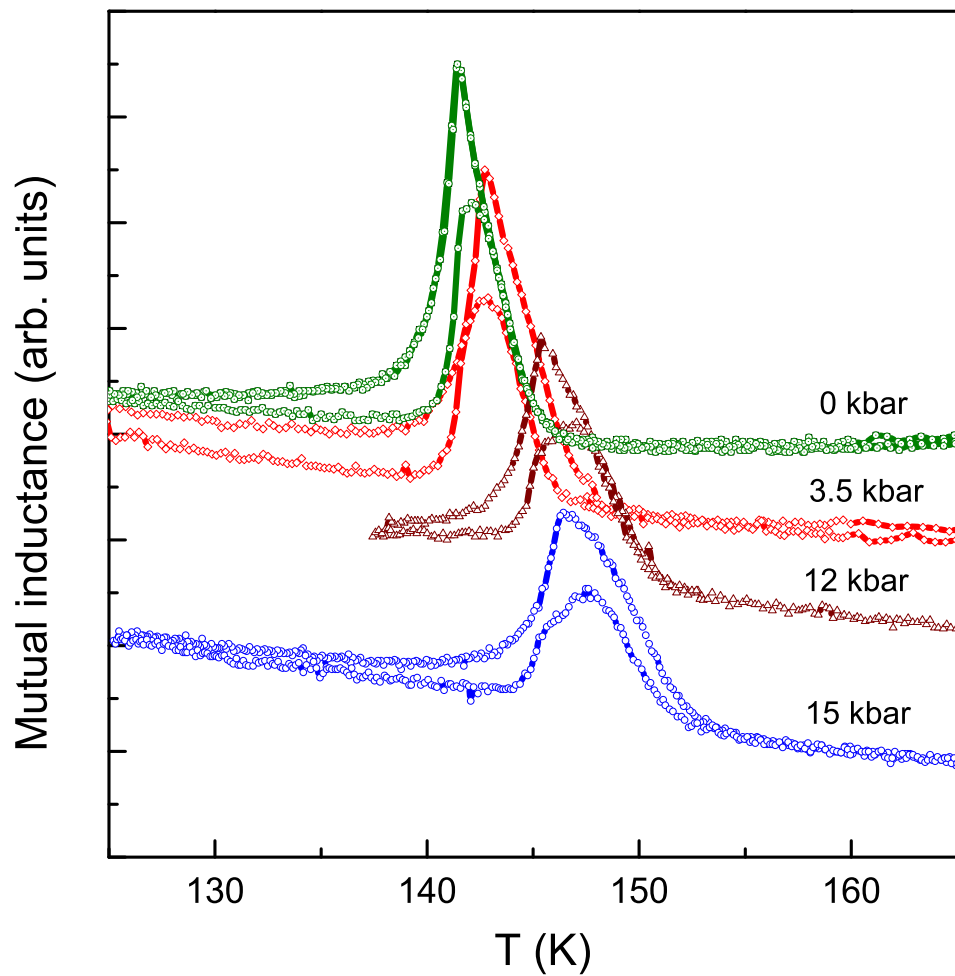


Figure 4.30: Pressure effect on the magnetic transition of  $\text{Ho}_{0.7}\text{Dy}_{0.3}\text{CrO}_3$ . The mutual inductance data are vertically offset by constant values for better visualization.

This is expected, as the  $\text{DyCrO}_3$  has higher  $T_N$  than  $\text{HoCrO}_3$ . Pressure increases the Néel transition temperature of  $\text{Ho}_{0.7}\text{Dy}_{0.3}\text{CrO}_3$  from 142 K to 147.5 K. This increase of  $T_N$  with pressure is almost linear as in  $\text{DyCrO}_3$ . The variation of  $T_N$  of these rare-earth ortho-chromates with pressure is summarized in Fig. 4.31. The microscopic mechanism of how those exchange interactions are affected by the pressure is not known yet. Our results of the increase in  $T_N$  are in agreement with the predictions of first-principles calculations [83], where the hydrostatic pressure squeezes the sample and decreases the Cr-O bond lengths linearly, favoring the antiferromagnetic transition and ultimately increasing the  $T_N$ .

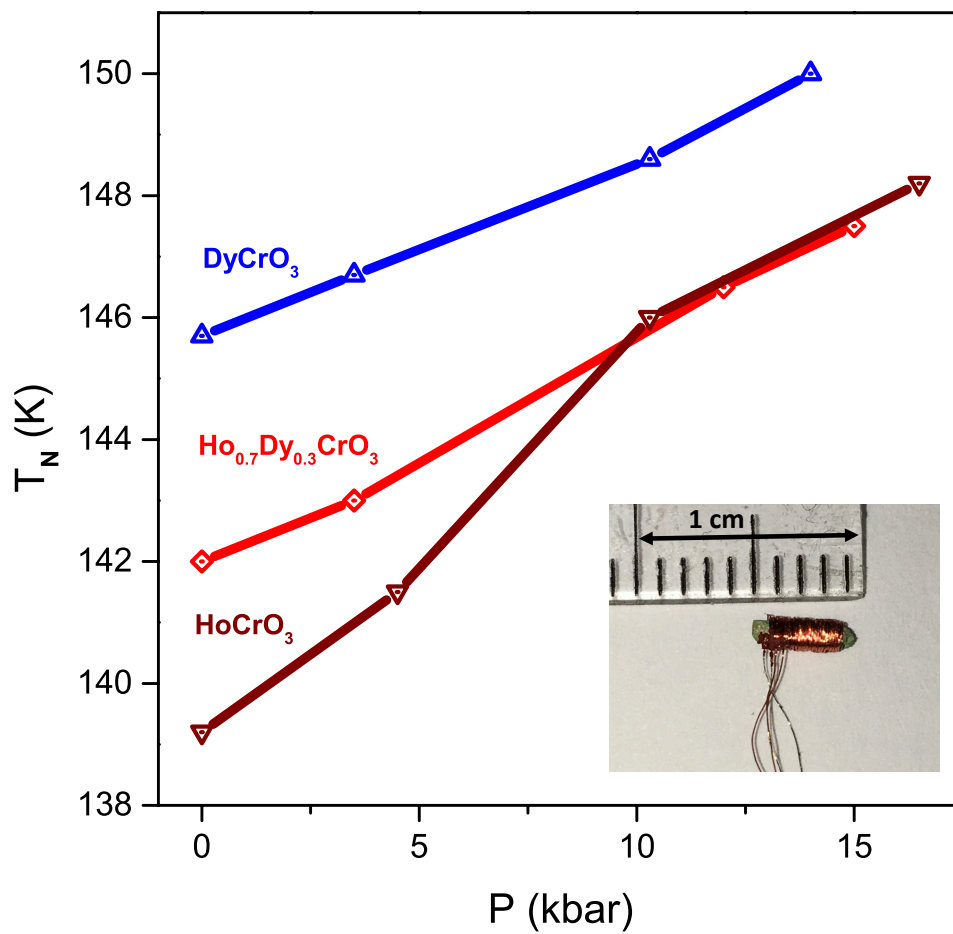


Figure 4.31: Pressure dependence of the Néel temperature of  $\text{RCrO}_3$  (unpublished). The  $T_N$  values are extracted from the peak positions of warming data. The inset image of one of the sample used for mutual induction measurement wound with two Cu coils.

# Chapter 5

## Summary

We investigated the effect of external perturbations in different types of multiferroic materials by magnetic, dielectric, thermodynamic, and neutron diffraction experiments. The magnetic field effect on the various magnetic and multiferroic phases of  $\text{Mn}_{1-x}\text{Co}_x\text{WO}_4$  is explored from the magnetic and ferroelectric measurements. The magnetic field along the plane of the spin helix in AF5 phase induces the spin-flop transition in this material. The spin-flop transition produces  $P_b$  although it is not allowed in its ground state. The polarization reversal is observed in  $\text{Mn}_{0.85}\text{Co}_{0.15}\text{WO}_4$  in a positive poling field above the critical magnetic field of 25 kOe. The reversal of the  $P_b$  in the high field AF5 phase is explained by the preserved chirality between the domains of coexisting magnetic phases during field induced phase transition. The strong coupling between the two coexisting multiferroic phases causes the  $P_b$  to be negative above a critical field. The details of the microscopic nature of spin-flop transition in this material could be studied by neutron diffraction in the magnetic

field. Moreover, the continuous rotation of polarization in  $\text{Mn}_{0.95}\text{Co}_{0.05}\text{WO}_4$  in the b-axis magnetic field was also investigated. It is found that magnetic field can tune and control the ferroelectric properties in bulk multiferroics as well as multiferroic domain walls.

The multiferroic properties of  $\text{Mn}_{1-x}\text{Ni}_x\text{WO}_4$  ( $0 < x < 0.3$ ) were studied by means of magnetic, ferroelectric, heat capacity and neutron diffraction measurements and the phase diagram of different magnetic and multiferroic phases was derived. The ferroelectricity in  $\text{Mn}_{1-x}\text{Ni}_x\text{WO}_4$  is first stabilized for small Ni content with  $T_C$  increasing by 0.5 K. The low temperature collinear AF1 phase is completely suppressed for a doping level as low as 5%. The helical AF2 phase, which is ferroelectric phase, is stabilized at low temperature through Ni doping where it develops as the magnetic ground state. Above 10% Ni content, the  $P_b$  is quickly reduced and a new high-temperature collinear AF4 phase develops. The details of different magnetic structures have been investigated by neutron-diffraction experiments. Above 20% Ni substitution, only the AF4 phase survives and becomes the ground state of the system. The sudden drop of  $P_b$  above 10% Ni doping is explained from the anti-correlation effect of Ni and Mn spins which causes the flop of the spin spiral plane close to the crystalline  $a - c$  plane. The possible mechanisms for the reorientation of the spin spiral plane and the decrease in polarization were discussed.

Pressure is one of the tuning parameters of magnetic and ferroelectric properties of materials. Pressure can change the magnetic properties of materials without polarizing the electron's spin. We studied the pressure effect in dielectric and ferroelectric properties of multiferroic  $\text{GdMn}_2\text{O}_5$  and  $\text{TmMn}_2\text{O}_5$ . The pressure-temperature

phase diagram for  $\text{GdMn}_2\text{O}_5$  was derived from dielectric and ferroelectric properties. The thermal expansion measurement at ambient pressure was also carried out to explain the giant polarization of  $\text{GdMn}_2\text{O}_5$  and pressure effect on ferroelectricity of  $\text{GdMn}_2\text{O}_5$ . The FE phase in  $\text{GdMn}_2\text{O}_5$  is split into two above  $P_C$  and the new FE phase is observed at the higher temperature. The new FE phase is explained by considering the decoupling of the Gd moments and the Mn spins of the zigzag chains along the  $c$ -axis under pressure. On the other hand, the pressure effect in  $\text{TmMn}_2\text{O}_5$  is rather different. Little observable changes were seen for pressures up to 18 kbars on the ferroelectric properties of  $\text{TmMn}_2\text{O}_5$ ; however, pressure does increase the range of commensurate ferroelectric phase by a small amount. Unlike other  $\text{RMn}_2\text{O}_5$ , the low-temperature incommensurate phase of  $\text{TmMn}_2\text{O}_5$  is found to be the most stable up to pressure limit of 18 kbars.

The last systems under pressure to be studied were the  $\text{RCrO}_3$  systems. Our work found that with increasing pressure changes the  $T_N$  of the  $\text{RCrO}_3$  materials increased. The magnetic ordering in these materials at relatively high temperature is related to ordering of the Cr-spins. The change in lattice parameters and the Cr-O bond distances by the pressure limit applied in our experiments may not be sufficient to enhance the  $T_N$  by a significant amount. Application of higher pressures may further increase the  $T_N$  to higher temperatures. Therefore future work should focus on the pressure effect on the ferroelectric (if exists) as well as the magnetic properties of these rare-earth ortho-chromates.

Although the effect of perturbation is not unusual in frustrated multiferroic materials, our results give insight and lay a possible path for more detailed investigations

of multiferroic materials under the pressure and magnetic field to explore exotic and unprecedented effects.

# Appendix A

## Publications and Conference Participations

### A.1 Publications

1. Pressure effects on magnetic ground states in cobalt-doped multiferroic  $\text{Mn}_{1-x}\text{Co}_x\text{WO}_4$ . Jinchun Wang, Feng Ye, Songxue Chi, Jaime A. Fernandez-Baca, Huibo Cao, Wei Tian, M. Gooch, N. Poudel, Yaqi Wang, Bernd Lorenz, and C. W. Chu. *Phys. Rev. B* 93, 155164 (2016).
2. Pressure effect on ferroelectric properties of  $\text{GdMn}_2\text{O}_5$  and  $\text{TmMn}_2\text{O}_5$ . Narayan Poudel, Melissa Gooch, Bernd Lorenz, Ching-Wu Chu, Jaewook Kim, and Sang-Wook Cheong. *IEEE Transactions on Magnetics* 52, 2501204 (2016).

3. Pressure-induced decoupling of rare-earth moments and Mn spins in multiferroic  $\text{GdMn}_2\text{O}_5$ . N. Poudel, M. Gooch, B. Lorenz, C. W. Chu, J. W. Kim, and S. W. Cheong. *Phys. Rev. B* 92, 144430 (2015).
4. Effects of Nickel Doping on the Multiferroic and Magnetic Phases of  $\text{MnWO}_4$ . N. Poudel, B. Lorenz, B. Lv, Y. Q. Wang, F. Ye, Jinchun Wang, J. A. Fernandez-Baca, and C. W. Chu. *Integrated Ferroelectrics* 166:1,17-29, (2015).
5. Polarization control at spin-driven ferroelectric domain walls. Naemi Leo, Anders Bergman, Andres Cano, Narayan Poudel, Bernd Lorenz, Manfred Fiebig, and Dennis Meier. *Nature Communications* 6, 6661 (2015).
6. Spontaneous polarization reversal in multiferroic  $\text{Mn}_{0.85}\text{Co}_{0.15}\text{WO}_4$  induced by an external magnetic field. Narayan Poudel, Bernd Lorenz, Kao-Chen Liang, Ya-Qi Wang, Yan Yi Sun, Feng Ye, Jaime A. Fernandez-Baca, and Ching-Wu Chu. *IEEE Transactions on Magnetics* 50, 2503904 (2014).
7. Magnetic field-induced spontaneous polarization reversal in multiferroic  $\text{Mn}_{0.85}\text{Co}_{0.15}\text{WO}_4$ . N. Poudel, K.-C. Liang, Y.-Q. Wang, Y. Y. Sun, B. Lorenz, F. Ye, J. A. Fernandez-Baca, and C. W. Chu. *Phys. Rev. B* 89, 054414 (2014).

## A.2 Conference and symposium presentations

1. **N. Poudel**, K.-C. Liang, Y.-Q. Wang, Y. Y. Sun, B. Lorenz, F. Ye, J. A. Fernandez-Baca, and C. W. Chu, "Magnetic field-induced spontaneous polarization reversal in multiferroic  $\text{Mn}_{0.85}\text{Co}_{0.15}\text{WO}_4$ ", APS March meeting 2014,

Denver, CO (oral presentation).

2. **N. Poudel**, K.-C. Liang, Y.-Q. Wang, Y. Y. Sun, B. Lorenz, F. Ye, J. A. Fernandez-Baca, and C. W. Chu, "Magnetic field-induced spontaneous polarization reversal in multiferroic  $\text{Mn}_{0.85}\text{Co}_{0.15}\text{WO}_4$ ", TcSUH Student Symposium 2014, University of Houston (oral presentation).
3. **N. Poudel**, K.-C. Liang, Y.-Q. Wang, Y. Y. Sun, B. Lorenz, F. Ye, J. A. Fernandez-Baca, and C. W. Chu, Magnetic field-induced spontaneous polarization reversal in multiferroic  $\text{Mn}_{0.85}\text{Co}_{0.15}\text{WO}_4$ , International Symposium on Emerging Multifunctional and Bio-Directed Materials 2014, San Antonio, TX (poster presentation).
4. **N. Poudel**, B. Lorenz, B. Lv, Y. Q. Wang, F. Ye, Jinchen Wang, J. A. Fernandez-Baca and C. W. Chu, "Multiferroicity in Ni doped  $\text{MnWO}_4$ ", APS March meeting 2015, San Antonio, TX (oral presentation).
5. **Narayan Poudel**, Melissa Gooch, Bernd Lorenz, Ching-Wu Chu, Jaewook Kim, and Sang-Wook Cheong, "Pressure induced decoupling of Gd-Mn spin systems in multiferroic  $\text{GdMn}_2\text{O}_5$ " MMM-Intermag 2016 joint conference, San Diego, CA (oral presentation).
6. **Narayan Poudel**, Melissa Gooch, Bernd Lorenz, Ching-Wu Chu, Jaewook Kim, and Sang-Wook Cheong, "Pressure effect on ferroelectric properties of multiferroics  $\text{RMn}_2\text{O}_5$  ( R = Gd, Tm)", APS March meeting 2016, Baltimore, MD (oral presentation).

7. **Narayan Poudel**, Melissa Gooch, Bernd Lorenz, Ching-Wu Chu, Jaewook Kim, and Sang-Wook Cheong, "Pressure induced decoupling of rare earth moments and Mn spins in multiferroic  $\text{GdMn}_2\text{O}_5$ ", TcSUH Student Symposium 2016, University of Houston (oral presentation).
8. **Narayan Poudel**, Melissa Gooch, Bernd Lorenz, Ching-Wu Chu, Jaewook Kim, and Sang-Wook Cheong, "Pressure effect on ferroelectric properties of  $\text{RMn}_2\text{O}_5$  ( R = Gd, Tm)", Gordon Research Conference on Multiferroic and Magnetoelectric Materials 2016, Lewiston, ME (poster presentation).
9. **Narayan Poudel**, Melissa Gooch, Bernd Lorenz, L. N. Bezmaternykh, V. L. Temerov and C. W. Chu "Pressure effect on ferroelectricity of multiferroic  $\text{Ho}_{0.5}\text{Nd}_{0.5}\text{Fe}_3(\text{BO}_3)_4$ ", APS March meeting 2017, New Orleans, LA (oral presentation).

# Bibliography

- [1] D. Khomskii. Classifying multiferroics: Mechanisms and effects. *Physics*, 2:20, 2009.
- [2] T. Kimura. Spiral magnets as magnetoelectrics. *Annual Review of Materials Research*, 37:387, 2007.
- [3] M. McElfresh. Fundamentals of magnetism and magnetic measurement system. *Quantum Design Inc. 1994*.
- [4] PPMS Heat capacity option user's manual. *Quantum Design Inc. 2008*.
- [5] K.-C. Liang, Y.-Q. Wang, Y. Y. Sun, B. Lorenz, F. Ye, J. A. Fernandez-Baca, H. A. Mook, and C. W. Chu. The complex multiferroic phase diagram of  $\text{Mn}_{1-x}\text{Co}_x\text{WO}_4$ . *New J. Phys.*, 14:073028, 2012.
- [6] F. Ye, S. Chi, J. A. Fernandez-Baca, H. Cao, K.-C. Liang, Y. Q. Wang, B. Lorenz, and C. W. Chu. Magnetic order and spin-flop transitions in the cobalt-doped multiferroic  $\text{Mn}_{1-x}\text{Co}_x\text{WO}_4$ . *Phys. Rev. B*, 86:094429, 2012.
- [7] F. Ye, R. S. Fishman, J. A. Fernandez-Baca, A. A. Podlesnyak, G. Ehlers, H. A. Mook, Y.-Q. Wang, B. Lorenz, and C. W. Chu. Long-range magnetic interactions in the multiferroic antiferromagnet  $\text{MnWO}_4$ . *Phys. Rev. B*, 83:140401(R), 2011.
- [8] N. Poudel, K.-C. Liang, Y.-Q. Wang, Y. Y. Sun, B. Lorenz, F. Ye, J. A. Fernandez-Baca, and C. W. Chu. Magnetic-field-induced spontaneous polarization reversal in multiferroic  $\text{Mn}_{0.85}\text{Co}_{0.15}\text{WO}_4$ . *Phys. Rev. B*, 89:054414, 2014.
- [9] Naémi Leo, Anders Bergman, Andres Cano, Narayan Poudel, Bernd Lorenz, Manfred Fiebig, and Dennis Meier. Polarization control at spin-driven ferroelectric domain walls. *Nat. Commun.*, 6:6661, 2015.

- [10] N. Poudel, B. Lorenz, B. Lv, Y. Q. Wang, F. Ye, Jincheng Wang, J. A. Fernandez-Baca, and C. W. Chu. Effects of nickel doping on the multiferroic and magnetic phases of  $\text{MnWO}_4$ . *Integrated Ferroelectrics*, 166:17–29, 2015.
- [11] I. Kagomiya, K. Kohn, and T. Uchiyama. Structure and ferroelectricity of  $\text{RMn}_2\text{O}_5$ . *Ferroelectrics*, 280:131, 2002.
- [12] R. P. Chaudhury, C. R. dela Cruz, B. Lorenz, Y. Y. Sun, C. W. Chu, S. Park, and S. W. Cheong. Pressure-induced polarization reversal in multiferroic  $\text{YMn}_2\text{O}_5$ . *Phys. Rev. B*, 77:220104(R), 2008.
- [13] C. R. dela Cruz, F. Yen, B. Lorenz, M. M. Gospodinov, C. W. Chu, W. Ratcliff, J. W. Lynn, S. Park, and S.-W. Cheong. Structural anomalies at the magnetic and ferroelectric transitions in  $\text{RMn}_2\text{O}_5$  (R=Tb, Dy, Ho). *Phys. Rev. B*, 73:100406(R), 2006.
- [14] Y. Koyata, H. Nakamura, N. Iwata, A. Inomata, and K. Kohn. Electric and magnetic low-temperature phase transitions of  $\text{YbMn}_2\text{O}_5$ . *J. Phys. Soc. Jpn.*, 65:1383, 1996.
- [15] S. Kobayashi, H. Kimura, Y. Noda, and K. Kohn. Neutron diffraction study of magnetic ordering associated with ferroelectricity in  $\text{TmMn}_2\text{O}_5$ . *J. Phys. Soc. Jpn.*, 74:468, 2005.
- [16] N. Lee, C. Vecchini, Y. J. Choi, L. C. Chapon, A. Bombardi, P. G. Radaelli, and S.-W. Cheong. Giant tunability of ferroelectric polarization in  $\text{GdMn}_2\text{O}_5$ . *Phys. Rev. Lett.*, 110:137203, 2013.
- [17] N. Poudel, M. Gooch, , B. Lorenz, C. W. Chu, J. W. Kim, and S. W. Cheong. Pressure-induced decoupling of rare-earth moments and Mn spins in multiferroic  $\text{GdMn}_2\text{O}_5$ . *Phys. Rev. B*, 92:144430, 2015.
- [18] G. Lautenschläger, H. Weitzel, T. Vogt, R. Hock, A. Bohm, M. Bonnet, and H. Fuess. Magnetic phase transition of  $\text{MnWO}_4$  studied by the use of neutron diffraction. *Phys. Rev. B*, 48:6087, 1993.
- [19] H. Weitzel and H. Langhof. Verfeinerung der momentenrichtungen in den magnetischen strukturen von  $\text{NiWO}_4$  und  $\text{CoWO}_4$ . *J. Mag. Mag. Mat.*, 4:265, 1977.
- [20] JR. W. F. Brown, R. M. Hornreich, and S. Shtrikman. Upper bound on the magnetoelectric susceptibility. *Phys. Rev.*, 168:574, 1968.
- [21] D. N. Astrov. Magnetoelectric effect in chromium oxide. *Sov. Phys. JETP*, 13:729, 1961.

- [22] G. T. Rado and V. J. Folen. Observation of the magnetically induced magnetoelectric effect and evidence for antiferromagnetic domains. *Phys. Rev. Lett.*, 7:310, 1961.
- [23] I. E. Dzyaloshinskii. On the magneto-electric effect in antiferromagnetics. *Sov. Phys. JETP*, 10:628, 1960.
- [24] Z. J. Huang, Y. Cao, Y. Y. Sun, Y. Y. Xue, and C. W. Chu. Coupling between the ferroelectric and antiferromagnetic orders in  $\text{YMnO}_3$ . *Phys. Rev. B*, 56:2623, 1997.
- [25] T. Kimura, T. Goto, H. Shintani, K. Ishizaka, T. Arima, and Y. Tokura. Magnetic control of ferroelectric polarization. *Nature (London)*, 426:55, 2003.
- [26] M. Fiebig. Revival of the magnetoelectric effect. *J. Phys. D: Appl. Phys.*, 38:R123–R152, 2005.
- [27] Xavier Rocquefelte, Karlheinz Schwarz, Peter Blaha, Sanjeev Kumar, and Jeroen van den Brink. Room-temperature spin-spiral multiferroicity in high-pressure cupric oxide. *Nat. Commun.*, 4:2511, 2013.
- [28] C. Kittel. Introduction to solid state physics. *John Wiley & Sons, Inc.*, 1996.
- [29] I. A. Sergienko and E. Dagotto. Role of the Dzyaloshinskii-Moriya interaction in multiferroic perovskites. *Phys. Rev. B*, 73:094434, 2006.
- [30] K. Taniguchi, N. Abe, T. Takenobu, Y. Iwasa, and T. Arima. Ferroelectric polarization flop in a frustrated magnet  $\text{MnWO}_4$  induced by a magnetic field. *Phys. Rev. Lett.*, 97:097203, 2006.
- [31] Y. Yamasaki, S. Miyasaki, Y. Kaneko, J.-P. He, T. Arima, and Y. Tokura. Magnetic reversal of the ferroelectric polarization in a multiferroic spinel oxide. *Phys. Rev. Lett.*, 96:207204, 2006.
- [32] S. Park, Y. J. Vhoi, C. L. Zhang, and S.-W. Cheong. Ferroelectricity in an  $s = 1/2$  chain cuprate. *Phys. Rev. Lett.*, 98:057601, 2007.
- [33] G. Lawes, A. B. Harris, T. Kimura, N. Rogado, R. J. Cava, A. Aharony, O. Entin-Wohlman, T. Yildirim, M. Kenzelmann, C. Broholm, and A. P. Ramirez. Magnetically driven ferroelectric order in  $\text{Ni}_3\text{V}_2\text{O}_8$ . *Phys. Rev. Lett.*, 95:087205, 2005.
- [34] T. Kimura, Y. Sekio, H. Nakamura, T. Siegrist, and A. P. Ramirez. Cupric oxide as an induced-multiferroic with high- $T_c$ . *Nature Materials*, 7:291, 2008.

- [35] I. A. Sergienko, C. Sen, and E. Dagotto. Ferroelectricity in the magnetic E-phase of orthorhombic perovskites. 2006.
- [36] S.-W. Cheong and M. Mostovoy. Multiferroics: a magnetic twist for ferroelectricity. *Nature Materials*, 6:13, 2007.
- [37] Y. J. Choi, H. T. Yi, S. Lee, Q. Huang, V. Kiryukhin, and S.-W. Cheong. Ferroelectricity in an ising chain magnet. *Phys. Rev. Lett.*, 100:047601, 2008.
- [38] M. Mostovoy. Ferroelectricity in spiral magnets. *Phys. Rev. Lett.*, 96:067601, 2006.
- [39] H. Katsura, N. Nagaosa, and A. V. Balatsky. Spin current and magnetoelectric effect in noncollinear magnets. *Phys. Rev. Lett.*, 95:057205, 2005.
- [40] D. Higashiyama, S. Miyasaka, N. Kida, T. Arima, and Y. Tokura. Control of the ferroelectric properties of  $\text{DyMn}_2\text{O}_5$  by magnetic fields. *Phys. Rev. B*, 70:174405, 2004.
- [41] R. P. Chaudhury, F. Yen, C. R. dela Cruz, B. Lorenz, Y. Q. Wang, Y. Y. Sun, and C. W. Chu. Pressure-temperature phase diagram of multiferroic  $\text{Ni}_3\text{V}_2\text{O}_8$ . *Phys. Rev. B*, 75:012407, 2007.
- [42] C. R. dela Cruz, F. Yen, B. Lorenz, Y. Q. Wang, Y. Y. Sun, M. M. Gospodinov, and C. W. Chu. Strong spin-lattice coupling in multiferroic  $\text{HoMnO}_3$ : Thermal expansion anomalies and pressure effect. *Phys. Rev. B*, 71:060407(R), 2005.
- [43] C. R. dela Cruz, B. Lorenz, M. M. Gospodinov, and C. W. Chu. Restoration of ferroelectricity by pressure in multiferroic  $\text{HoMn}_2\text{O}_5$ . *J. Mag. Mag. Mat.*, 310:1185, 2007.
- [44] C. R. dela Cruz, B. Lorenz, Y. Y. Sun, Y.Q. Wang, S. Park, S-W. Cheong, M. M. Gospodinov, and C. W. Chu. Pressure-induced enhancement of ferroelectricity in multiferroic  $\text{RMn}_2\text{O}_5$  (R=Tb, Dy, Ho). *Phys. Rev. B*, 76:174106, 2007.
- [45] C. R. dela Cruz, B. Lorenz, W. Ratcliff, J. Lynn, M. M. Gospodinov, and C. W. Chu. The pressure effect on the magnetic commensurability and ferroelectricity in multiferroic  $\text{HoMn}_2\text{O}_5$ . *Physica B*, 403:1359, 2008.
- [46] T. Aoyama, K. Yamaguchi, A. Lyama, S. Picozzi, K. Shimizu, and T. Kimura. Giant spin-driven ferroelectric polarization in  $\text{TbMnO}_3$  under high pressure. *Nature Communications*, 5:4927, 2014.

- [47] Takuya Aoyama, Ayato Lyama, Katsuya Shimizu, and Tsuyoshi Kimura. Multiferroicity in  $\text{RMnO}_3$  ( $R = \text{Dy}, \text{Tb}, \text{and Gd}$ ) under high pressure. *Phys. Rev. B*, 91:081107, 2015.
- [48] S. Yin and M. Jain. Enhancement in magnetocaloric properties of holmium chromite by gadolinium substitution. *J. Appl. Phys.*, 120:043906, 2016.
- [49] A. Eichler and J. Wittig. Pressure dependence of the superconducting transition temperature of lead. *Z. Angew. Physik*, 125:319–327, 1968.
- [50] A. H. Arkenbout, T. T. M. Palstra, T. Siegrist, and T. Kimura. Ferroelectricity in the cycloidal spiral magnetic phase of  $\text{MnWO}_4$ . *Phys. Rev. B*, 74:184431, 2006.
- [51] O. Heyer, N. Hollmann, I. Klassen, S. Jodlauk, L. Bohaty, P. Becker, J. A. Mydosh, T. Lorenz, and D. Khomskii. A new multiferroic material:  $\text{MnWO}_4$ . *J. Phys.: Condens. Matter*, 18:L471, 2006.
- [52] R. P. Chaudhury, F. Yen, C. R. dela Cruz, B. Lorenz, Y. Q. Wang, Y. Y. Sun, and C. W. Chu. Thermal expansion and pressure effect in  $\text{MnWO}_4$ . *Physica B*, 403:1428, 2008.
- [53] K. Taniguchi, N. Abe, H. Sagayama, S. Ohtani, T. Takenobu, Y. Iwasa, and T. Arima. Magnetic-field dependence of the ferroelectric polarization and spin-lattice coupling in multiferroic  $\text{MnWO}_4$ . *Phys. Rev. B*, 77:064408, 2008.
- [54] L. Meddar, M. Josse, P. Deniard, C. La, G. Andre, F. Damay, V. Petricek, S. Jobic, M.-H. Whangbo, M. Maglione, and C. Payen. Effect of nonmagnetic substituents Mg and Zn on the phase competition in the multiferroic antiferromagnet  $\text{MnWO}_4$ . *Chem. Mat.*, 21:5203, 2009.
- [55] R. P. Chaudhury, F. Ye, J. A. Fernandez-Baca, B. Lorenz, Y. Q. Wang, Y. Y. Sun, H. A. Mook, and C. W. Chu. Robust ferroelectric state in multiferroic  $\text{Mn}_{1-x}\text{Zn}_x\text{WO}_4$ . *Phys. Rev. B*, 83:014401, 2011.
- [56] E. García-Matres, N. Stüßer, M. Hofmann, and M. Reehuis. Magnetic phases in  $\text{Mn}_{1-x}\text{Fe}_x\text{WO}_4$  studied by neutron powder diffraction. *Eur. Phys. J. B*, 32:35, 2003.
- [57] R. P. Chaudhury, B. Lorenz, Y. Q. Wang, Y. Y. Sun, and C. W. Chu. Suppression and recovery of the ferroelectric phase in multiferroic  $\text{MnWO}_4$ . *Phys. Rev. B*, 77:104406, 2008.

- [58] R. P. Chaudhury, B. Lorenz, Y.-Q. Wang, Y. Y. Sun, and C. W. Chu. Re-entrant ferroelectricity and multiferroic phase diagram of  $\text{Mn}_{1-x}\text{Fe}_x\text{WO}_4$ . *New J. Phys.*, 11:033036, 2009.
- [59] H. Weitzel. Magnetische struktur von  $\text{CoWO}_4$ ,  $\text{NiWO}_4$  und  $\text{CuWO}_4$ . *Solid State Commun.*, 8:2071, 1970.
- [60] I. Urcelay-Olabarria, E. Ressouche, A. A. Mukhin, Y. Yu. Ivanov, A. M. Balbashov, G. P. Vorobev, Ya. F. Popov, A. M. Kadomtseva, J. L. Garcia-Munoz, and V. Skumryev. Neutron diffraction, magnetic, and magnetoelectric studies of phase transitions in multiferroic  $\text{Mn}_{0.90}\text{Co}_{0.10}\text{WO}_4$ . *Phys. Rev. B*, 85:094436, 2012.
- [61] Jinchun Wang, Feng Ye, Songxue Chi, Jaime A. Fernandez-Baca, Huibo Cao, Wei Tian, M. Gooch, N. Poudel, Yaqi Wang, Bernd Lorenz, and C. W. Chu. Pressure effects on magnetic ground states in cobalt-doped multiferroic  $\text{Mn}_{1-x}\text{Co}_x\text{WO}_4$ . *Phys. Rev. B*, 93:155164, 2016.
- [62] M. Gooch, N. Poudel, B. Lorenz, K.-C. Liang, Y. Q. Wang, Y. Y. Sun, J. Wang, F. Ye, J. A. Fernandez-Baca, and C. W. Chu (unpublished).
- [63] R. P. Chaudhury, F. Ye, J. A. Fernandez-Baca, Y.-Q. Wang, Y. Y. Sun, B. Lorenz, H. A. Mook, and C. W. Chu. Magnetic and multiferroic phases of single-crystalline  $\text{Mn}_{0.85}\text{Co}_{0.15}\text{WO}_4$ . *Phys. Rev. B*, 82:184422, 2010.
- [64] Narayan Poudel, Bernd Lorenz, Kao-Chen Liang, Ya-Qi Wang, Yan Yi Sun, Feng Ye, Jaime A. Fernandez-Baca, , and Ching-Wu Chu. Spontaneous polarization reversal in multiferroic  $\text{Mn}_{0.85}\text{Co}_{0.15}\text{WO}_4$  induced by an external magnetic field. *IEEE Transactions on Magnetics*, 50:2503904, 2014.
- [65] K.-C. Liang, R. P. Chaudhury, Y. Q. Wang, Y. Y. Sun, B. Lorenz, and C. W. Chu. Field-induced continuous rotation of the polarization in multiferroic  $\text{Mn}_{0.95}\text{Co}_{0.05}\text{WO}_4$ . *J. Appl. Phys.*, 111:07D903, 2012.
- [66] D. Meier, J. Siedel, A. Cano, K. Delaney, Y. Kumagai, M. Mostovoy, N. A. Spaldin, R. Ramesh, and M. Fiebig. Anisotropic conductance at improper ferroelectric domain walls. *Nature Materials*, 11:3249, 2012.
- [67] R. P. Chaudhury, B. Lorenz, Y. Q. Wang, Y. Y. Sun, C. W. Chu, F. Ye, J. Fernandez-Baca, H. Mook, and J. Lynn. Re-entrant spiral magnetic order and ferroelectricity in  $\text{Mn}_{1-x}\text{Fe}_x\text{WO}_4$  ( $x=0.035$ ). *J. Appl. Phys.*, 105:07, 2009.

- [68] K.-C. Liang, Y.-Q. Wang, Y. Y. Sun, B. Lorenz, and C. W. Chu. Control of improper ferroelectricity by chemical substitution and magnetic fields in multiferroic  $\text{Mn}_{1-x}\text{Cu}_x\text{WO}_4$ . *Ferroelectrics*, 470:43–51, 2014.
- [69] Y.-S. Song, J.-H. Chung, J. M. S. Park, and Y.-N. Choi. Stabilization of the elliptical spiral phase and the spin-flop transition in multiferroic  $\text{Mn}_{1-x}\text{Co}_x\text{WO}_4$ . *Phys. Rev. B*, 79:224415, 2009.
- [70] G. R. Blake, L. C. Chapon, P. G. Radaelli, S. Park, N. Hur, S.-W. Cheong, and J. Rodriguez-Carvajal. Spin structure and magnetic frustration in multiferroic  $\text{RMn}_2\text{O}_5$  (R=Tb, Ho, Dy). *Phys. Rev. B*, 71:214402, 2005.
- [71] L. C. Chapon, P. G. Radaelli, G. R. Blake, S. Park, and S.-W. Cheong. Ferroelectricity induced by acentric spin-densitywaves in  $\text{YMn}_2\text{O}_5$ . *Phys. Rev. Lett.*, 96:097601, 2006.
- [72] C. Vecchini, L. C. Chapon, P. J. Brown, T. Chatterji, S. Park, S.-W. Cheong, and P. G. Radaelli. Commensurate magnetic structures of  $\text{RMn}_2\text{O}_5$  (R=Y, Ho, Bi) determined by single-crystal neutron diffraction. *Phys. Rev. Lett.*, 77:134434, 2008.
- [73] C. Vecchini, A. Bombardi, L. C. Chapon, N. Lee, P. G. Radaelli, and S.-W. Cheong. Magnetic phase diagram and ordered ground state of  $\text{GdMn}_2\text{O}_5$  multiferroic studied by x-ray magnetic scattering. 519:012004, 2014.
- [74] M. Fukunaga, H. Kimura, Y. Noda, and K. Kohn. Temperature dependences of electric polarization and magnetic ordering of  $\text{TmMn}_2\text{O}_5$ . *J. Kor. Phys. Soc.*, 51:768–771, 2007.
- [75] M. Fukunaga, H. Kimura, Y. Noda, and K. Kohn. Discovery of polarization flop transition and simultaneous measurements of magnetic ordering and dielectric properties of  $\text{TmMn}_2\text{O}_5$ . *J. Phys. Soc. Jpn.*, 77:094711, 2008.
- [76] Narayan Poudel, Melissa Gooch, Bernd Lorenz, Ching-Wu Chu, Jaewook Kim, and Sang-Wook Cheong. Pressure effect on ferroelectric properties of  $\text{GdMn}_2\text{O}_5$  and  $\text{TmMn}_2\text{O}_5$ . *IEEE Transactions on Magnetism*, 52:2501204, 2016.
- [77] N. Kojima, K. Tsushima, K. Aoyagi, and I. Tsujikawa.  $\text{Cr}^{3+}$  exciton accompanied with  $\text{R}^{3+}$  spin flip in rare-earth orthochromite  $\text{RCrO}_3$ . *J. Mag. Mag. Mater.*, 31:560–562, 1983.
- [78] N. Kojima, K. Tsushima, K. Aoyagi, and I. Tsujikawa. Optical investigations of rare-earth orthochromites  $\text{RCrO}_3$  (R=Er, Ho, Dy, and Tb). *J. Phys. Soc. Jpn.*, 54:4804–4820, 1985.

- [79] Z. X. Cheng, X. L. Wang, S. X. Dou, H. Kimura, and K. Ozawa. A novel multiferroic system: rare earth chromates. *J. Appl. Phys.*, 107:09, 2010.
- [80] A. Ghosh, K. Dey, M. Chakraborty, S. Majumdar, and S. Giri. Polar octahedral rotations, cation displacement and ferroelectricity in multiferroic  $\text{SmCrO}_3$ . *Euro. Phys. Lett.*, 107:47012, 2014.
- [81] B. Rajeswaran, D. I. Khomskii, A.K. Zvezdin, C.N.R. Rao, and A. Sundaresan. Field-induced polar order at the Néel temperature of chromium in rare-earth orthochromites : interplay of rare-earth and Cr magnetism. *Phys. Rev. B*, 86:214409, 2012.
- [82] S. Yin, M. S. Seehra, Curtis J. Guild, Steven L. Suib, N. Poudel, B. Lorenz, and M. Jain. Magnetic and magneto-caloric properties of  $\text{HoCrO}_3$  tuned by selective rare-earth doping (unpublished).
- [83] H. J. Zhao, W. Ren, X. M. Chen, and L. Bellaiche. Effect of chemical pressure, misfit strain and hydrostatic pressure on structural and magnetic behaviors of rare-earth orthochromates. *J. Phys.: Condens. Matter*, 25:385604, 2013.